Universidad Autónoma de Madrid

Programa de Doctorado en Biociencias Moleculares

Tesis doctoral

Assembly, super-assembly and impaired assembly of the mitochondrial electron transport chain: *in situ* validation of the plasticity model

Elena Martín García

Madrid 2018

Facultad de Ciencias

Universidad Autónoma de Madrid

Assembly, super-assembly and impaired assembly of the mitochondrial electron transport chain: *in situ* validation of the plasticity model

Doctorando:

Elena Martín García

Licenciada en Bioquímica

Madrid 2018

Director de tesis:

José Antonio Enríquez Domínguez

El Doctor José Antonio Enríquez Domínguez, líder del grupo de investigación “Genética Funcional del Sistema de Fosforilación Oxidativa” del Centro Nacional de Investigaciones Cardiovasculares (CNIC),

CERTIFICA

Que la Tesis Doctoral “***Assembly, super-assembly and impaired assembly of the mitochondrial electron transport chain: in situ validation of the plasticity model***” ha sido realizada en la Fundación Centro Nacional de Investigaciones Cardiovasculares Carlos III, bajo su tutela, y que reúne las condiciones para optar al grado de Doctor.

Madrid, 2018

Fdo. José Antonio Enríquez

ACKNOWLEDGMENTS

¿Es posible aprender a desafiarnos personalmente? ¿Es cierto que podemos cumplir los retos que nos propongamos, sean cuales sean? Preguntas que encuentran su respuesta después de años haciendo la tesis. Respuestas acompañadas de infinitas personas que han permitido que esto sea posible.

Y ahora, llegado el momento de dar las gracias, temo no encontrar las palabras justas o cometer alguna omisión.

Gracias a todos y cada uno de los que formáis o habéis formado parte de nuestra familia en el CNIC.

Gracias Toño, por darme la oportunidad de formar parte de la familia OXPHOS para sacar adelante un proyecto tan duro y complejo como el que hemos hecho.

Gracias Valeria, por que sólo nosotras podemos decir que un 50! es posible, por tu paciencia y ayuda incansable.

Gracias a mi manita mala, a mi chica favorita, la princesa verde de los cuentos de hadas, de Mar y de prosa, que me obliga a ser valiente cuando las cosas se tuercen. Gracias por todo, por ser mi amarillo, mi norte y mi sur. Por nuestras charlas y consejos malos. Y por enseñarme que los puntos nunca son finales, siempre pueden continuar.

Gracias Rocío, Adela y AnaV, por ser las hermanas mayores de las que cualquiera quiere aprender, por vuestros abrazos y locuras transitorias. Porque se acaba esta aventura y siempre os tendré de compañeras de viaje.

Gracias a Yolandi y Varus, por ser moralmente repugnantes, porque la vida te puede sonreír, pero es mejor esperar que te suelte carcajadas. Gracias por enseñarme a reír cuando más lo necesitaba. A mi Rachel, porque eres buena y bonita por dentro y por fuera, y con tu humildad y naturalidad haces que todo vaya mejor.

Gracias a mis pequeños pero grandes pollitos. A Isa, por ser fuerte y poderosa, porque siempre consigues ver el lado bueno de las cosas. A Andrés, porque eres inagotable y me has enseñado que siempre se puede abrir un capitulo nuevo, gracias por todas las charlas y tu apoyo incondicional.

Gracias Carmen, por acompañarme de la mano desde los inicios, por tu rigor y tu bondad. Cristiane gracias por dejarme ver el mundo en superresolución. A Conchi, por tus palabras de ánimo, aconsejarme y ayudarme. A Sara por tus aires de calma cuando se acerca la tormenta y a Rebe por traer la energía en los días donde más cafeína necesitábamos. A, Carol, Clara, Xiaotong, Sergio y Umut, por vuestras conversaciones y haber traído aire fresco al labo.

Gracias a los estudiantes: Cristina, Blanca, Laura, María, Nerea, Belén, Alba, Carol, Diana, Marta, Esther mi Chester, Dani mi Prim, Raquel, Marta y a mi pilichi Macarena. Habéis hecho todos los ratos únicos con vuestro sentido del humor y ganas de aprender.

Gracias a la unidad de microscopia: Vero, Elvira, Moreno y Hélio, gracias por dejaros los sesos con las ideas locas de mi proyecto y la infinita ayuda que me habéis dado.

Pero todo esto no habría sido posible sin mi pequeña, pero enorme familia:

Gracias mamá, porque pocas palabras se pueden decir para devolver todo lo que has hecho y haces por mi. Eres incansable, fuerte y un ejemplo de superación. De mayor quiero ser como tú. Gracias papá, por tu sentido del humor e intentar entender lo que es la mitocondria, aunque ya sabes que hay tesis mas raras que la mía. Gracias Xoxi por tu rebeldía, por querernos como lo haces y hacernos mejores solo con verte sonreir.

Gracias Tere, mi madrina, mi ángel de la guarda, gracias por tu preocupación, por tus palabras de aliento y tus sabios consejos. Gracias a los Sergios y a los bebes porque hacéis que todo sea más llevadero. Y por supuesto gracias al resto de todos mis tíos y primos, la familia unida jamás será vencida.

Gracias a los Pepos, por ser mis padres adoptivos, quererme y tratarme como una bruji más en la familia. Gracias Evis que "le bella comme le papaya", por ser un minion peleón, hacernos piar y ser la mejor cuñada que cualquiera querría tener. También quiero agradecer al resto de los Sanabreses que hacéis que la palabra familia siga cobrando sentido: abuelita Carmen, abuelito Paco, Sandra, Pili, Ricky, JoseMi, Carmen, Loli, abuelitas tías…a todos.

No quiero olvidarme de la familia que se elige. Gracias Dradis, Spínolas de raíces y freaks de corazón. Rix, Mari, Kabe, Deva, Jony, Malmu, Fonfrun, arribota por nosotros!

A mi coatí, mi cazador de dragones. Mi luz celta en medio de esta guerra de palabras raras y que hizo de la ilusión un resplandor, por ser sol del amanecer y luna entre las estrellas…GRACIAS.

ABSTRACT

The oxidative phosphorylation system (OXPHOS) comprises three fundamental processes: electron transport, proton pumping and ATP synthesis. The OXPHOS system is organized as a branched chain of multi-protein complexes that can be assembled into supra-molecular structures (supercomplexes) to optimize the utilization of the different sources of electrons. We have proposed the plasticity model as a dynamic model where free and super-assembled RCs may coexist and be functional.

This model is supported by the disruption of the mitochondrial membranes with mild detergents and visualization of supercomplexes (SCs) by blue native electrophoresis (BNGE) extracted from cell lines or tissues.

In this thesis, we have developed an innovative and robust approach to visualize and quantitatively estimate the proximity of the mitochondrial complexes and SCs (I/III, III/IV, I/IV and I/III/IV) in intact cells, without the use of detergents.

For that purpose, we have analyzed different combinations of mitochondrial endogenous subunits by Stimulated Emission Depletion super resolution microscopy (STED) using a variety of cellular tools: mtDNA depleted cells (ρ^o), complex III ($CYTb^M$) and complex IV ($Cox10^{KO}$) depleted cell lines, and their respective isogenic controls. Moreover, we have used different immunolabelling combinations to tag RCs and SCs (CI/CIII, CI/CIV, CIII/CIV and CI/CIII/CIV).

Thus, STED imaging reveals the co-existence of free and superassembled complexes in intact cells demonstrating in situ that the cellular organization of the mitochondrial respiratory chain are correctly represented by the plasticity model.

On the other hand, It is known that mutations in genes encoding subunits of the mitochondrial complexes may affect the stability of other complexes. Therefore, as a second main aim, we investigate the molecular mechanism that allows CIII mutants, to suppress the effect of mutations, which impede the assembly of respiratory complexes in normal circumstances.

RESUMEN

El sistema de fosforilación oxidativa concentra tres funciones principales: el transporte de electrones, el bombeo de protones y la síntesis de ATP. Este sistema está organizado como una cadena de complejos multiproteicos que pueden ensamblarse en estructuras supramoleculares con el fin optimizar el transporte electrónico. En particular nuestro grupo se centra en el estudio de estos complejos mitocondriales dentro del modelo de la plasticidad, modelo dinámico en el cual encontramos los complejos aislados o superensamblados como supercomplejos de manera funcional.

Este modelo está respaldado por la disrupción de las membranas mitocondriales con detergentes suaves y la visualización de supercomplejos (SC) mediante electroforesis nativa azul (BNGE) extraída de líneas celulares o tejidos.

En esta tesis hemos desarrollado una metodología innovadora y robusta para visualizar y estimar cuantitativamente la proximidad de los complejos mitocondriales y SC (I / III, III / IV, I / IV e I / III / IV) en células intactas, sin el uso de detergentes

Para ello, hemos analizado diferentes combinaciones de subunidades endógenas mitocondriales mediante microscopía de depleción de emisión estimulada (STED) utilizando una variedad de herramientas celulares: células que carece de mtDNA (ρ^o), mutantes del complejo III ($CYTb^M$) y líneas celulares deficientes de complejo IV ($Cox10^{KO}$) y sus respectivos controles isogénicos. Por otro lado, hemos utilizado diferentes combinaciones para imunodetectión para componer los RC y SC (CI / CIII, CI / CIV, CIII / CIV y CI / CIII / CIV).

Por lo tanto, la técnica STED revela la coexistencia de complejos libres y superensamblados en células intactas con el fin de confirmar el modelo de plasticidad de la organización de la cadena respiratoria mitocondrial.

Por otro lado, se sabe que las mutaciones en genes que codifican subunidades de los complejos mitocondriales pueden afectar la estabilidad de otros complejos. De esta manera, como segundo objetivo principal, investigamos el mecanismo molecular que permite a células mutantes del CIII, suprimir el efecto de mutaciones que impiden el ensamblaje de complejos respiratorios en circunstancias normales.

ABBREVIATIONS

ABBREVIATURES

λ	light wavelength
α	half-angle from which light is gathered by the objective
Å	Angstroms
4OH	4-hydroxytamoxifen
A/BA	Acrylamide/bis-acrylamide
ADP	Adenosine diphosphate
ATP	Adenosine triphosphate
ATPase	ATP sintetase
APS	Ammonium persulfate
a.u.	Arbitrary units
BSA	Bovine serum albumin
BNGE	Blue Native polyacrylamide gel electrophoresis
CI	Complex I
CII	Complex II
CIII	Complex III
CIV	Complex IV
CoA	Coenzyme A
CYT b	Cytochrome b
CYT c	Cytochrome c
DAB	3-3 'diaminobenzidine
DNA	Deoxyribonucleic acid
EM	Electron Microscopy
ER	Endoplasmic Reticulum
ERAD	ER-associated degradation

$FADH_2$	Flavin Adenine Dinucleotide
FBS	Fetal bovine serum
Fc	Fold chain
FCCP	Carbonilcianuro-p-trifluorometoxifenilhidrazona
Fw	Forward
IBM	Inner Boundary Membrane
IMM	Inner mitochondrial membrane
IMS	Intermembrane space
kDa	Kilo Dalton
NADH	Reduced nicotinamide adenine nucleotide
nDNA	Nuclear DNA
NBT	Nitroblue tetrazolium
NGS	Next Generation Sequencing
mt	Mitochondrial
mETC	Mitochondrial Electron Transport Chain
mtDNA	Mitochondrial DNA
OSCP	Oligomycin sensitivity-con- ferring protein
OXPHOS	Oxidative Phosphorylation System
PCR	Polimerase Chain Reaction
PVDF	Poly (vinylidene fluoride)
qPCR	Quantitative Polimerase Chain Reaction
RCs	Respiratory complexes
RFLP	Restriction Fragment Length Polymorphism
RNA	Ribonucleic acid
RNAseq	RNA sequencing
ROS	Reactive Oxygen Species

RPM	Revolutions per minute
Rv	Reverse
RT	Room Temperature
SCs	Supercomplexes
SD	Standard deviation
SDS-PAGE	Sodium dodecyl sulfate polyacrylamide gel electrophoresis
STED	Stimulated Emission Depletion Microscopy
TEMED	Tetrametiletilendiamina
Tris	Tris(hydroxymethyl)aminomethane
UPR	Unfolded Protein Response

INDEX

INTRODUCTION

I. MITOCHONDRIA

I.1 Structure and function

Mitochondria are subcellular organelles present in all eukaryotic cells, with some exceptions in protist, which have lost their mitochondria due to environmental adaptations, or in very specialized cells (Embley and Martin, 2006). These organelles have tubular or ovoid shape although their length and number are variable depending on the cellular type. However, their structure is defined by two membranes. The outer membrane, which separates the mitochondria from the cytoplasm, being freely traversed by ions and small molecules due to its porous nature (Kühlbrandt, 2015). The inner membrane that defines the intermembrane space and can be divided into the inner boundary membrane (IBM) and the cristae (Cogliati, Enriquez and Scorrano, 2016) (Mannella, 2006).

Mitochondria are mobile and plastic organelles that constantly change shape by fission and fusion events. Mitochondrial fission is essential for their biogenesis, since is the main tool used by the cell to remove of aged or damaged mitochondria; while fusion is the basic process maintaining an homogenous organelle population and allowing inter-complementation of mtDNA (Osellame, Blacker and Duchen, 2012). Fusion does not prevent the co-existence of functional heterogeneous organelles in the same cytoplasm (Twig *et al.*, 2008; Benador *et al.*, 2018).

The most unique feature about mitochondria is that has its own genome: the mitochondrial DNA (mtDNA). In mammal cells mtDNA is organized as a circular, double-stranded DNA molecule (Chinnery and Hudson, 2013). This genetic system, despite of containing a very small number of genes, is indispensable for the cellular life because it codifies integral proteins for the mitochondrial respiratory complexes and essential components for the synthesis of these proteins. However, mitochondria are not genetically self-sufficient, since both organelle formation and the expression of their genome depend on a large number of proteins encoded in the nucleus, which are synthesized in cytoplasmic ribosomes and imported into mitochondria. Therefore, mitochondria biogenesis is controlled by two cellular genetic systems, nuclear and mitochondrial, that must act in coordination (Kelly and Scarpulla, 2004).

Its importance stems from the fact that it is the main energy source in most eukaryotes cells that do not depend on photosynthesis (Kühlbrandt, 2015). Mitochondria participate in the control of the redox status of the cell, and are of critical importance in metabolic and signaling pathways ranging from the synthesis of pyrimidine to the regulation of apoptosis (Acín-Pérez *et al.*, 2008). Nevertheless, the most recognized function of these organelles is to produce energy as ATP by the process called oxidative phosphorylation (OXPHOS).

I.2 Oxidative Phosphorylation System (OXPHOS)

I.2.1 Structural organization and function

The OXPHOS system is one of the better and more deeply characterized metabolic pathways. It is composed of five multiprotein complexes, called complex I (NADH-ubiquinone oxidoreductase), complex II (succinate: ubiquinone oxidoreductase), complex III (ubiquinol-cytochrome c oxidoreductase), and complex IV (cytochrome c oxidase); the electron carriers ubiquinone (UQ or CoQ) and cytochrome c (cyt c); and the H^+-ATP synthase (complex V).

The mitochondrial electron transport chain (mETC) is organized as a branched chain of these multiprotein complexes that oxidize the reduced nicotinamide adenine dinucleotide (NADH) (complexes I, III, and IV) or the reduced flavin adenine dinucleotide ($FADH_2$) (complex II),

transferring electrons through CIII and CIV to oxygen, and pumping protons across the inner membrane. The electrochemical gradient thus generated drives the synthesis of ATP by complex V and the import of proteins, metabolites and ions (i. e. Ca^{2+}) into the mitochondria (Wallace, Fan and Procaccio, 2010; Enríquez, 2016a).

Different models have been proposed for the structural organization of the mETC, namely solid state model (B Chance *et al.*, 1955), the random collision (Hackenbrock, Chazotte and Gupte, 1986) and the plasticity (Acín-Pérez *et al.*, 2008) models.

The plasticity model, proposes that complexes I, III and IV can act free or super-assembled in supramolecular structures (supercomplexes) as I, IV, III_2, IV_2, I + III_2, III_2 + IV_1 or I + III_2 + IV_1 (Respirasome) (Acin-Perez et al al. 2008; Enriquez 2016). Other associations containing multiple copies of complex IV, the interaction of CII with other complexes, the interaction of CI with CIV or with V has been also suggested, but their true existence is still under debate.

I.2.2 Structures of mETC

Complex I

Complex I (CI), also called NADH: ubiquinone (CoQ) oxidoreductase, is the entry point of NADH in the respiratory chain, and catalyzes the oxidation of NADH by transferring two electrons to ubiquinone, coupling proton translocation to the intermembrane space. It is the largest enzyme of the OXPHOS system, highly conserved from humans to bacterias (Baradaran *et al.*, 2013). In mammals it consists of 44 different subunits, 37 of them are codified by the mtDNA and the other 7 by the nDNA (ND1, ND2, ND3, ND4, ND4L, ND5 AND ND6).

CI has a L-shaped structure, formed by the peripheral arm N-module, which comprises the binding and oxidation of NADH and the membrane domain that comprises the proton-translocating P-module. This two modules are connected by the Q-module that couple the electrons to the CoQ (Fiedorczuk *et al.*, 2016)(L. A. Sazanov, 2015). Seven subunits are located in the N module and another seven in the P module, all of them involved in electron transport and proton pumping mechanisms. Mammalian complex I also contains 30 accessory subunits, that participate in stabilization and assembly processes (Fiedorczuk *et al.*, 2016) (Figure 1).

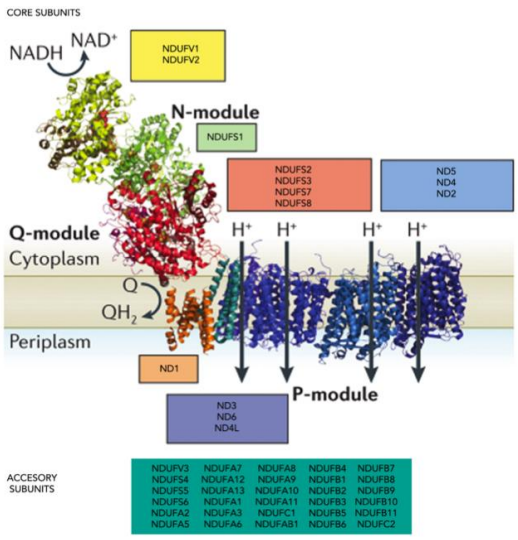

Figure 1. Subunit composition of mammalian Complex I adapted from (L. a. Sazanov, 2015). CI is an L-shaped enzyme complex that can be dissected into: N, P and Q modules. Subunits have been grouped by the subcomplex they have been identified in as core subunits and accessory subunits

Complex II

Complex II (CII), also called succinate: ubiquinone oxidoreductase, is the only respiratory complex that does not pump protons across the IM during its catalytic cycle. It catalyzes the oxidation of succinate to fumarate (Rutter, Winge and Schiffman, 2011). CII is an integral membrane protein complex, composed of four subunits that are encoded by nuclear genes SDHA, SDHB, SDHC, and SDHD. (Baysal, Rubinstein and Taschner, 2001) SDHA and SDHB encode two hydrophilic proteins, the flavoprotein (Fp) and the ironsulfur protein (Ip), respectively, while the two last ones encode two transmembrane proteins (CybL and CybS). Moreover these enzymes have different prosthetic groups required for electron transfer from succinate to ubiquinone (Sun *et al.*, 2005) (Figure 2).

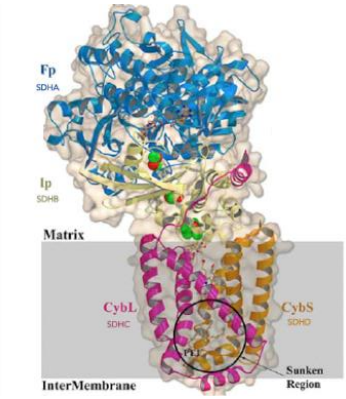

Figure 2. Structure of the mitochondrial respiratory Complex II (adapted from (Sun *et al.*, 2005)). The flavoprotein (Fp) is shown in blue; iron-sulfur protein (Ip) is shown in cream; the transmembrane proteins CybL and CybS are shown in pink and gold, respectively.

Complex III

Complex III (CIII), also called ubiquinol-cytochrome c oxidoreductase or mitochondrial cytochrome bc1 complex, is the middle component of the mETC, which couples the transfer of electrons from ubihydroquinone to cytochrome c and the proton translocation across the intermembrane space (Iwata, 1998). This complex has an homodimeric organization, each monomer is composed by 11 different polypeptide subunits within three core subunits that are required for its catalytic activity: cytochrome b with its two heme groups (bH and bL), cytochrome c1 with its heme (PDBID 1BGY), and the Rieske iron-sulfur protein with its two 2Fe-2S centers (Yang *et al.*, 2012) (Figure 3).

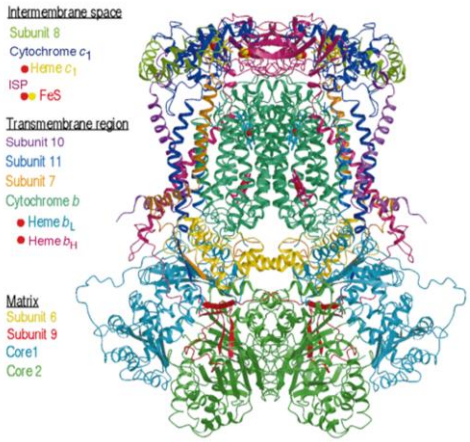

Figure 3. Structure of the dimeric mitochondrial respiratory Complex III of bovine heart from (Iwata, 1998). The 8 polypeptide subunits and the three core subunits within the bc1 complex dimer are represented.

Complex IV

Complex IV (CIV), also called cytochrome c oxidase, is the terminal component of mETC. This enzyme catalyzes the reduction of molecular oxygen to water with the electrons from cytochrome c, coupled to pumping protons to the intermembrane space (Aoyama *et al.*, 1995). The mammalian enzyme is composed of 3 core subunits encoded by the mitochondrial DNA (COX1, COX2 and COX3 subunits) and 11 subunits required for the assembly and function that are encoded by the nuclear genome (COX4, COX5A, COX5b, COX6a1, COX6b1, COX6c, COX7a2, COX7b, COX7c, COX8 and NDUFA4 subunits) (Timón-Gómez *et al.*, 2017) (Figure 4)

This enzyme requires several prosthetic groups for catalytic function: 2 hemes (a and a3), two copper centers (CuA and CuB), zinc and magnesium. (Diaz, 2010).

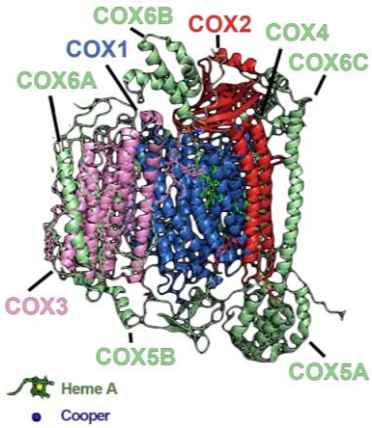

Figure 4. Mitochondrial cytochrome c oxidase structure adapted from (Timón-Gómez *et al.*, 2017). 9 subunits are shown as well as the prostetic groups for its catalytic function. Cox7a2, COX7b, COX7c, COX 8 and NDUFA4 are not represented.

Complex V

Complex V (CV), also called H^+-ATP synthase, is a multisubunit enzyme complex, that uses the proton energy gradient between the intermembrane space and the matrix, generated by the respiratory chain for the synthesis of ATP from ADP and inorganic phosphate.

The complex consists of two functional domains (F_1 and F_O) that are connected by a stalk. The structure of the catalytic part F_1 has been solved (Abrahams *et al.*, 1994) and consists of five subunits, which are assembled with a stoichiometry of 3α: 3β: 1δ: 1γ: 1ε (Walker and Collinson, 1994). The stalk and the F_O domain have the subunits: a, b, c, d, e, f, g, oligomycin sensitivity-con- ferring protein (OSCP), F6 and A6L (Belogrudov, Tomich and Hatefi, 1995). Recently two new subunits in the F_O domain have been described as DAPIT and 6,8KDa (Chen *et al.*, 2007; Meyer *et al.*, 2007).

The F_O part functions as a proton pore and directs the released power in the dissipation of the electrochemical gradient to the part F_1 in where the ATP is formed. Energy is transferred from one part to another by a rotary motor mechanism (Stock, 1999). In the last years ATPase has been also described not only as the ATP producer, but as a multiprotein complex involved in the regulation of the permeability transition pore, though the mechanism is still unclear (Giorgio *et al.*, 2013) (Figure 5).

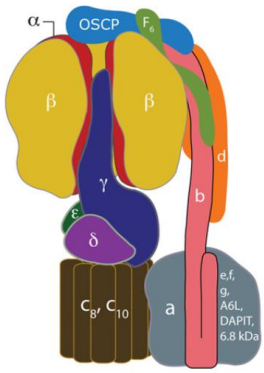

Figure 5. Structure of the ATPase synthase from (Walker, 2013). The model contains the subunits in the F1 catalytic domain, the stalk and FO domain.

I.2.3 Supercomplexes

The first model explaining the structural organization of the OXPHOS system was the "solid state" model (Britton Chance *et al.*, 1955), which postulated that the respiratory complexes were associated in high molecular weight rigid structures located in the internal mitochondrial membrane.

This model was challenged by the "fluid state model" that postulated that each complex diffuses freely through the inner mitochondrial membrane. This fluid state model was further developed by suggesting that electron transport occurs through random collisions between complexes and the cytochrome c or coenzyme Q electronic transporters, resulting in the "random collision model" (Hackenbrock, Chazotte and Gupte, 1986). In 2000, the fluid state model was challenged through the development of electrophoretic techniques in native conditions (Blue Native), which resolve the assembly of the complexes in supramolecular structures called supercomplexes (Schägger and Pfeiffer, 2000). Supercomplexes were later confirmed in mammals, plants and fungus (Schägger and Pfeiffer, 2000; Eubel, Jansch and Braun, 2003; Eubel, Heinemeyer and Braun, 2004).

Nowadays the notion that both mechanisms can coexist, giving rise to the "plasticity model" is accepted. The plasticity model postulates that respiratory complexes are in dynamic equilibrium, moving from individual structures to associated structures as supercomplexes, and adapting their assembly to changes in energy metabolism (Acín-Pérez *et al.*, 2008).

The association of respiratory complexes into supercomplexes increases efficiency of the electron flow between the respiratory chain complexes, decreasing electron or proton leakage and reducing the diffusion distance of the ubiquinone and cytochrome c electronic transporters (Baracca *et al.*, 2010).

In mammals, most of the complex I (90%) is assembled in supercomplexes, while only 50% of complex III and approximately 20% of complex IV are associated in the supramolecular species (Schägger 2001; Schägger & Pfeiffer 2000). Variants of supercomplexes have been described. Complex I forms a stable association with complex III dimer, giving rise to the $I+III_2$ supercomplex, and sequestering a subpopulation of CoQ molecules preferentially dedicated to transferring electrons from NADH.

In mammals, the dimeric complex III can be associated with complex IV, forming the supercomplex III_2 + IV. This interaction defines two pools of cyt c: one present the respirasome that is preferentially dedicated to NADH-derived electrons and the other engaged in CIII + CIV complexes (lacking CI)

that is preferentially dedicated to transferring electrons from $FADH_2$ enzymes. However, the majority of CoQ and cyt c remains unbound to supercomplexes. (Enríquez, 2016b; Moreno-Loshuertos and Enríquez, 2016).

Supercomplex $I+III_2$ can associate with one copy of complex IV, forming the supercomplex $I + III_2 + IV_1$, also called respirasome (Vonck and Schäfer, 2009; Althoff *et al.*, 2011; Dudkina *et al.*, 2011). It has been postulated that the respirasome may bind up to four copies of CIV, but no experimental support for this claim has been provided.

Different associations heve been described in different organisms, i.e.: Y. lipolytica, N. crassa and P. anserina in which CI, $CIII_2$ and CIV can be interacting with alternative stoichiometries (Krause *et al.*, 2004; Marques *et al.*, 2007; Nübel *et al.*, 2009).

The first demonstration that the respirasome is fully functional, was provided by its isolation and functional analysis from mice cells (Acín-Pérez *et al.*, 2008). The respirasome structure has been characterized as having 190 Å height and 300 Å length, resulting the largest supercomplex of the mETC (Guo *et al.*, 2017).

There is a structural interdependence between the complexes of the respiratory chain since the formation of supercomplexes is necessary to maintain the stability of their individual components (Figure 6).

It has been shown that mutations in genes encoding subunits of complex I may affect the stability of other complexes, which in turn may lead to an enzymatic deficiency of complexes I and III, or complexes I and IV (Budde *et al.*, 2000; Ugalde *et al.*, 2004; Saada *et al.*, 2012).

Moreover, the absence of complex III and cytochrome c transporter in mammals may result in a decrease of the levels of complex I (Acín-Pérez 2004) and pathogenic mutations in subunits or complex III assembly factors, leading to combined deficits of complexes I and III, and even complex IV in the affected tissues(Lamantea *et al.*, 2002; Fernandez-Vizarra *et al.*, 2007; Morán *et al.*, 2010).

Finally, mutations in CIV subunits may cause secondary deficiencies of complex I (D'Aurelio *et al.*, 2006; Guarás *et al.*, 2016). The structural dependency of CI on CIII and CIV deficiency, has been explained by the CoQ redox status that enables the cells to adjust the amount of NADH dehydrogenase

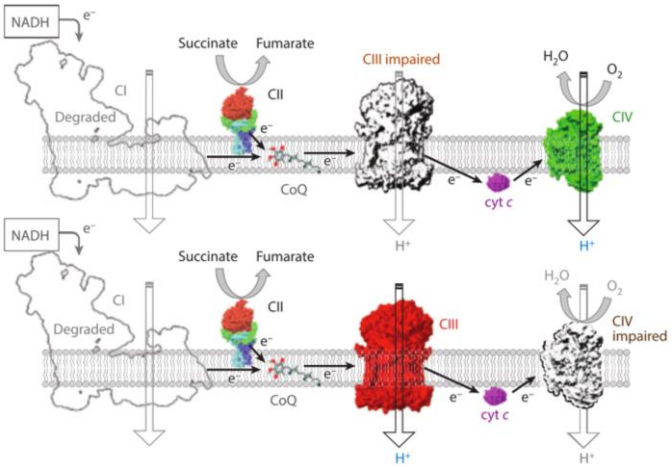

Figure 6. mETC components under CIII & CIV impairement from (Enríquez, 2016a). Lack of CIII & CIV promotes degradation of CI just after its assembly and normal assembly of the rest of the complexes.

(CI). In all of them CoQH2 accumulation triggers RET and causes localized damage to CI components.

Mitochondria perform numerous functions, produce ATP and many biosynthetic intermediates while also contribute to cellular stress responses, autophagy and apoptosis. Therefore mitochondrial dysfunction, firstly discovered in 1960 (Luft *et al.*, 1962), has been linked to a wide range of degenerative and metabolic diseases, cancer, and aging (Wallace, 2005; Nunnari and Suomalainen, 2012).

Findings on a large number of diseases due to mtDNA mutations, can explain the role of this genome in different processes, revealing inadequacies in the mitochondrial electron transport chain (mtETC) models (Saiki *et al.*, 1985; Holt, Harding and Morgan-Hughes, 1988; Kroemer and Reed, 2000; Petros *et al.*, 2005).

Mitochondrial diseases can manifest both in children and in adults and can affect multiple organs. Thus, they can deregulate synthesis, folding, amount or assembly of any of the proteins involved in the processes of respiration, replication of mtDNA, transcription or synthesis (Suomalainen and Battersby, 2017).

I.2.4 Endoplasmic reticulum (ER) : ER stress and Unfolded Protein Response

The endoplasmic reticulum (ER) is a cellular organelle that forms an interconnected network of flattened, membrane-enclosed sacs or tube-like structures known as cisternae, which are continuous with the outer nuclear membrane. There are two types of ER, rough, studded with ribosomes, and smooth-extended through the cell (Lodish *et al.*, 2003).

The ER is the main site of synthesis, storing, modifying and transport of newly synthesized proteins (Lodish *et al.*, 2003), as well as the main center of storage, signaling and regulation of intracellular Ca^{2+}.

A wide variety of alterations such as hypoxia, lack of nutrients, redox imbalance, changes in Ca^{2+} homeostasis, increased protein translation, virus infections, chemical substances and mutations can generate an imbalance between the capacity of ER folding and the amount of proteins to be folded, causing the accumulation of unfolded or poorly folded proteins and thus generating ER stress. The resulting fate of the cell is either survival or apoptosis, depending on the cellular response to the stress. An accumulation of unfolded or misfolded proteins in the endoplasmic reticulum (ER) leads to stress conditions. To mitigate such circumstances, stressed cells activate the unfolded protein response (UPR), which orchestrates the recuperation of ER function. The UPR is a signal transduction pathway, activated to re-establish protein homeostasis within the mitochondrial protein-folding environment (Xu, Bailly-Maitre and Reed, 2005; Hussain and Ramaiah, 2007; Cnop, Foufelle and Velloso, 2012).

The UPR of eukaryotic cells consists of three different mechanisms: (i) translational attenuation to limit further protein loads (Harding, Zhang and Ron, 1999) (ii) transcriptional activation of genes encoding factors involved in ER protein folding and degradation (Gething and Sambrook, 1992) and (iii) ER-associated degradation (ERAD), which restores the folding capacity through the clearance of unfolded or misfolded proteins by enabling their retro translocation from the ER into the cytosol via the ubiquitin- proteasome system (Mori, 2000)

In mammals, the UPR signaling pathway is initiated by three ER membrane-associated sensors: activating transcription factor-6 (ATF6), inositol-requiring transmembrane kinase/endoribonuclease 1 (IRE1) and double-stranded RNA-dependent protein kinase (PKR)-like eukaryotic initiation factor 2α

(eIF2α) kinase (PERK). This system is dynamically interconnected with autophagy processes, acting as an inductor or inhibitor (Kadowaki and Nishitoh, 2013; Rashid *et al.*, 2015) (Figure 7).

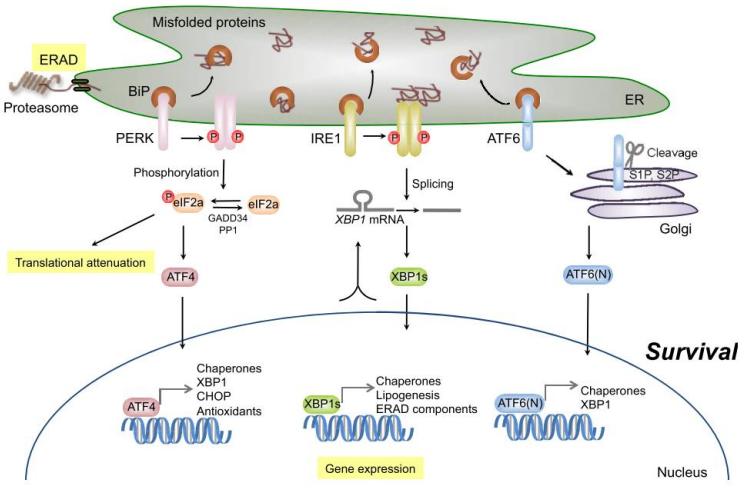

Figure 7. Survival signaling under ER stress conditions. The accumulation of misfolded proteins activates three ER stress sensors: activating transcription factor-6 (ATF6), inositol-requiring transmembrane kinase/endoribonuclease 1 (IRE1), and double-stranded RNA-dependent protein kinase (PKR)-like eukaryotic initiation factor 2α (eIF2α) kinase (PERK) (Kadowaki and Nishitoh, 2013)

ATF6 is activated following cleavage with S1P and S2P, after transport to the Golgi, inducing the expression of ER chaperones and XBP1. Activated IRE1 induces the splicing of XBP1 mRNA, and the resulting spliced XBP1 protein (XBP1s) controls the transcription of ER-resident chaperones and genes involved in lipogenesis and ER-associated degradation (ERAD) (Kadowaki and Nishitoh, 2013).

Activated PERK enables the phosphorylation of eIF2aK3 under ER stress conditions, that translocates to the nucleus where the signaling cascade induce the expression of genes involved in the scavenging of ROS and autophagy. eIF2aK3-dependent nuclear translocation of ATF4 results in upregulation of several genes involved in MTORC1 inhibition, including SESN2, DDIT4, and DDIT3. SESN2 and DDIT4 act directly on MTORC1, whereas DDIT3 upregulates TRIB3, which minimizes MTORC1 activity via AKT1 inhibition (Zhao *et al.*, 2013).

I.2.5 Mitochondrial CYTb mutation

Mitochondrial pathologies associated with mutations in CIII are clinical heterogeneous and rare diseases, mostly due to mutations in mitochondrial CYTb. Mutations in the cytochrome b gene are the most frequent cause of enzyme deficiency of complex III (Andreu *et al.*, 1999).

Complex III deficiencies disrupt the activity not only of CIII, but also of complex I (Lamantea *et al.*, 2002). Moreover CIII dysfunction destabilizes CI, by making CI susceptible to active degradation within mitochondria (Acín-Pérez 2004) as described in chapter I.2.3.

Exercise intolerance is a mitochondrial myopathy that is associated with at least 9 different mutations in the mt-CYTb gene (Dumoulin *et al.*, 1996; Andreu *et al.*, 1999; Legros *et al.*, 2001). All these mutations are manifested in heteroplasmy and are associated with different diseases, such as cardiomyopathy (Marin-Garcia *et al.*, 1996; Valnot *et al.*, 1999; Andreu *et al.*, 2000), respiratory problems (Hayashi *et al.*, 2015), septic-optic dysplasia (Schuelke *et al.*, 2002),

mitochondrial encephalopathy (Keightley *et al.*, 2000) and multisystemic failure (Wibrand *et al.*, 2001).

However most of the patients with these mutations have isolated myopathy with torn red fibers, characterized by exercise intolerance, weakness and myoglobinuria. It is important to note that there are mutations in mt-CYTb, which can be associated with a combined deficiency in CI + CIII (Andreu *et al.*, 1999; Bruno *et al.*, 2003).

To investigate the molecular cause of this observations human and mouse cell models of complex III deficiency has been used. Our laboratory isolated a mouse cell presenting a defect in complex III, due to a single base substitution within the CYTb gene, which is deleterious: a G15263A transition that mutates the E373 to K at the carboxy terminus of the CYTb protein. The consequence is that the protein is translated by cannot be properly folded and therefore is sent for degradation (Acín-Pérez 2004).

II. IMAGING MITOCHONDRIA

II.1 Electron Microscopy

II.1.1 Transmission electron microscopy (TEM)

Since 1950s, various forms of electron microscopy (EM) have provided a detailed view on the membrane architecture of these organelles. This microscope uses a beam of accelerated electrons as a source of illumination, with a resolution of 50pm.

Sjöstrand and Palade led the pioneering work on electron microscopy of mitochondria. These studies recognized that mitochondria contained more than one membrane system leading them to different observations.

Palade observed the internal membrane compartments defining them as the mitochondrial cristae, the mitochondrial inner membrane is convoluted in a baffle-like manner with broad paths around them (Palade, 1952). On the other hand, Sjöstrand described the mitochondria as a organelle with double limiting membrane that has internal membrane-bounded compartments forming the septa that divide the matrix into many compartments (Sjöstrand, 1956).

In 1966, Daems and Wisse noted that the frequency of interaction between the intermembrane and the cristae was much smaller than Palade model. In this way they propose that cristae are connected to the inner boundary membrane via tubular structures characterized, termed as crista junctions (CJs) (Daems and Wisse, 1966) (Figure 8).

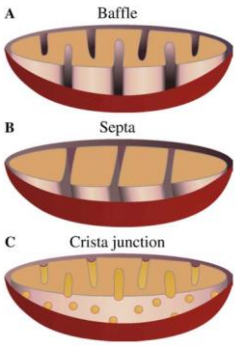

Figure 8. Different models for the organization of the mitochondrial inner membrane from (Zick, Rabl and Reichert, 2009) (A) Baffle model according to Palade 1952. (B) Septa model proposed by Sjöstrand 1956 (C) Crista junction model proposed by Daems and Wisse 1966.

These controversies in mitochondrial compartmentation lead the creation of new 3D imaging technology, electron microscopic (EM) tomography. The use of this technique leads the establishment of this currently widely accepted model: The cristae junction model (Figure 9).

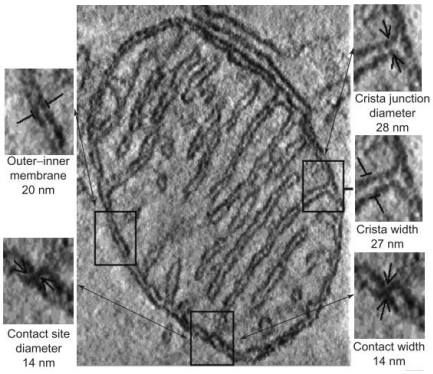

Figure 9. A single section through the electron microscopic tomography of the mitochondrion from (Frey and Mannella, 2000). Various structural features are outlined: Outer−inner membrane, contact site diameter, crista junction diameter, crista width and contact width.

II.1.2 Scanning electron microscopy (SEM)

Scanning electron microscopy (SEM) is a high-resolution surface imaging technique that produces images of a sample by scanning the surface with a focused beam of electrons. This technique has proven evidences and phenotypic differences in three-dimensions for organelle associations as well as the identity of larger mitochondria (Cascarano *et al.*, 1995; MacDonald, Fowle and Woods PhD, 2017) (Figure 10).

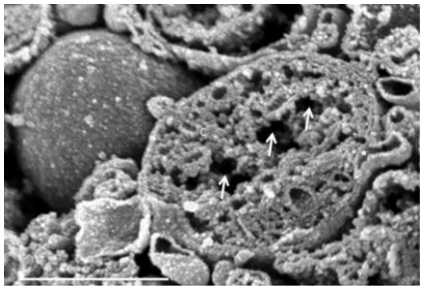

Figure 10. Mitochondrion fractured across a central plane allows the complete visualization of outer membrane, inner membrane, cristae (denoted with C) and inner membrane spaces (indicated with white arrows). Scale bar 500nm. Figure obtained from (MacDonald, Fowle and Woods PhD, 2017)

II.1.3 Cryo – electron microscopy

This technique determine three-dimensional (3D) structures from projection images of molecular complexes preserved in their native, non-crystalline state (Zhou, 2011). In the frozen state the structure can be preserved to atomic resolution. In 2017, Jacques Dubochet, Joachim Frank and Richard Henderson were awarded the prize Nobel for their work in developing cryo-electron microscopy (cryo-EM).

Perhaps the most commonly used variant of cryo-electron microscopy is single-particle analysis. In this technique, data from a large number of 2D projection images, of protein complex in different orientations, generate a 3D reconstruction of the structure (Orlova and Saibil, 2011).

The respiratory complexes have been analyzed using this technique, among the supramolecular assembly forms that we found in the mETC, the structure characterization of CI, $CIII_2$ and CIV interaction has been the most studied.

Reports in bovine heart shown 9Å resolution in cryo-electron microscopy structure of the major supercomplex I+III_2+IV respirasome (Sousa *et al.*, 2016). Moreover, an increase of resolution was obtained in porcine and ovine heart at 5.4 Å (Gu *et al.*, 2016; Letts, Fiedorczuk and Sazanov, 2016) and better resolved 4.0 A˚ cryo-electron microscopy structure in porcine (Wu *et al.*, 2016) (Figure 11A-B)

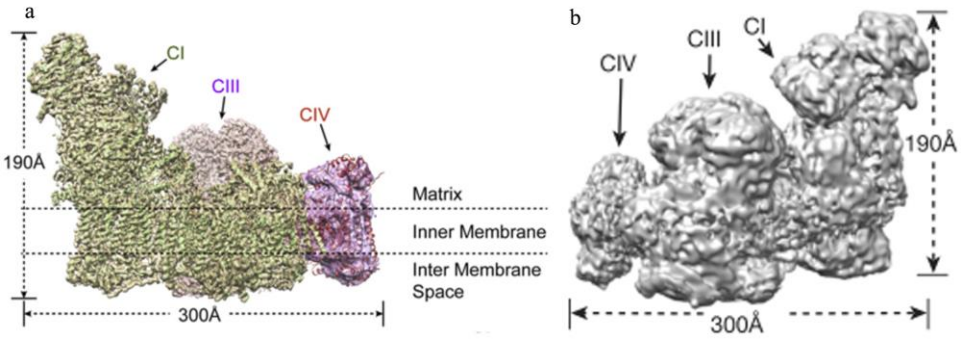

Figure 11. A) The CI, CIII, and CIV maps with the cartoon presented models after soft mask subregion refinement aligned to the 4.0 A˚ from the Cryo–EM map from (Wu *et al.*, 2016). **B)** Cryo–EM structure of the respirasome I+III2+IV from (Gu *et al.*, 2016).

Interestingly, two distinct forms of supercomplex I+III_2+IV has been resolved in ovine heart at the resolution of 5.8 Å and 6.7 Å, respectively. The first described as 'tight' form and the second as 'loose' form, which may represent different stages in supercomplex assembly or disassembly (Letts, Fiedorczuk and Sazanov, 2016).

Recently low-resolution architecture of the human respiratory 'megacomplex' CI_2+$CIII_2$+CIV_2 has been reported, which seems to represent a minor subpopulation of supercomplexes (Guo *et al.*, 2017). From previous studies about the interaction between CII and the other mammalian electron transport chain complexes: CI, CIII, and CIV (Acín-Pérez *et al.*, 2008; Schon and Dencher, 2009; Lapuente-Brun *et al.*, 2013), evidences for the addition of CII into the megacomplex model has been studied but remains to be obtained.

II.2 Optical and Fluorescence Microscopy

In the 17th century for the first time scientists could visualize living organisms under an optical microscope,, and Ernst Abbe was the first to derive a concise mathematical law that quantifies the optical resolution limit as a function of the illumination wavelength in any optical system with a circular aperture: (E. Abbe, 1873):

$$d = \lambda /(2n\sin \alpha) = \lambda / 2NA$$

The Abbe's Law describes the light of wavelength λ that excites a sample, in a medium with a refractive index of n, where α is the half-angle from which light is gathered by the objective and NA the numerical aperture of the objective. Therefore, d is the optical resolution limit or minimal distance between two objects to be separated. By the Abbe law, the shorter is the monochromatic wavelength

the better is the resolution, while to further increase resolution high NA values are also necessary at any given λ. In numerical terms, since the visible, non toxic light is in the range of 400 – 700 nm, the resolution limit of standard microscopy is in the order of 200-300 nm, that is insufficient for imaging individual molecules or even molecular complexes, but well suited for visualize intracellular larger structures. The Abbe's law also regulates the axial (i.e. Z) resolution, perpendicular to the plane of the objective:

$$d = 2\,\lambda/NA^2$$

and explains how the axial resolution degrades to 500-1000nm.

II.2.1 Fluorescence Microscopy

Over the past decades, fluorescence microscopy has become an essential tool for increasing the image contrast and detectability of a wide variety of biological structures, pathways, and dynamics in living cells, tissues, and whole animals. In contrast to other techniques (such as electron microscopy), fluorescence imaging is compatible with living model organisms and cells in culture.

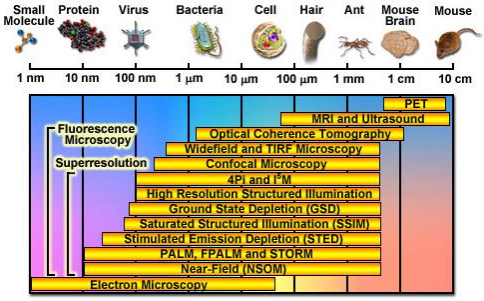

Figure 12. Spatial resolution of biological imaging techniques. The image represented the resolution of each microscope.

Fluorescence microscopy is the most important approach for biological imaging due to the shortcomings of the alternative techniques. It is the only method that allows non-invasive imaging of thick samples under physiological conditions in three dimensions.

Live cell imaging of mitochondria and other cellular structures can be performed by tagging resident mitochondrial proteins with fluorescent proteins or by adding specific mitochondrial targeting sequences to fluorescent proteins (Okamoto, Perlman and Butow, 2001) Studies of re-localization in living cells of different fluorescent proteins by fusion with mitochondrial complexes have addressed mitochondrial dynamics (Muster *et al.*, 2010).

In terms of spatial resolution, other techniques including positron-emission tomography, magnetic resonance imaging, and optical coherence tomography can generate images at resolutions between 1 mm and 10 µm. Electron microscopy and scanning probe techniques feature the highest spatial resolution between 1nm and 100 µm. Between these two extremes in resolving power lies optical and fluorescence standard microscopy (Figure 12).

However, in the recent years, the resolution limit dictated by the Abbe's law has been circumvented with the discovery of super-resolution approaches. In this way to have high resolution we need short wavelength and high NA values.

II.3 Nanoscopy

In 2014, Eric Betzig, Stefan W. Hell and William E. Moerner were awarded with the Nobel Prize in Chemistry for the achieving a relevant increase of optical resolution in fluorescence microscopy. They were able to exploit the photophysical properties of some fluorescent molecules that can be used to tag molecular structures and cellular organelles and obtained the first super-resolved and single molecule images in cells using visible light.

II.3.1 Single Molecule Localization Microscopy (SLM)

One major utility of super-resolution techniques, referred as PALM, FPALM and STORM, uses temporal control of the excited state of fluorophores to sequentially identify single non-overlapping emitters in time and space (Hess, Girirajan and Mason, 2006; Rust, Bates and Zhuang, 2006)

Cells with labeled mitochondria have been used in different implementations of super-resolution microscopy, including the first manuscript using PALM microscopy (Betzig *et al.*, 2006). This technique allows the relative distribution or regions of interaction between multiple proteins to be discerned at the nanometer level (Figure 13A)

Moreover utilizing STORM, (Shim *et al.*, 2012) succeeded in visualizing mitochondrial inner membrane dynamics in living cells using a photoswitchable membrane probe, MitoTracker Red. In the same way STORM has been used to study protein distributions in mammalian mitochondria (Jakobs and Wurm, 2014) (Figure 13B).

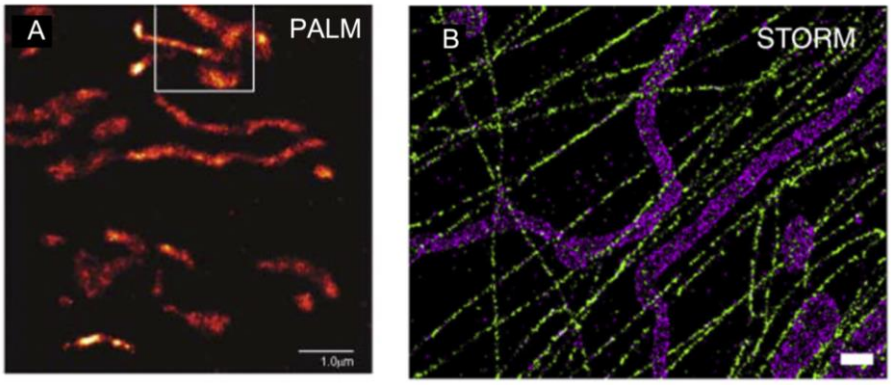

Figure 13. A) dEosFP-tagged cytochrome-C oxidase import sequence localized within the matrix of mitochondria by PALM technique modified from (Betzig *et al.*, 2006). **B)** Two-color STORM images showing the interaction between mitochondria (magenta) and microtubules (green) from (Jakobs and Wurm, 2014).

Single molecule fluoresce microscopy allows the localization of single molecules of mitochondrial complexes in fused mitochondria and the study of the different states of fusion, showing consecutive mixing of OXPHOS complexes and the progressive homogenization of them (Wilkens, Kohl and Busch, 2012).

II.3.2 Stimulated Emission Depletion Microscopy (STED)

Improvements on confocal microscopy have prompted research into increasing the numerical aperture as well as bypassing the diffraction limit. Stimulated Emission Depletion Microscopy, STED, was first developed in 1994 by Hell and Wichmann (Hell and Wichmann, 1994) and awarded in 2014 with the Nobel prize in chemistry "for the development of super-resolved fluorescence microscopy". The technique improves the resolving ability of fluorescence microscopy, enabling to visualize details as small as ~30nm (Dyba and Hell, 2002). Later on, focal spot size was reported as 16nm (Westphal and Hell, 2005).

Incoming light into the fluorescent probe increases the energy state of the electrons changing its organization to an excited state S_1. The absorbed energy returns to the ground state S_0 as fluorescence. Due to vibrational or rotational states, the fluorophore loses energy and the emitted fluorescence has less energy than the absorbed light. This energy difference is used to separate the excitation light and the spontaneous emission (Blom and Brismar, 2014).

The concept of STED microscopy is to suppress the spontaneous emission around the periphery of the fluorescence focal spot by stimulating emission of photons using a laser pulse that is red-shifted with respect to the excitation laser.

STED microscopy uses two laser beams: the excitation beam and high intensity spatially modified beam, called STED beam. In this way after the molecule has been excited from the ground state to a high level and naturally relaxed, it can be excitated again to the ground state with an other photon. The excess of energy can be removed via an exact copy of stimulated light (Figure 14B).

The photons from stimulated emission are at the same wavelength, phase, polarization and direction as the STED beam. The wavelength of the STED beam is set to overlap the tail of the emission spectrum, such that the photons that have a longer wavelength compared with the majority of spontaneous emission photons can be filtered out. By overlaying a doughnut shape STED beam on

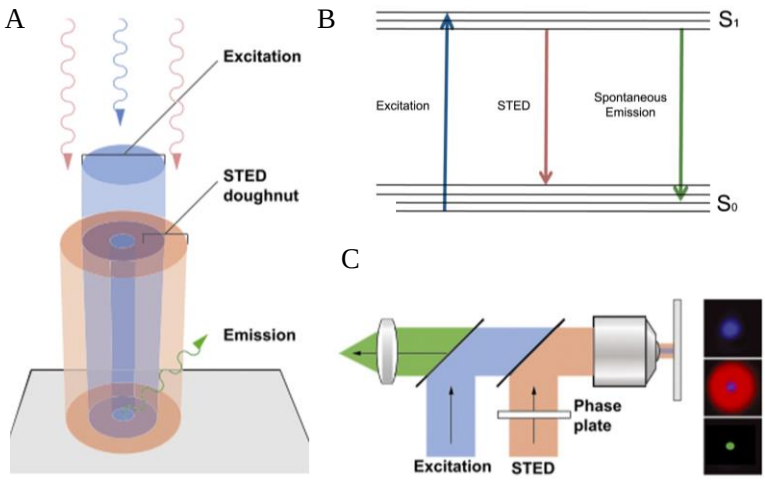

Figure 14. A) Laser light is used to excite (blue) fluorescence emission (green) in the area of focus. A sculptured STED focus (red) is used to selectively turn off emission in the outer rim allowing better separation of fluorescent entities from (Blom and Brismar, 2014). **B)** Jablonski diagram for STED. Adapted from (Hell, 2003). Molecules excited to S1 state are "switched off" by STED beam to S0 state under the STED beam and emit longer wavelength photons than spontaneous emission photons. **C)** Schematic diagram of an optical STED microscope, the depletion beam (red) into a 'doughnut-shape' in the focal plane, overlapped with the excitation beam (blue), and the resulting effective detected fluorescence emission (green) from (Blom and Brismar, 2014).

the excitation beam, molecules at the doughnut center are allowed spontaneous emission, while others under the STED beam are switched off and do not emit spontaneous photons (Figure 14A and 14C).

Both lasers are still diffraction-limited, but the STED laser has a modified beam profile with a central zero intensity (like a doughnut). If the STED pulse intensity is greater than the molecular emission depletion threshold then the fluorescence area will be limited to a small region around the STED zero intensity center. Increasing the intensity of the STED laser will further decrease the fluorescence around the central zero.

II.3.3 3D Super Resolution Microscopy

The first applications to mitochondria of 3D imaging was the EM tomography of rat liver isolated mitochondria (Frey and Mannella, 2000) . Moreover, the same Authors also contributed to develop the technique for to in situ imaging. The images acquired were processed to generate in-silico models as the one shown in Figure 15.

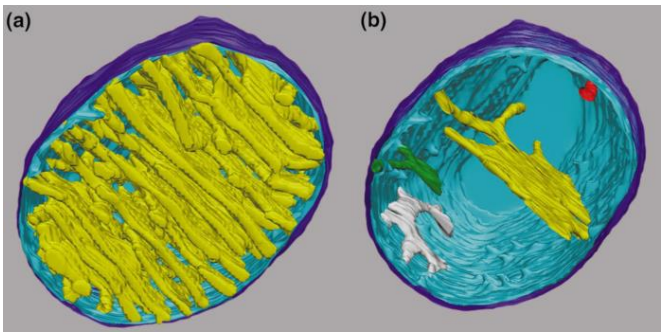

Figure 15. Computer models generated from segmented 3D tomograms of a mitochondrion in chick cerebellum from (Frey and Mannella, 2000)

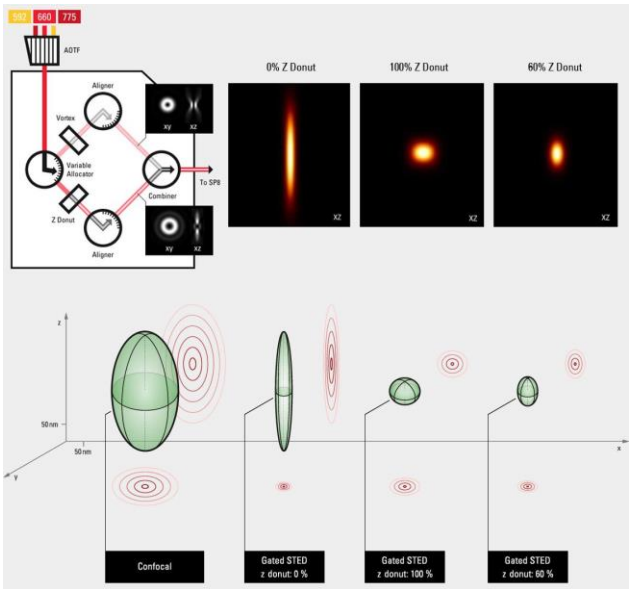

Figure 16. Representation of the resolution improvements by allocating the light to the two STED pathways: the best lateral resolution is achieved by the classic vortex donut, the best axial resolution by the novel z donut, from Leica Microsystems.

In STED the creation of a depletion-focus, results in a resolution improvement confined in the lateral (*xy*) plane but still diffraction-limited in the axial (*z*) direction. Consequently STED images are super-resolved in the lateral directions, but not along the optical axis (Gould *et al.*, 2012). Most of the STED images in literature are obtained with this configuration.

Some STED equipment (ex: Leica Gated STED-3X-WLL SP8), have the characteristics like the one on Figure 14. The microscope can apply a double depletion geometry, depleting along the 3 x, y, z directions, and obtaining a much more accurate identification of the image along the x, y, z space (Figure 16).

OBJECTIVES

Evidences of the co-existence of supercomplexes (SCs) and free complexes in the mETC proposed by the plasticity model, were obtained by blue native gels and proteomic experiments, however direct observation in situ of the organization of the mETC is still missing.

Nanoscopy has opened new possibilities for the research on mitochondria composition since the resolution of these approaches is in the in the nanometric range.

In this work, we aim at visualizing and quantifying the endogenous distribution of respiratory complexes and supercomplexes in situ.

Although protein components in each complex have been identified, it remains unclear how the balance of the different complexes is achieved. The study of compensatory pathways for OXPHOS deficiency in mtDNA encoded proteins, might lead to the better understanding of the molecular mechanisms involved in the regulation of this system.

Within this thread of the work, lies the present thesis, whose objectives can be divided into the following:

1. Novel *in situ* validation of the plasticity model

2. Compensatory pathways for OXPHOS deficiency

MATERIAL AND METHODS

I. CELL CULTURE

I.1 Cell Lines

In the table above, we show the cell lines used in this work.

Table 1. Cell lines used and specific characteristics.

Cell Line	nDNA	mtDNA	Mutation	mETC	Reference
CYTb ^{Ctrl}	L929	L929	mt-COI T6589C (homoplasmic)	Normal complex assembly	(Acín-Pérez 2004)
CYTb ^{M}	L929	L929	mt-CYTb G15263A→ mutates E373 to K at the carboxy terminus of the CYT b protein mt-COI T6589C (homoplasmic)	CIII deficiency and reduction of CI	
CYTb ^{S}	L929	L929	mt-CYTb G15263A mt-COI T6589C (homoplasmic)	CYTb KO phenotypic rescue	(Lapuente-Brun *et al.*, 2013)
Rho0 ^{Ctrl}	L929	C57BL/6J	-	Normal complex assembly	(Moreno-Loshuertos and Enríquez, 2016)
Rho0	L929	-	No mtDNA	Deficiency in CI, CIII, CIV and CV	
Cox10 ^{Ctrl}	C57BL/6J y 129/Svj	C57BL/6J	-	Normal complex assembly	(Diaz *et al.*, 2006)
Cox10 ^{KO}	C57BL/6J y 129/Svj	C57BL/6J	Cox 10 Knock out (Homozygosis)	No CIV and CI assembly	

I.2 Culture Media

I.2.1 Mice Fibroblast cells

All the cells in this work were grown in DMEM (Sigma D5796), with 4500 mg/L glucose, L-glutamine, and sodium bicarbonate, supplemented with 5% fetal bovine serum (Sigma F7524), 1mm sodium pyruvate, 100 units of Potassium Penicillin and 100 µg of Streptomycin Sulfate per 1 ml of culture media.

CYTb ^{S} cell line was grown in medium lacking glucose but containing 0.9 mg/ml galactose. The mutant cells, CYTb ^{M}, Cox10 ^{KO} and Rho0 were grown supplementing the normal medium with uridine (50µg/ml) since pyrimidine synthesis requires the activity of the enzyme dihydroorotate dehydrogenase.

I.3 Culture Conditions

Cell lines were grown at 37ºC in an atmosphere of 5% CO_2 / 95% air.

In mice fibroblast the medium was changed every 2 days.

I.4 Drugs treatments

Cells were culture under different drugs during the thesis project.

Table 2. Drugs treatments, concentration and duration of the treatment.

Drug	Comercial House	Cat. No.	Exp. concentration	Used	Function
Chloroquine	SIGMA	C6628	20 µg/ml	4h / 24h	lysosomal inhibitors
Tunicamycin	SIGMA	T7765	20 nM	3 days	N-linked glycosylation
GSK 2606414	TOCRIS	5107	1 µM	1 day	Inhibition PERK kinase activity
CCT020312	Merck Millipore	324879	1 µM	3 days	PERK pathway activation

I.5 Growing curves

In order to test how the mutation of each cell line is affecting their ability to grow and to determine de concentration at which different drugs affect the cells we performed cell proliferation test in DMEM supplemented with glucose or galactose. Since cells with deficiency in respiratory function are not able to grow in medium with galactose as substrate, we restricted the uridine supplementation in the cells that needed in control conditions, in order to confirm that the growing capabilities were not due to this nucleotide supplementation.

Multi-day test (0h, 24h, 48h, 72h, 96h) of cell number were made by CYQUANT (Molecular Probes), an ideal high throughput screening of the number of cells. The basis for CYQUANT is the use of a fluorescent dye which exhibit strong fluorescence enhancement when bound to nucleic acids of the healthy cells. For each experiment, we have to add 100µl of 2x detection reagent to 100µl of cells in culture media. Incubation of 30 to 60min at 37°C in the dark is needed prior to fluoresce measurement with green filters

I.6 Hypoxia induction

Hypoxia chamber

Cells were cultured in a chamber “The Invivo2 Hypoxia Workstation” (Cultek) that accurately maintains and controls temperature, humidity, oxygen and carbon dioxide. For our purposes cells were incubated for 72h under1 % O2.

DMOG Induction

In order to induce a chemical- hypoxic condition in our cells DMOG was used (dimethyloxaloylglycine, ENZO Life Science) 1mM for 24 hours under normal O_2 concentration.

I.7 shRNA Interference

By RNA interference (RNAi) the targeted genes were knocked down with high specificity and selectivity. We are going to mediate this technique through short hairpin molecules of RNA (shRNA) against mitochondrial proteases and genes that were delivered by a viral vector. Expression of these genes in CYTBM cells were knocked down using the "Expression ArrestTM GIPZ lentiviral shRNAmir library" developed by Thermo Scientific Open Biosystems.

Optimal multiplicity of infection (MOI) was calculated according to the manufacturer's protocol. $5x10^4$ cells per well were plated in a 24-well plate the day before transduction. The next day, medium was replaced (250 µl DMEM without FBS or antibiotics plus 8 µg/ml polybrene) and virus added at the desired MOI. After 4-6 h, an additional 1 ml of full medium was added and cells were incubated for 48 h. Cells were then examined under a fluorescence microscope every 24 h for reporter expression, and once expression reached an acceptable level, the reduction in the targeted protein content was tested by western blot and qPCR. The shRNA that we used in this work were against the proteases: LonP, YME1L1, Htra2/Omi and ClpP. Algo we used shRNA against mitochondrial genes like NDUFS3 and NDUFA4L2, subunits from complex I.

II. PROTEIN ANALYSIS

II.1 Protein extraction

All the protein extractions were done from culture cell lines on 100mm plates at 80% confluence. The cell pellet was resuspended in 200 µl RIPA buffer and incubated for 15 minutes at 4 °C on a rotating wheel. In last we collected the supernatant obtained from the centrifugation for 15 minutes at 13000 rpm and at 4ºC.

Proteins were extracted with RIPA buffer (Tris-HCl 50mM pH 7.4, NaCl 50mM, Triton X-100 1%, sodium deoxicolate 0.5%, EDTA 5 mM), to which we added an inhibitor cocktail mix (pepstatin 1 ug/ml, leupeptin 1 ug/ml, aprotinin 1 ug/ml, PMSF 1) (Sigma).

II.2 Protein quantification

Protein quantification was carried out by the Bradford method (Bradford, 1976).The calibration curve was constructed with 8 standards having 0, 1, 2, 3, 4, 5, 10, 15 mg/ml of bovine serum albumin (BSA). The protein samples were determined in triplicate by taking 1µl of each sample. All were added 50 µl of the Bradford concentrated reagent (Bio-Rad). Both the samples and standards were taken to a final volume of 200 µl. They were allowed to develop the color (around five minutes) and, finally, the absorbance was read at a wavelength of 595 nm. With the standards of BSA, a calibration line was built. With the equation of this calibration line, the absorbance of the samples was related to their protein concentration.

II.3 SDS electrophoresis

Protein separation electrophoresis was performed on denaturant polyacrylamide gels. Protein samples were incubated for 1 minute at 95 ° C with Loading buffer (50 mM Tris-HCl pH 6.8, 2% SDS, 10% glycerol, 1% β -mercaptoethanol, 0.02% bromophenol blue). Subsequently 20 µg of each protein sample were loaded on a 12.5%, 10% or 15% acrylamide gel, depending on their molecular weight. The electrophoresis was done in Tris-glycine solution at 10 mA per gel during migration in the concentrator gel and when the sample is in the resolving gel we changed to 20 mA per gel.

II.4 Protein detection by Western Blot

Western blot immunodetection was performed on any type of electrophoresis described in this work.

The proteins were transferred to PVDF membrane (Immobilon-FL, 0.45 µm) by transfer into Mini Trans-Blot Cell (Bio Rad), in transfer solution (48 mM Tris, 39 mM glycine, 20% methanol) at 100 volts for one hour 15 minutes. Once the transference was done, the membrane was blocked for one hour and incubated with the primary antibody overnight under agitation at 4°C. After three washes with PBS-tween 0.1% the fluorescent secondary antibody was incubated for one hour.

Membrane developing was done in the Odyssey imaging system (LI-COR biosciences). This technology allows us to use two different wavelengths during the image acquisition, in this way we can reveal two proteins at the same time. For this type of process, we blocked the membrane and prepared the antibodies in Sea Block blocking buffer (ThermoFisher) diluted in PBS. Moreover, membrane developing was performed by chemiluminescence, with Amersham ECL Western Blotting Detection Reagent (Ge Healthcare). In this case we blocked with 5% milk in PBS-0.1% tween and the dilution of the antibodies were done in 0.2% milk in PBS-tween 0.1%.

We specify the antibodies used during the elaboration of this thesis (Table 3). It is also important to note the specific application for each antibody, because not all them worked in the native conditions and in the image techniques we used in this manuscript.

Table 3. Primary Antibodies used in this manuscript

Antibody	Clon	Isotype	Comercial House	Catalog no.	Used
ACTIN	Polyclonal	Rabbit IgG	Sigma	A2066	SDS
Atg5	Monoclonal	Rabbit IgG	Cell Signalling	12994	SDS
Atg7	Monoclonal	Rabbit IgG	Cell Signalling	8558	SDS
BECLIN	Monoclonal	Rabbit IgG	Cell Signalling	3495	SDS
COI/SubI	Monoclonal	Mouse IgG2a	Invitrogen	459600	BN/SDS/STED
COX5A	Polyclonal	Rabbit IgG2a	Abcam	ab110262	BN/SDS/STED
GAPDH	Monoclonal	Mouse IgG1	Abcam	ab8245	SDS
Grp75	Monoclonal	Mouse IgG2b	Abcam	ab2799	SDS
HIF1a	Monoclonal	Mouse	Novus	NB 100-15	SDS
Hif2a	Polyclonal	Rabbit IgG	Abcam	Ab 199	SDS
Hif3a	Polyclonal	Rabbit IgG	Abcam	Ab2165	SDS
HTRA2	Polyclonal	Rabbit IgG	Proteintech	15775-1-AP	SDS
HSP60	Monoclonal	Mouse IgG1	SIGMA	H3524	SDS
LC3A/B	Monoclonal	Rabbit IgG	Cell Signalling	12741	SDS
LONP	Polyclonal	Rabbit IgG	Abcam	Ab103809	SDS
MITOFUSIN 1	Polyclonal	Rabbit IgG	Abcam	Ab104274	SDS
MITOFUSIN 2	Monoclonal	Rabbit IgG	Abcam	Ab124773	SDS
NDUFA4	Polyclonal	Rabbit IgG	Bioworld	BS3883	SDS
NDUFA4L2	Polyclonal	Rabbit IgG	Proteintech	16480-AP	SDS
NDUFA9	Monoclonal	Mouse IgG1	Abcam	ab14713	BN/SDS
NDUFB8	Polyclonal	Rabbit IgG	Abcam	ab74126	BN/SDS/STED
NDUFS3	Monoclonal	Mouse IgG1	Abcam	ab110246	BN/SDS/STED
OPA1	Polyclonal	Rabbit IgG	Abcam	ab42364	SDS
PINK1	Polyclonal	Rabbit IgG	Abcam	Ab23707	SDS
SDHA(Fp70)	Monoclonal	Mouse IgG1	ThermoFisher	459200	BN/SDS/STED
SERPINA3	Polyclonal	Rabbit IgG	Sigma	HPA002560	SDS
SOD2	Polyclonal	Rabbit IgG	Abcam	Ab16956	SDS
TAK1	Monoclonal	Rabbit IgG	Cell Signalling	5206	SDS
p-TAK1	Monoclonal	Rabbit IgG	Cell Signalling	4531	SDS
TIM23	Monoclonal	Mouse IgG2a	BD Transduction	611222	SDS
TOM20	Polyclonal	Rabbit IgG	Santa Cruz	sc-11415	BN/SDS
UQCRC1 (CORE1)	Monoclonal	Mouse IgG1	Abcam	ab110252	BN/SDS/STED
UQCRC2 (CORE2)	Monoclonal	Mouse IgG1	Abcam	ab14745	BN
RIESKE/UQCRFS1	Monoclonal	Mouse IgG2b	Abcam	ab14746	BN/SDS/STED
VDAC	Monoclonal	Mouse IgG2b	Abcam	ab14734	BN
YME1L1	Monoclonal	Mouse IgG	Proteintech	11510-1-AP	SDS
30KDa	Monoclonal	Mouse IgG2a	Invitrogen	459230	BN/SDS/STED

III. MITOCHONDRIA ANALYSIS

III.1 Mitochondria isolation form cell culture

Mitochondrial isolation from cultured cell lines was performed based on (Fernández-Vizarra *et al.*, 2010).

Pellets from cells (50–70 million) were recollected and suspended in 7 volumes of hypotonic medium (sucrose 83mM, MOPS 20mM, pH 7.2) in a potter tube and incubated for 2 minutes in ice. At 600 rpm the sample is homogenized. The resulting homogenate is passed to a falcon tube and 7 volumes of hypertonic (sucrose 250mM, MOPS 30mM, pH 7.2) medium were added. Centrifugation of the sample in a Sorval centrifuge SS34 (F21-8x50y) for 5 minutes at 3000rpm at 4°C was done. Supernatant was centrifuged at 9000 rpm for 12 min at 4 ºC. Mitochondrial pellets were suspended in medium A (sucrose 0.32mM, Tris 10mM, EDTA 1mM, pH 7.4) and centrifuged 3 times at 12000 rpm for 2 min at 4 ºC to wash the sample. Pellets were suspended in an appropriate volume of buffer (1 M 6-amiohexanoic acid, 50 mM Bis-Tris-HCl, pH 7.0) to be at 10 mg/ml and the membrane proteins were solubilized by the addition of digitonin and incubated 5 min in ice.

After 30 min centrifugation at 13,000 rpm, the supernatant was collected, and one-third of the final volume of the sample of 5% Serva Blue G dye in 1 M 6-amiohexanoic acid was added.

III.2 Electrophoresis in Native Conditions Blue Native-PAGE

Polyacrylamide Gel Preparation

Blue Native gels allow the study of protein-protein interactions, separation and analysis of hydrophobic proteins, their complexes and supercomplexes. In this work digitonin-solubilized mitochondrial proteins were separated on blue native gradient gels (3-13% acrylamide)

The solutions needed for the preparation of Blue Native polyacrylamide gels are:

- 3x Gel Buffer: 150 mM Bis-Tris; 1.5 M aminocaproic acid; pH 7.0
- Solution acrylamide-bisacrylamide: 48% acrylamide (w/v); 1.5% bisacrylamide, which was filtered and stored protected from light.
- 20% (w / v) ammonium persulfate (APS).

For the preparation, we used the Biorad Mini protein III 1,5mm and a methacrylate gradient former connected to a one-way peristaltic pump, that pumps the solution into the space between the crystals. Once the gradient gel is done, we added the stacking.

The solutions for the gradient gel are prepared as indicated in Table 4 and for the stacking in Table 5.

Table 4. Composition for Blue Native gels in a 3% to 13% gradient.

Reagent	Acrylamide solution 3%	Acrylamide solution 13%
Acrilamide : bisacrilamide (48:1,5)	0.305 ml	0.866 ml
3x Gel Buffer	1.667 ml	1.111 ml
H_2O milliQ	3 ml	0.713 ml
Glicerol 87%	-	0.643 ml
APS 20%	20 µl	12 µl
TEMED	4 µl	3 µl

Table 5. Stacking composition for Blue Native gels in a 3% to 13% gradient.

Reagent	Volume
Acrilamide : bisacrilamide (48:1,5)	0,25 ml
3x Gel Buffer	1 ml
H_2O milliQ	1,75 ml
Glicerol 87%	-
APS 20%	12,5 µl
TEMED	3 µl

Electrophoresis

The electrophoresis was carried out in the cold, whereupon the gel was mounted on the methacrylate support in the cold chamber.

The buffer was prepared and kept at 4ºC:

- Cathode A buffer: 50 mM tricine; 15 mM Bis-Tris pH 7.0 (4 ° C); comassie Blue G-250 0.02%
- Cathode B buffer: 50 mM tricine; 15 mM Bis-Tris pH 7.0 (4 ° C); comassie Blue G-250 0.002%
- Anode buffer: 50 mM Bis-Tris-HCl; pH 7.0 (4 ° C).

The cathode A and anode buffers were added. The samples were obtained from the solubilization of 100ug of mitochondria and were charged into the wells. The electrophoresis was started at 150 V until the samples completely entered the gel (approximately 30 minutes). After this time, the buffer of cathode A was changed to B for 1h 30min at 300V. After the electrophoresis was completed, two different procedures were performed, depending on the purpose of the experiment. The gel was stained with specific solution to assay mitochondrial complex activities (Section III.3), or use for transfering the proteins to a PVDF membrane immediately after disassembling the gel from its support (Section II.4).

III.3 In-gel activity

Each sample was loaded in duplicate in a Blue Native gel so we can assay the activity of the mitochondrial complexes by the addition of a specific solution and the separation of the native conditions of the protein by Western Blot.

We determined the activities for complex I and CIV.

- Solution for activity of complex I:
  - 0.1 M Tris-HCl buffer, pH 7.4
  - 0.14 mM NADH
  - 1 mg / ml NBT (nitroblue tetrazolium)
- Solution for activity of complex IV:
  - 45 ml 50 mM phosphate buffer pH 7.4 (19ml NaH_2PO_4 0.2M + 81ml Na_2HPO_4 0.2M +100ml H_2O)
  - 25mg DAB (3-3 'diaminobenzidine)
  - 50 mg cytochrome c
  - 5ml H_2O

The reaction was carried out on a rocker and protected from light for 45 mins to 2 hours Both solutions were withdrawn and the reaction was quenched with acetic 10% in distilled water. The stop and fix solution were changed several times to draw nonspecific bindings of the dye.

III.4 Oxygen consumption. SeaHorse

An XF 96 extracellular flux analyzer was used to determine mitochondrial function (XF 96, Seahorse Bioscience). The validity of this method in comparison to classical Clark electrode oxygraph measurements has been proven recently.

The day before the experiment, 10.000 cells per well were cultured with the medium of interest and cultivated at 37°C for 24h. The SeaHorse cartridge with the oxygen sensors was incubated O/N with the calibration medium, in an incubator without CO_2 at 37 ° C. On the day of the experiment the assay medium was prepared. For that we supplemented the Seahorse XF Base medium (without SFB or bicarbonate), with 1 mM pyruvate, 2mM glutamine, 1 M glucose or 2M carnitine with palmitoil CoA and adjusting pH to 7.4. Cells were incubated in that medium for one hour in the incubator without CO_2. The already hydrated cartridge was loaded with oligomycin, FCCP and rotenone + antimycin, diluted in Seahorse XF Base medium up to final concentration of 1 µM and 0.4 µM respectively. The cartridge was placed on the cell plate, so that the sensors came into contact with the cell culture medium. The plate was loaded in the analyzer, which, after the necessary calibrations, started the oxygen consumption measurements. In our case, basal respiration was first evaluated. After injection of oligomicine (ATPase inhibitor), the value of the non-retained respiration was obtained coupled to ATP production. Then, the injection of a decoupling revealed the maximum respiration value in each cell type.

The data obtained was analyzed with the Agilent program Seahorse XF Analyzer. The data was normalized by the DNA content, measured with the CyQUANT ™ fluorescence assay (ThermoFisher).

III.5 RT-qPCR

Cells were collected after trypsinization and the RNA was extracted with the RNeasy Column Clean Up Kit. 2µg of this RNA were used in a retrotranscription process (RT), adding to the RNA a reverse transcriptase enzyme, random primers, dNTPs and an RNase inhibitor (all of them from INVITROGEN). The cycles of the reaction were 25ºC 10 min; 37 ºC 2 hours; 85 ºC 5min.

The resulting cDNA can be used in RT-PCR reaction to evaluate the expression levels in the candidate genes for each cell line. According to the calibration curves performed for each pair of primers, 1/100 dilution of cDNA was used in the reaction.

Quantification of mRNA abundance was performed by real-time PCR detection using a Mastercycler ep Realplex (Eppendorf). For the reaction we need: reaction buffer, sequence-specific primers, Taq polymerase, magnesium, water and SYBR green as a double-stranded DNA-specific fluorescent dye (Power SYBR Green PCR Master Mix (Applied Biosystems). The expression of each gene was normalized to actin mRNA.

The primers were designed using the online tool from Invitrogen:

(http://tools.invitrogen.com/content.cfm?pageid=9716) and were specific for each gene (Table 6).

Table 6. Primer Sequences for qPCR

Gene	PRIMER
Actina Rv	TGA CCG AGC GTG GCT ACA
Actina Fw	TCT CTT TGA TGT CAC GCA CGA T
Afg3l1 Rv	ATC GCT CCC TTT GGA ATT TT
Afg3l1 Fw	TGG TCC TGG TTA GCA TCC TC
Afg3l2 Rv	CCT GGA CCA CCA GTG AGA AT
Afg3l2 Fw	CTG CCT CCG TAC GCT CTA TC
ClpP Rv	TGT AGG CTC TGC TTG GTG TG
ClpP Fw	ATT CAC TGC CCA ATT CCA GA
Clpx Rv	CTG CAT CGT GTC GTA GAT GG
Clpx Fw	AGC AAG CAG AGG CTG AGA AG
Htra2/Omi Rv	CCA AAA TCA ATA GCT GCA TCA
Htra2/Omi Fw	AAG TTT GGA AAC TCT GGA GGT C
Hsp60 Rv	CTT CAG GGG TTG TCA CAG GT
Hsp60 Fw	AAA GAT GGG GTC ACT GTT GC
LonPI Rv	GCA CCT GGA CAG ATC CAC T
LonPI Fw	GAC AGA GAA CCC GCT AGT GC
Parl Rv	TGT GAA CCC AAT GGT GAA GA
Parl Fw	GGG TCG AGT GGA GAA GCA TA
SPG71 Rv	TGG TGA AAC GTG CCA TCT TA
SPG71 Fw	ATT CTT TGG GAA TGC CCT CT
YME1L1 Rv	GTA TTA AGG CAT TAT CTA ATG
YME1L1 Fw	GAA TTA GAT TCT GTT GGT GG

IV. MICROSCOPY AND NANOSCOPY

IV.1 Antibody preparation

Reagent List:

- Anhydrous DMSO (Sigma Aldrich)
- 1M Sodium Bicarbonate Solution
- Dulbeccos Phosphate Buffered Saline (Invitrogen)
- Illustra Nap-5 columns, sephdex G-25 (GE Healthcare)
- Conjugated dye (Table 7)
    - Alexa Fluor 532 (Invitrogen)
    - Alexa Fluor 568 (Invitrogen)
    - 488 STAR (Abberior)
- Secondary IgG:
    - AffiniPure Fab Fragment Goat Anti-Mouse IgG1, Fcγ fragment specific (Jackson Immunoresearch)
    - AffiniPure Fab Fragment Goat Anti-Mouse IgG2a, Fcγ fragment specific (Jackson Immunoresearch)
    - AffiniPure Goat Anti-Mouse IgG, Fcγ Subclass 2b Specific (Jackson Immunoresearch)
    - Goat anti-rabbit IgG (Invitrogen)

For labeling, we dissolved the dye in anhydrous DMSO up to a concentration 10ug/ ul.

Then we prepared the reaction:

65 µg specific secondary IgG

6 µl 1M $NaHCO_3$

2 µg Alexa Fluor Conjugated dye

The reaction tube was wrapped in aluminum foil to protect it from light. We allowed the reaction to proceed for up to 30 minutes at RT on a rocking platform.

While the reaction is processing, we equilibrated the Nap-5 gel filtration column, by running three column volumes of PBS through the column. After the incubation, we added 140 µl of PBS to bring the reaction volume up to 200 µl (the minimum column loading volume) and gently vortex. We added the entire volume to the center of the column and after the last drip we added sufficient PBS to collect the fastest colored band. For IgG, 550 µl of PBS should be required. We added 300 µl PBS and collected the resulting eluent in an Eppendorf tube. We stored the antibodies at 4ºC protected from light, for up to 6 months.

Table 7. List of fluorophores, their excitation, Leica recommended STED laser.

Fluorophore	Excitation (nm)	STED(nm)
Abberior STAR 488	488	592 / 660
Alexa Fluor 532	532	592 / 660
Alexa Fluor 568	568	660 / 775

IV.2 Sample Preparation

IV.2.1 Single and dual color inmunostaining

For immunofluorescence, cells were seeded on coverslips for high resolution microscopy (18mm 1.5H; Marienfeld), fixed in DMEM with 3.7% formaldehyde for 37°C for 15 minutes, washed 4 times with PBS. Samples were submitted to antigen retrieval [100 mM Tris, 5% (w/v) urea, pH 9.5] pre-heated at 95°C for 10 minutes. Samples were washed 3 times for 5 minutes each with PBS and permeabilized with 0.1% Triton X-100 (Sigma) and 0.05% sodium deoxycholate (Merck) in PBS, washed 4 times in PBS and blocked at room temperature for 1 h in 5% Goat Serum in PBS. Primary antibodies diluted in blocking buffer were incubated overnight at 4°C in wet chamber. Secondary antibodies were incubated at room temperature for 2 h. Coverslips were mounted with Prolong Gold (Thermo). Each antibody was applied in series.

Single immunostaining was aimed out for two individual subunits for each mitochondrial complex.

The labeled subunits for complex I were NDUFB8 and NDUFS3. RIESKE and CORE1 were the selected complex III subunits. complex IV subunits were COX5A and SUBUNIT I. Fluorophores combinations were made by the specific IgG (Table 3) of the primary antibody.

Consecutive dual color staining was performed following the table above (Table 8):

Table 8. Antibody combinations for dual inmunostaining.

Complexes	Incubation I		Incubation II	
	mt Subunit	Dye	mt Subunit	Dye
CI + CIII	NDUFB8	532	RIESKE	488
	NDUFS3	532	RIESKE	488
CI + CIV	NDUFB8	532	COX5A	488
	NDUFS3	532	COX5A	488
	NDUFB8	532	SUBI	488
	NDUFS3	532	SUBI	488
CIII + CIV	CORE1	488	COX5A	532
	CORE1	532	SUBI	488
	RIESKE	532	COX5A	488

IV.2.2 Tri color inmunostaining

We have done 3-colour STED images labeling the subunits NDUFB8 (CI), RIESKE (CIII) and COX5A (CIV).

As before, fluorophores combinations were chosen according the specific IgG of the primary antibody. Therefore, we made three serial staining: NDUFB8 (532) + RIESKE (568) + COX5A (488).

IV.3 Confocal imaging

IV.3.1 Mitochondria fussion assay

Cells were grown in 35 mm glass bottom microwell dishes (MatTek corporation) until confluence and then were transfected with mt-DsRed and mito-PAGFP using Metafectene Pro (Biontex) following manufacture instructions: mt-DsRed 1.5µg, mito-PAGFP 1.5µg, 4µl metafectene pro and 100 µl DMEM for 24 hours.

The images were acquired as described in chapter IV.3.2.

IV.3.2 Confocal microscopy

For short-term live cell imaging (7 min), a Leica SP5-Inverted Confocal Microscpe equipped with 37°C incubation chamber with 5% CO_2 was used (Figure 17) that have the specification that we can find in Table 9.

Mito-PAGFP was photoactivated in small ROIs and the diffusion of the photoactivated fluorophores inside the mitochondrial membrane was recorded over time. Frames (512x512pixels) were registered every 0.756 s for 7 min and intensity was analyzed using Volocity Software Routines. Internal normalization was applied.

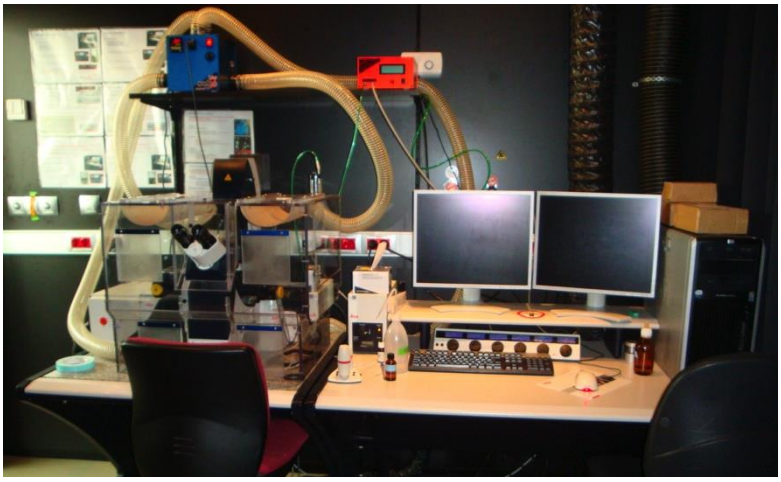

Figure 17. Leica SP5-Inverted Microscope used in this chapter.

Table 9. Leica SP5-Inverted microscope specifications.

OBJECTIVES	HCX PL APO CS 10x 0,4 dry HCX PL APO lambda blue 20x 0,7 multi-imm HCX PL APO CS 40x 1,25 oil HCX PL APO lambda blue 63x 1,2 water HCX PL APO CS 63 x 1,3 Glyc HCX PL APO lambda blue 63x 1,40 oil
INCUBATOR	A full acrylic box covering the microscope allows the regulation of temperature and CO_2 levels for in vivo imaging.
STAGE	motorized stage
DISHES	35 mm dishes and standard microscope slides
ILUMINATION SOURCES	Diode 405 nm Argon Ion Laser: 458,476,488, 496, 514 nm Diode 561 nm HeNe 594 nm HeNe 633 nm
DETECTORS	4 spectral PMT detectors 1 spectral Hybrid PMT detector for fluorescence 1 PMT for transmitted light
CONFIGURATION	Inverted Confocal.
Epi- FILTERS	DAPI,GFP,FITC,Cy3
SCANNER	Galvano/ Resonant

IV.4 Nanoscopy imaging

The STED images were obtained using a Leica Gated STED-3X-WLL-SP8 (Figure 18) inverted microscope equipped with a Leica stimulated emission depletion module consistent in 592 and 660nm lasers, a White Light Laser, and a HCX PL APO 100x/1.40 oil immersion objective. For optimal STED microscopy samples were adjusted to a refractive index of 1.518 and fluorescence was collected through single photon counting detector. All specifications are described in Table 10. The microscope was through LAS AF software (2.0.0 version).

Before depletion, cells were scanned in confocal mode to select a suitable 16x16 μm Region Of Interest (ROI) for super-resolution image acquired at 16 x 16 nm pixel size. Fluorophore depletion was performed always using the 660-nm depletion line. For double or triple stained cells, the depletion was applied sequentially. For 2-color STED images the sequence was ex at 532nm (seq 1) and ex at 488nm (seq 2). For 3-color STED images the sequence was ex at 568nm (seq 1), ex at 532nm (seq 2) and ex at 488nm (seq 3).

3D-STED nanoscopy on 3-color stained cells was performed to recover volumetric information along the mitochondrial network in about 500nm depth inside a cell. For these measurements, the three-color depletion protocol was applied frame-by-frame. To minimize photobleaching, acquisition was carried out using the ultra-fast resonant scanning mode at 8000 frame/sec with line average and frame accumulation.

Figure 18. Leica Gated STED-3X-WLL SP8

Table 10. Leica Gated STED-3X-WLL SP8 Specifications.

OBJECTIVES	HC PL Fluotar 10x/0.3 Dry HC PL Apo CS2 20x/0.75 IMM HC PL Apo CS2 40x/1.3 OIL HC PL Apo CS2 63x/1.4 OIL HC PL Apo CS2 100x/1.4 OIL
INCUBATOR	No
STAGE	motorized stage
DISHES	35 mm dishes and standard microscope slides
ILUMINATION SOURCES	Diode 405 nm White Light Laser: from 470 to 670 nm up to 8 lines STED Depletion Laser: 592nm, 660nm
DETECTORS	2 PMTs full spectral 2 Hybrid detectors full spectral 1 detector for transmitted light
CONFIGURATION	Inverted
Epi- FILTERS	GFP, DsRed, DAPI
SCANNER	Galvano/ Resonant

IV.5 Quantitative image analysis

For 2D-colocalization analysis of 2-color stained cells, images were processed with a Gaussian 0.5-0.7 filter and background subtracted when necessary. The colocalization percentage was obtained using the BlobProb routine (REF) in the ImageJ/Fiji software (National Institutes of Health, USA). The metric was based on measuring the colocalization between objects in which one object is colocalized with another when its center of mass is contained within the other object. We imposed a commutative colocalization. By this strict criterion two or more objects are colocalized when their center of mass are contained within the other object(s) (Fletcher *et al.*, 2010)

For 2D-colocalization analysis of 3-color stained cells, images were first processed with a Gaussian 0.5-0.7 filter and background subtracted. Then the images were explored using 2D vectors 300 nm large and of variable length to select sections of several microns along the mitochondria network. The

intensity profile of each color component was plotted along the vector and internally normalized using the ImageJ/Fiji software. Normalized intensity profiles were overlapped using Graphic Pad Prism software to determine the co-occurrence of CI, CIII and CIV along each vector.

For 3D-colocalization analysis of 3-color stained cells, images were first processed by Image/Fiji software, then a customized Boolean routine was using the Imaris software (Bitplane AG, Switzerland) for quantifying the complexes volumes as described in IV.6.2.

IV.6 Design Analysis Protocol

IV.6.1 FIJI open source command lines for IMARIS

1. First, we apply a 3D crop to remove photobleached frames:
   1.1. Use **Image>Color>Make Composite** to visualize the merged image.
   1.2. To create a subset of the original Z stack, go to **Image>Duplicate**, check "**Duplicate hyperstack**" and specify the desired range of slices.
   1.3. Draw a region of interest to select the desired analysis area, and use **Image>Crop** to reduce the size of the dataset.
2. In the next step proceed with the splitting of channels (**Image>Color>Split channels**). Using Kota Miura´s **Bleach Correction** tool (Schindelin *et al.*, 2016), apply a histogram based bleaching correction to every channel individually (go to **Image>Adjust>Bleach Correction**) (Schindelin *et al.*, 2012).
3. Combine corrected channels into a hyperstack (**Image>Color>MergeChannels**, leaving "**Composite**" option selected).
4. In order to remove noise, apply a 0.5 radius Gaussian filter (**Process>Filters>Gaussian Blur…**) to every channel. This step does not alter the morphology of the objects, as it is show in the intensity profile plot.
5. Finally, export data as an image sequence (**File>Save As>Image Sequence**).

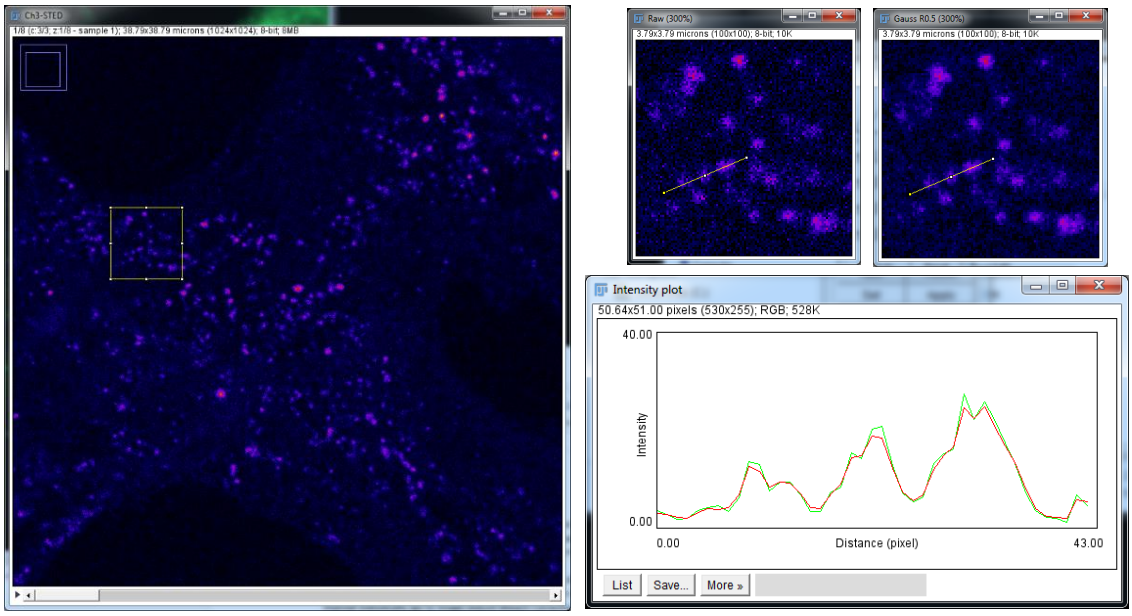

Figure 19. Raw data before and after Gaussian filter. Plot Profile shows that morphology of the objects was not altered (green for raw data, red for Gaussian Blur denoised data).

IV.6.2 Volume analysis by Imaris

1. For this analysis, the Imaris software version 7.7.2 was used (http://bitplane.com)
2. To import STED individual files previously saved by Fiji with Imaris, use **File>Open** and select the first file of the series.
   2.1. It is necessary to go to **Edit>Image Properties** and specify voxel size in microns for X,Y and Z dimensions.
   2.2. Go to the "**Display Adjustment**" window to change channels color, rename every channel and modify Brightness/Contrast to improve data visualization if necessary.
   2.3. STED data will be composed by 3 channels and at least 4 slices in Z axis:

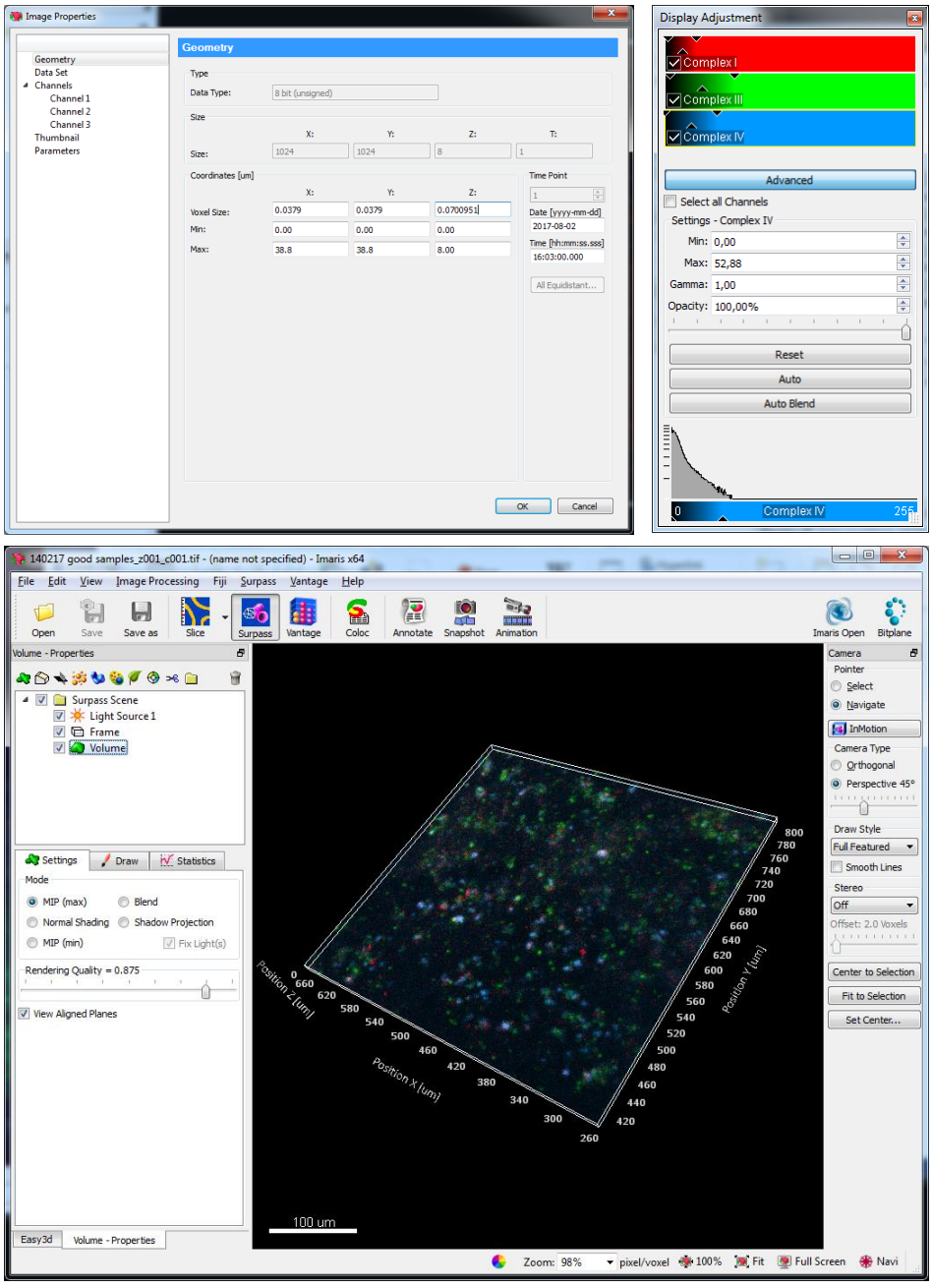

Figure 20. Image Properties and Display Adjustment windows. General view of Surpass Imaris interface.

3. In order to isolate voxels of interest from background signal, an Imaris 3D Surfaces object is created for every channel:

   3.1. From Imaris **Surpass** menu create a new **Surfaces object** and follow the different steps of the wizard:

      3.1.1. Go to step 2 of the wizard, select the source channel and stablish a suitable smooth value (a very high smooth value will cause merging of close objects). For this analysis, a smooth value of 0.0150um was used.

      3.1.2. If background intensity is not even along the image volume, select "**Background Subtraction (Local Contrast)**" option for a better isolation of 3D objects. An estimate size of the object must be provided.

      3.1.3. To finally isolate voxels of interest, an intensity threshold must be applied. Average background mean intensity value from different regions of interest was used as the minimum threshold to select voxels of interest. Splitting of touching objects was not performed as this study is based on voxels, not objects (their irregular shapes can cause problems when doing object splitting).

      3.1.4. The last step of the wizard allows us to filter out 3D objects based on different parameters. A filter based on volume size was applied to avoid quantification of spurious structures with sizes below the system resolution.

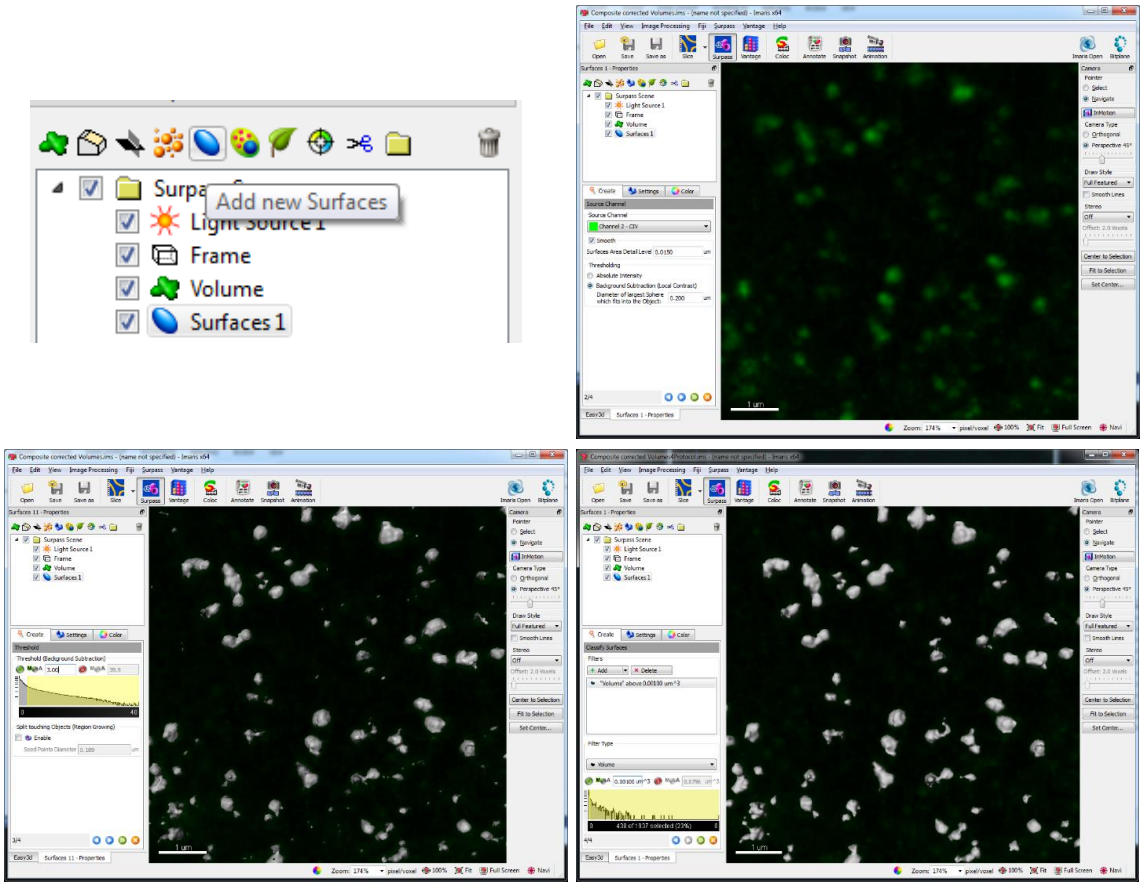

Figure 21. Overview of different steps during Imaris Surfaces object creation.

3.1.5. Once a **Surfaces object** has been created, using it as a 3D mask we can create a binary simplified new channel containing only those voxels selected during the Surfaces object creation:

3.1.5.1. Select the created Surfaces object and go to the **Edit** tab on the menu below (pencil icon). Then select **Mask All.**

3.1.5.2. Select the channel corresponding to the Surfaces object and set background voxels (outside surface) to 0 and foreground voxels to 255 (inside surface). Make sure the option "**Duplicate channel**" is selected to avoid overwriting the source channel. The new masked channel will appear on the **Display Adjustment** window.

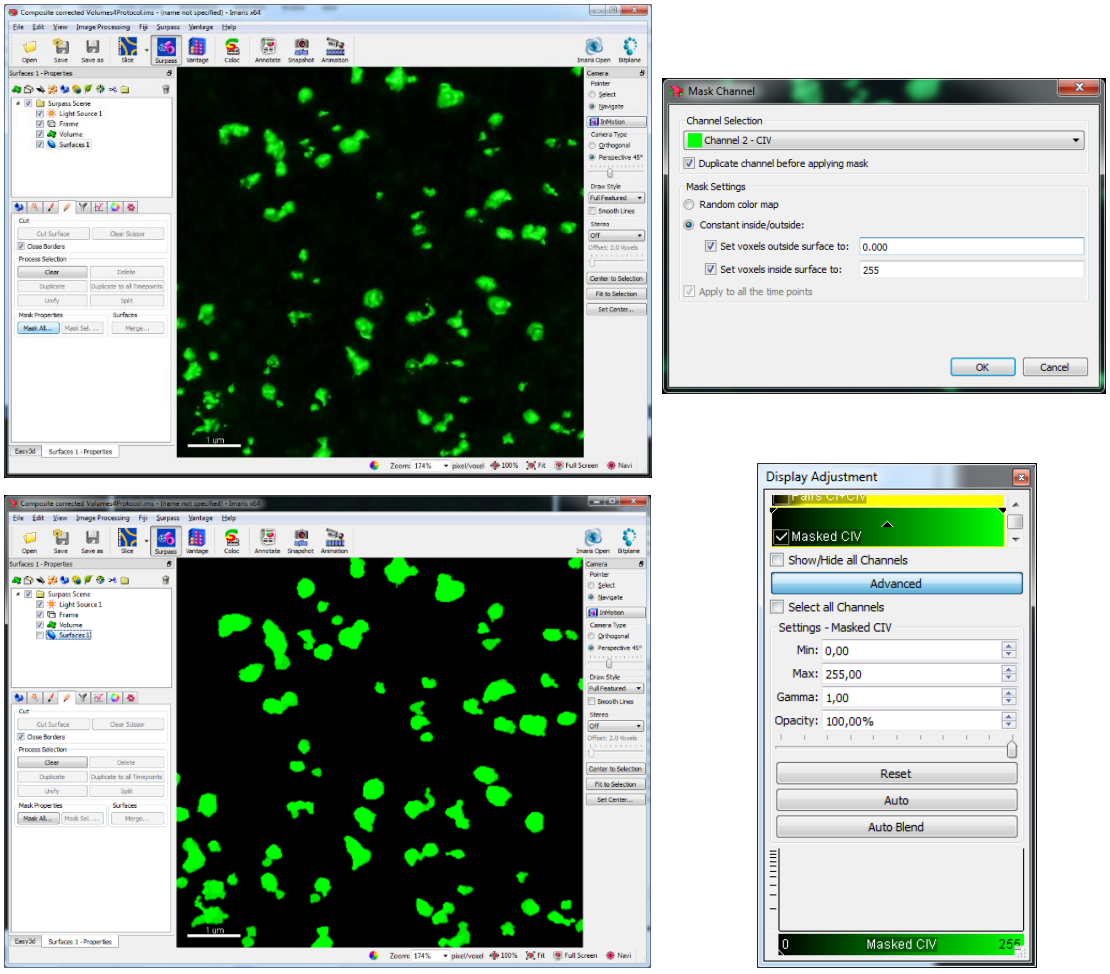

Figure 22. Overview of different steps during Mask Channel process.

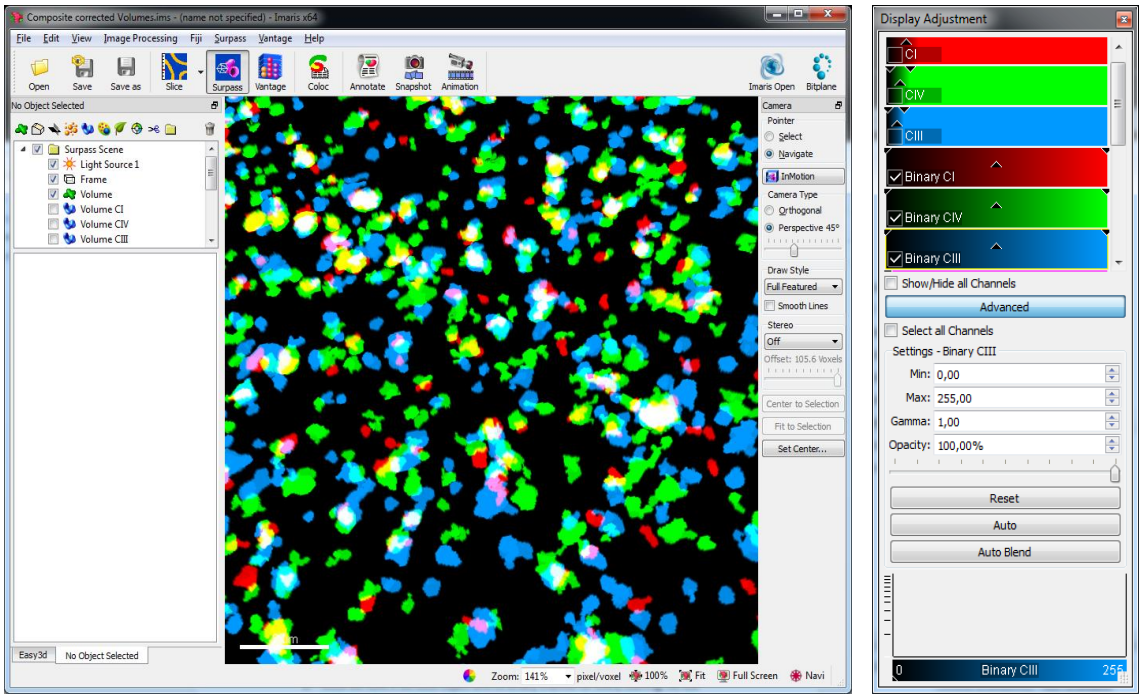

Figure 23. 3D Masks obtained from Imaris Surfaces objects.

4. Once we have a Surfaces object and its binary channel for every staining, we use arithmetic (subtraction) or logical operations (and) between channels in order to obtain the following new binary channels:

Free Complex I

Free Complex III

Free Complex IV

TRIOs (Complexes I, III and IV)

Complex I+III pairs

Complex III+IV pairs

Complex I+IV pairs

4.1. First use Boolean operator AND to obtain common voxels between two binary channels, ej. CI and CIII:

4.1.1. To perform arithmetic operations, go **to Image Processing>Channel Arithmetic's**. For Boolean AND operation use the symbol **&** in between the channels you want to perform the operation, ej. ch4&ch6. It is important to note that you must write the channel number, not the channel name. Use the order in the **Display Adjustment** window to check the channel number (increasing value from top to bottom). Using this AND operator we can create a channel for every Complex pairs: CI&CIII, CI&CIV, CIII&CIV.

4.1.2. Once we have this new channel (it will appear at the bottom of the **Display Adjustment** list), we repeat the AND operation to obtain voxels in common for the three colors, ej. (Result from ch4&ch6) & ch5. The new channel created will be the TRIOs channel (voxels that appear in all the 3 binary channels)

4.1.3. It is important to subtract the TRIO channel to every Pair channel in order to keep strictly only paired voxels. For doing this we use the **Channel Arithmetic's** tool and the arithmetic operation subtraction, ej. ch7-ch8.

4.1.4. The final step will be to obtain only one color voxels (that belong to only one Complex). This can be done using a sequence of subtraction operations, ej. to obtain voxels belonging only to complex I we first subtract complex III binary channel to complex I binary channel, and then we subtract complex IV binary channel to the result of the first subtraction: (Result of ch4-ch5)-ch6.

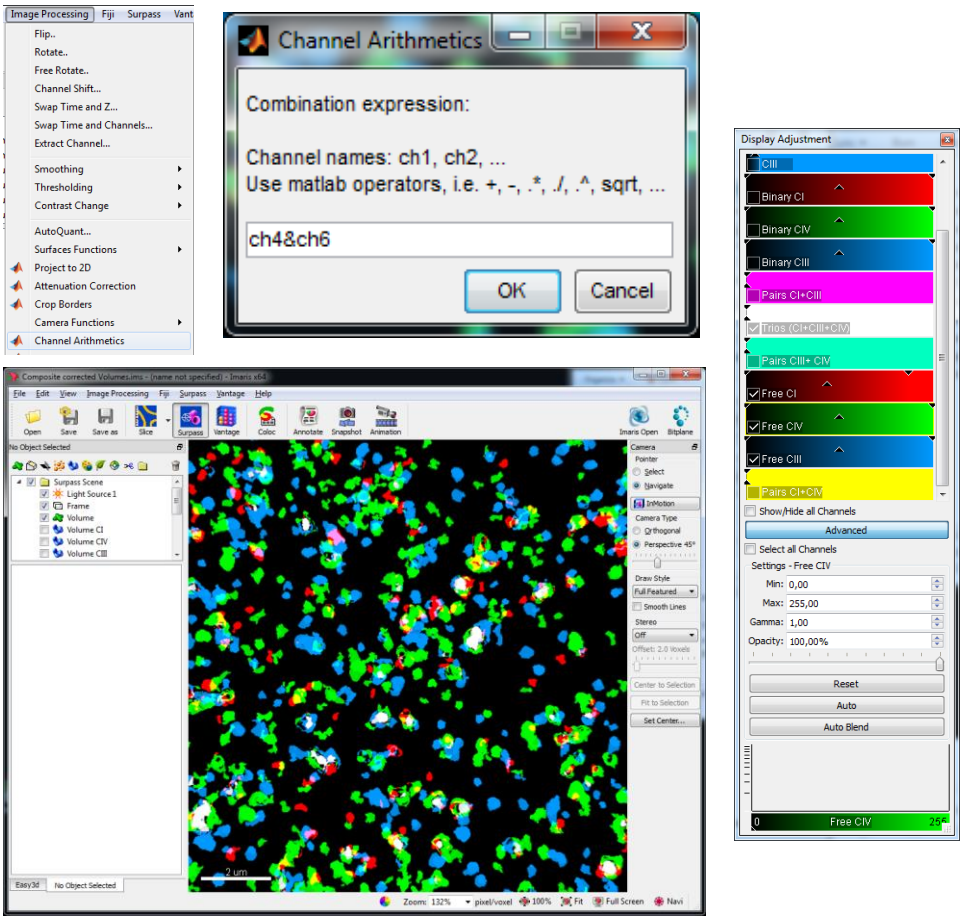

Figure 24. Channel Arithmetics operations window. Final result with free complexed and TRIOs 3D binary channels.

5. In order to measure the total volume of these groups of voxels (TRIOs, Complexes I&III, Complexes I&IV, Complexes III&IV, Free Complex I, Free Complex III, Free Complex IV) an Imaris **Surfaces object** was created for each of them. Objects smaller than the system resolution were discarded. For each new Surfaces object created the total volume occupied by voxels was obtained. Data related with volume can be found selecting a **Surfaces object** and going to the **Statistics** tab.

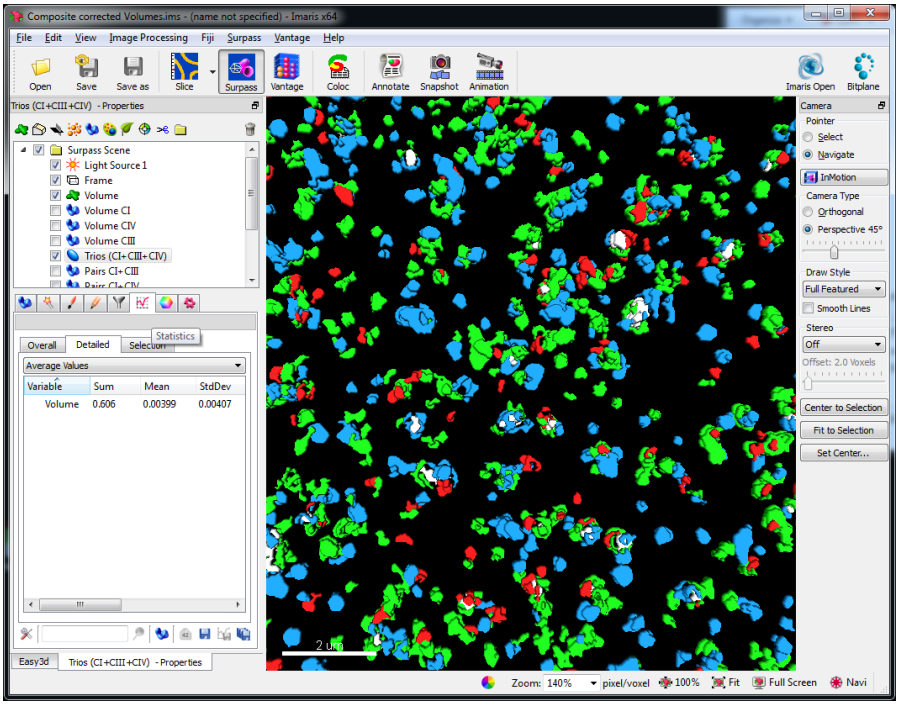

Figure 25. Statistics tab in Surfaces object menu.

6. Total volume data was normalized using the total number of voxels analyzed. Mean and standard deviation was obtained after analysis of three different samples and results were represented.

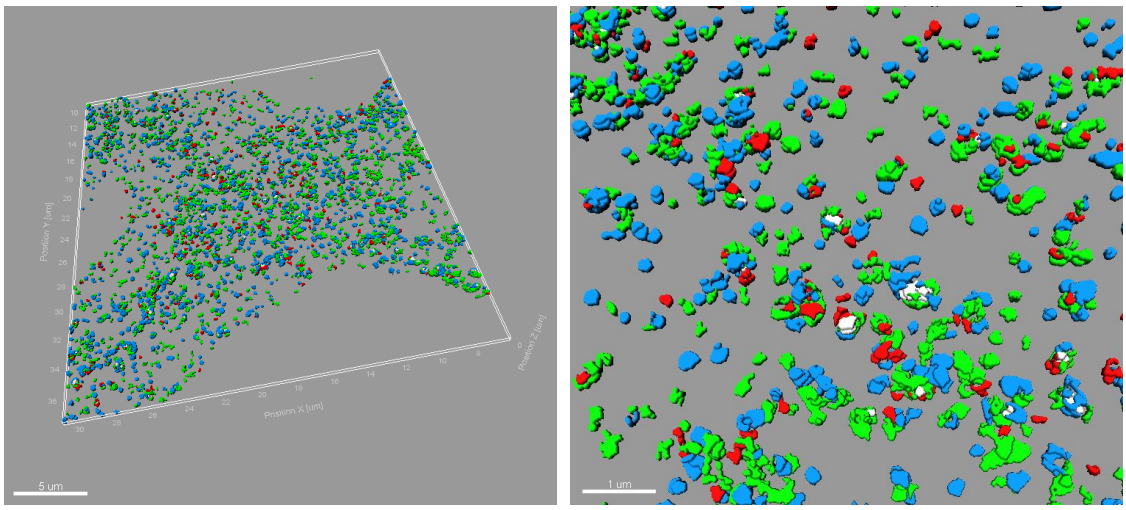

Figure 26. 3D Surfaces objects of free complexes and TRIOs binary channels

RESULTS

I. Novel *in situ* validation of the Plasticity Model

The aim of Results I is the evaluation of the interaction and assembly status of respiratory complexes in cultured cell lines. For this purpose, we have planned a double and parallel approach based on the use of the same immunostaining protocol by which on one hand, we have separated and identified the complexes by BNGE and on the other hand, we had applied the same set of primary antibodies for in situ immunostaining by super-resolution and confocal fluorescence microscopy (Table 11).

Table 11. Experimental design

Control Cells & Mutant cells	BNGE	Complex I subunits	NDUFB8	
			NDUFS3	
		Complex III subunits	Rieske	
			CORE1	
		Complex IV subunits	COI	
			COX5A	
	Co-immunostaining	Confocal	Mitochondrial localization	
			Subunits immunospecificity	
		STED	Mitochondrial localization	
			Subunits immunospecificity	
			Colocalization	
			Quantitative analysis of complex distribution and 3D reconstruction	

Each mitochondrial complex was labelled using two different subunits that are represented in Figure 27. By this experimental design we could obtain the first in situ demonstration of the plasticity model.

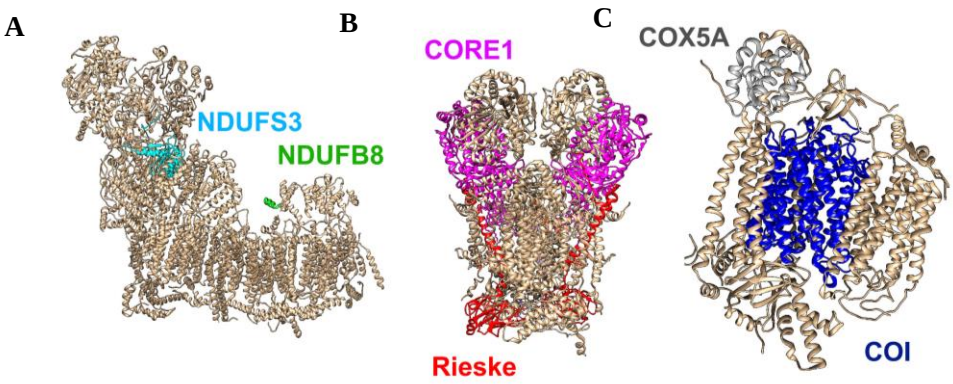

Figure 27. Assignment of the mitochondrial subunits. Transparent surface representation of mitochondrial complex I, complex III and complex IV [Source: Protein Data Base (PDB)] Each immunostained subunit is highlighted by pseudocolors **(A)** NDUFS3 and NDUFB8 subunits of CI in cyan and green, respectively. **(B)** The assigned subunits for complex III, CORE1 and Rieske in red and magenta, respectively. **(C)** CIV subunits COX5A and COI, in grey and blue, respectively.

The subunit selection was based on following criteria: 1) Commercial availability of primary antibodies; 2) Antibody combinations depending of the commercial availability of specificity secondary IgG and 3) antibodies positive for BNGE.

I.1 Identification of respiratory complexes and supercomplexes by BNGE

BNGE separate the respiratory complexes and supercomplexes and the immunodetection of individual subunits allow to discriminate between their assembled, superassembled or unassembled status. In this work, we used ρº cells as a negative control for assembled status. ρº cells lacks mtDNA, and therefore are unable to assembly complex I, III and IV. These cells are able to assemble complex II and a subcomplex of the ATPase. The second model was $CYTb^{M}$ cell line that harbor a missense mutation in the cytochrome b gene and therefore does not assembly CIII. The last model was $COX10^{KO}$ cell line, that doesn´t express COX10, a farnesyltransferase required for the maturation of the cytochromes a-a3. In absence of this enzyme, cytochrome c oxidase (CIV) assembly is impeded. Each mutant cell line was compared with the respective isogenic wild type cell line: ρ+, $CYTb^{Ctrl}$, $COX10^{Ctrl}$. Determination of the assembly status of the respiratory complexes in these cells was done in digitonin-permeabilized mitochondria separated by BNGE and probed with monoclonal antibodies for two subunits for each mitochondrial complex. Complex I (NDUFB8 and NDUFS3), Complex III (CORE1 and Rieske) and Complex IV (COI and COX5A).

I.1.1 Complex I subunits

BNGE probed for complex I subunits (NDUFB8 and NDUFS3) revealed the diversity on the assembly status of this complex, as a free complex or superassembled in the following SC combinations: I + III_2 in two differenciated bands and SC I + III_2 + IV, as observed in all control cell lines (Figure 28 A-C).

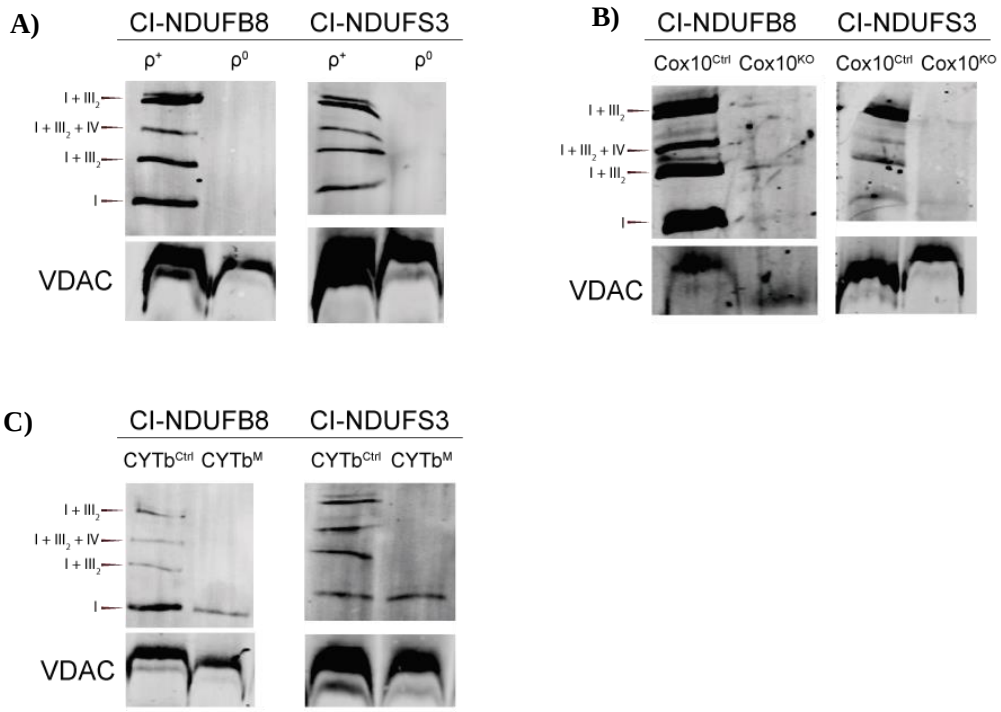

Figure 28. Analysis of the Assembly Status of the Different OXPHOS Complexes. Blue-Native gel electrophoresis of the mitochondrial OXPHOS complex I subunit NDUFB8 and NDUFS3 in the cell lines **(A)** ρ+ and ρ0 **(B)** $Cox10^{Ctrl}$ and $Cox10^{KO}$ **(C)** $CYTb^{Ctrl}$ and $CYTb^{M}$. VDAC is used as loading control in all cases.

As expected, ρº cells does not assembled any complex I. A small amount of free CI was detected in $CYTb^{M}$ cells while $COX10^{KO}$ cells kept a barely observed amount of free CI, and a complete loss of supercomplexes (Figure 28 A-C).

The massive loss of CI, in CIII and CIV deficient cells, is consequence of the elevation of the CoQred/CoQoxid rate and the induction of RET that signal CI for degradation (Guarás *et al.*, 2016).

I.1.2 Complex III subunits

BNGE & WB for complex III subunits (Rieske and CORE1) revealed the different assembly status of this complex, as a dimer III_2 or superassembled in the following SC combinations: III_2+IV; I + III_2 (two distinct bands) and SC I + III_2 + IV, as observed in all control cell lines (Figure 29 A-C).

ρ^o cells cannot assembly respiratory complexes, as revealed by BNGE probed with anti-Rieske or anti-CORE1 for complex III (Figure 29A), because of their inability to assemble CI, CIII and CIV. $COX10^{KO}$ cells, due to the lack of CIV, are incapable of forming CIII and CIV containing SCs but showed a conspicuous amount of CIII (Figure 29B). Equally, $CYTb^M$ cells were not able to assemble complex III_2 or supercomplexes. (Figure 29C).

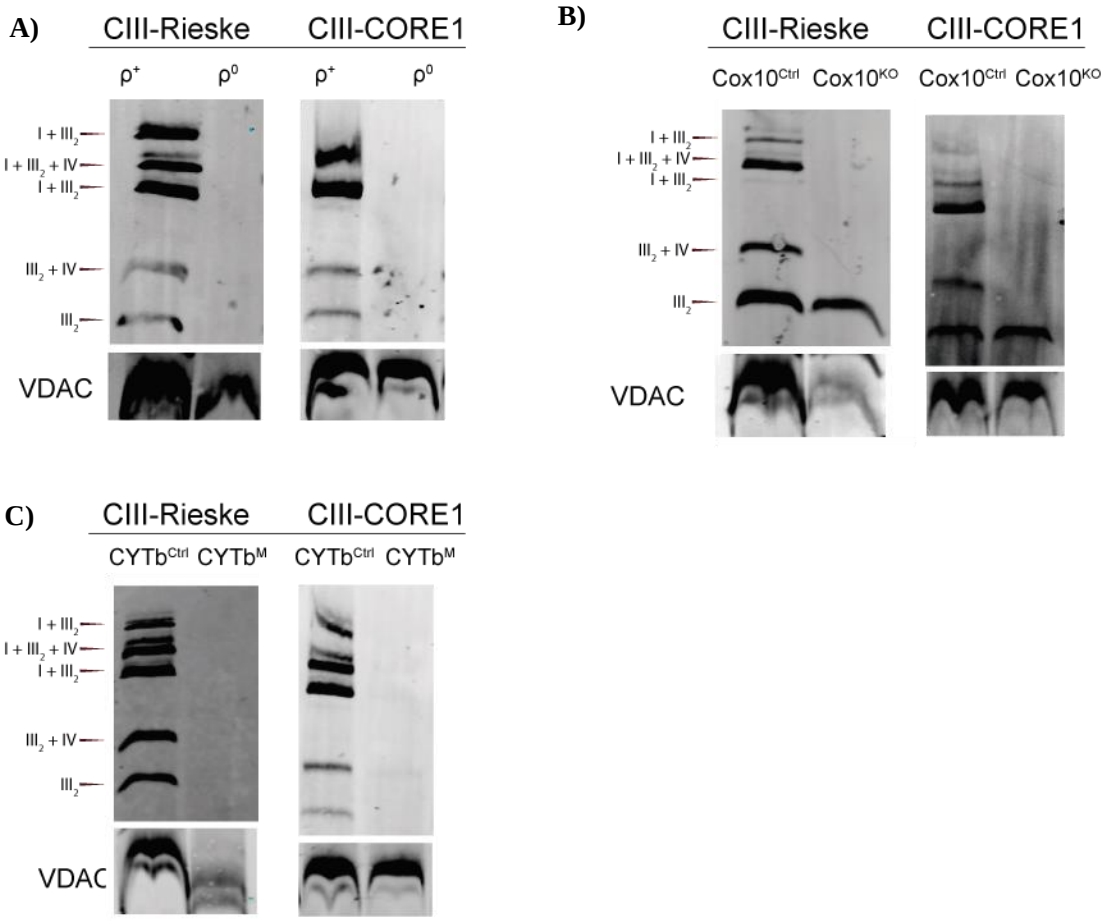

Figure 29. Analysis of the Assembly Status of the Different OXPHOS Complexes. Blue-Native gel electrophoresis of the mitochondrial OXPHOS complex III subunit Rieske and CORE1 in the cell lines (**A**) ρ+ and ρ0 (**B**) Cox10 ^{Ctrl} and Cox10 ^{KO} **(C)** $CYTb^{Ctrl}$ and $CYTb^M$. VDAC is used as loading control in all cases.

I.1.3 Complex IV subunits

BNGE for complex IV subunits (COI and COX5A) revealed the different assembly status of this complex, as a free complex or superassembled in the following SC combinations: III_2+IV and SC I + III_2 + IV, as observed in all control cell lines (Figure 30 A-C).

BNGE revealed that ρ^o cells did not assemble CIV (Figure 30A). The disruption of CIV biogenesis by the ablation of COX10 assembly factor revealed the lack of this complex in Cox10^{KO} cells (Figure 30B). In CYTb^M, the lack of CIII preclude the formation of supercomplexes (since they all contain CIII), showing only free CIV (Figure 30C).

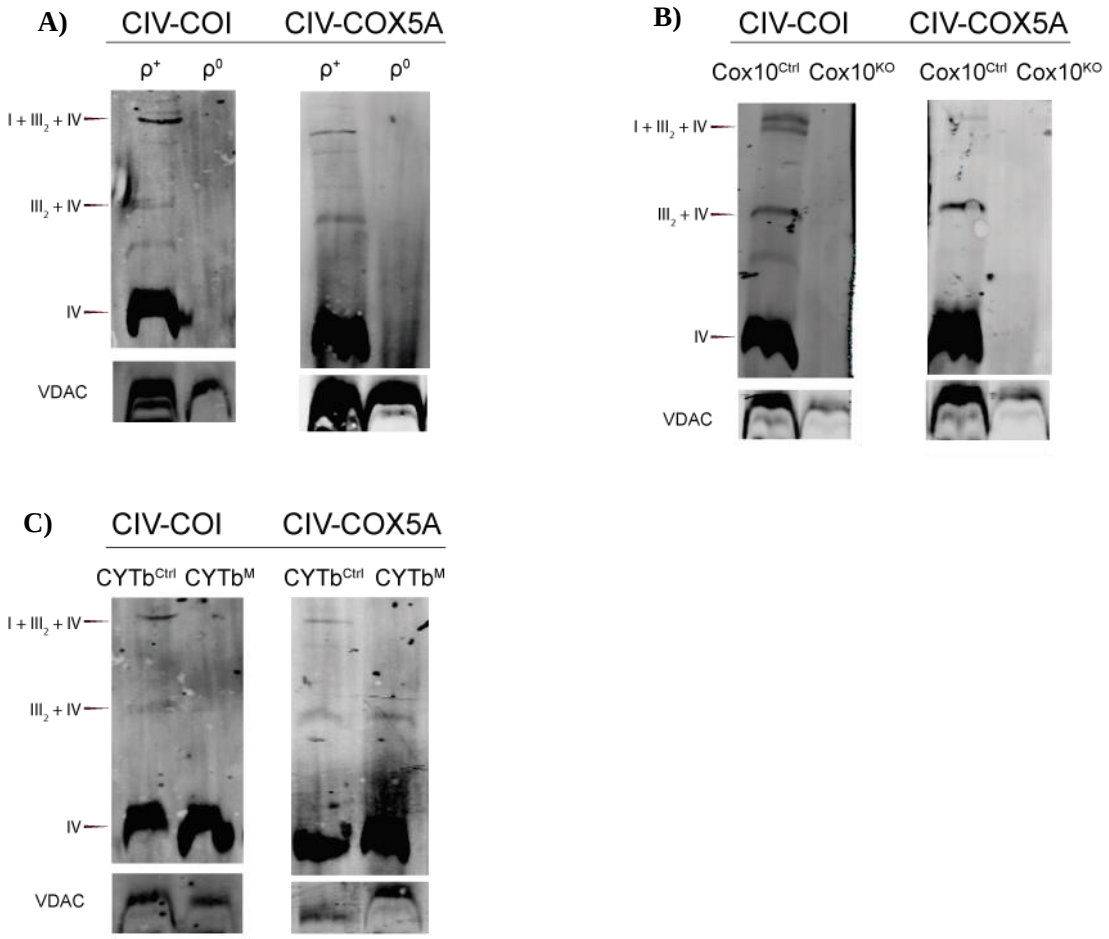

Figure 30. Analysis of the Assembly Status of the Different OXPHOS Complexes. Blue-Native gel electrophoresis of the mitochondrial OXPHOS complex IV subunit COI and COX5A in the cell lines (**A**) ρ$^+$ and ρ0 (**B**) Cox10 ^{Ctrl} and Cox10 ^{KO} **(C)** CYTb^{Ctrl} and CYTb^M. VDAC is used as loading control in all cases.

In summary, equal detection was obtained using different subunits for each mitochondrial complex. According to the recent literature, the BNGE analysis in the mutated cell lines, correctly reproduced the alterations in complex assembly as summarized in the in the following table:

Table 12. Blue Native Gel Electrophoresis observations table summary.

Cell	BNGE Observations					
	CI	CIII	CIV	CI + CIII	CIII + CIV	CI + CIII + CIV
$Cox10^{Ctrl}$	√	√	√	√	√	√
$Cox10^{KO}$	Low	—	—	—	—	—
$CYTb^{Ctrl}$	√	√	√	√	√	√
$CYTb^{M}$	√	—	√	—	—	—
$Rho0^{Ctrl}$	√	√	√	√	√	√
Rho0	—	—	—	—	—	—

I.2 Identification of respiratory complexes and supercomplexes by Imaging.

With the aim of conducting the parallel detection of the complexes by biochemical batch analysis and by *in situ* imaging analysis, we next evaluated the conditions for STED and confocal imaging and the achievable spatial resolution. In fact, both experimental approaches have complementary advantages and disadvantages. The most challenging task was the selection of secondary antibodies that were suitable labels for STED depletion in 3D.

First, we explored the increase in resolution of STED images in x,y and z planes using 23 nm GATTAQuant nano labelled beads with Alexa 568 (Figure 31A), Alexa 532 (Figure 31B) and Ab488Star (Figure 31C).

Spatial Resolution was measured as Full-Width at Half Max(FWHM) of the Gaussian fit for each PSF (Point Spread Function).

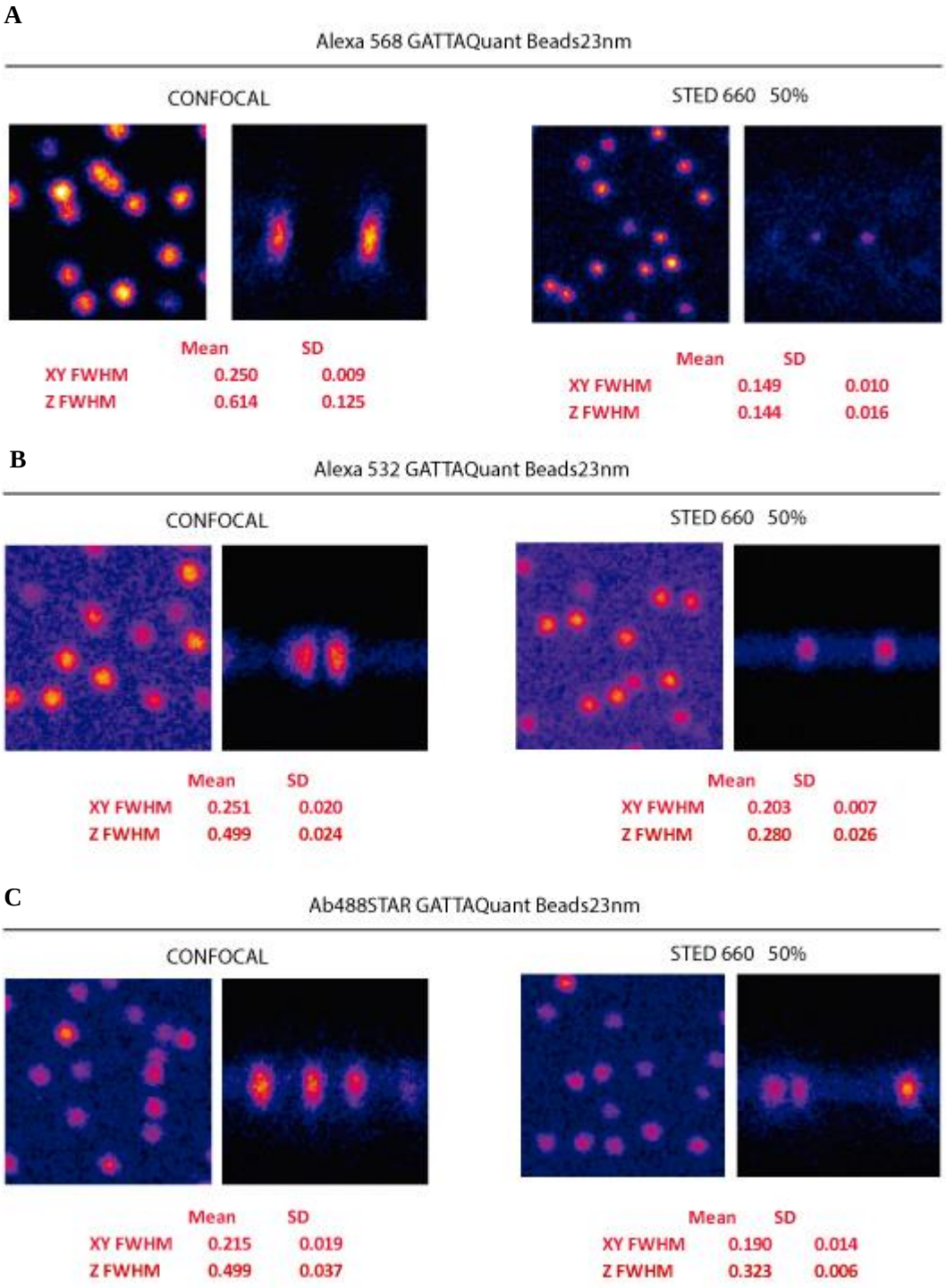

Figure 31. Determination of the STED microscope's resolution. Super resolution image acquired on a Leica TCS SP8 STED imaging system. 660 STED depletion laser power is indicated in all the images. Left images were acquired in the lateral direction (XY) and right images were acquired in the axial direction. The full-width at half maximum (FWHM) in our images showed a resolution for the x,y plane of 100-200 nm and in Z of 300nm. Images are presented as: **(A)** Alexa 568 GATTAQuant Beads 23nm. **(B)** Alexa 532 GATTAQuant Beads 23nm **(C)** Ab488STAR GATTAQuant Beads 23nm.

I.3 *In situ* cellular localization of individual subunits

The endogenous content and cellular distribution of each subunit was investigated by co-immunostaining with the mitochondrial outer membrane marker TOM20. Combined confocal and STED imaging were run in parallel with SDS gel electrophoresis to assess the total subunit content in the cell samples.

I.3.1 Cox10^{Ctrl} and Cox10^{KO}

Complex I subunits. When we carried out the analysis in our Cox10^{Ctrl} cells, we observed a homogeneous distribution in the confocal images for both complex I subunits along the mitochondrial marker TOM20, being NDUFB8 subunit more predominantly expressed than NDUFS3.

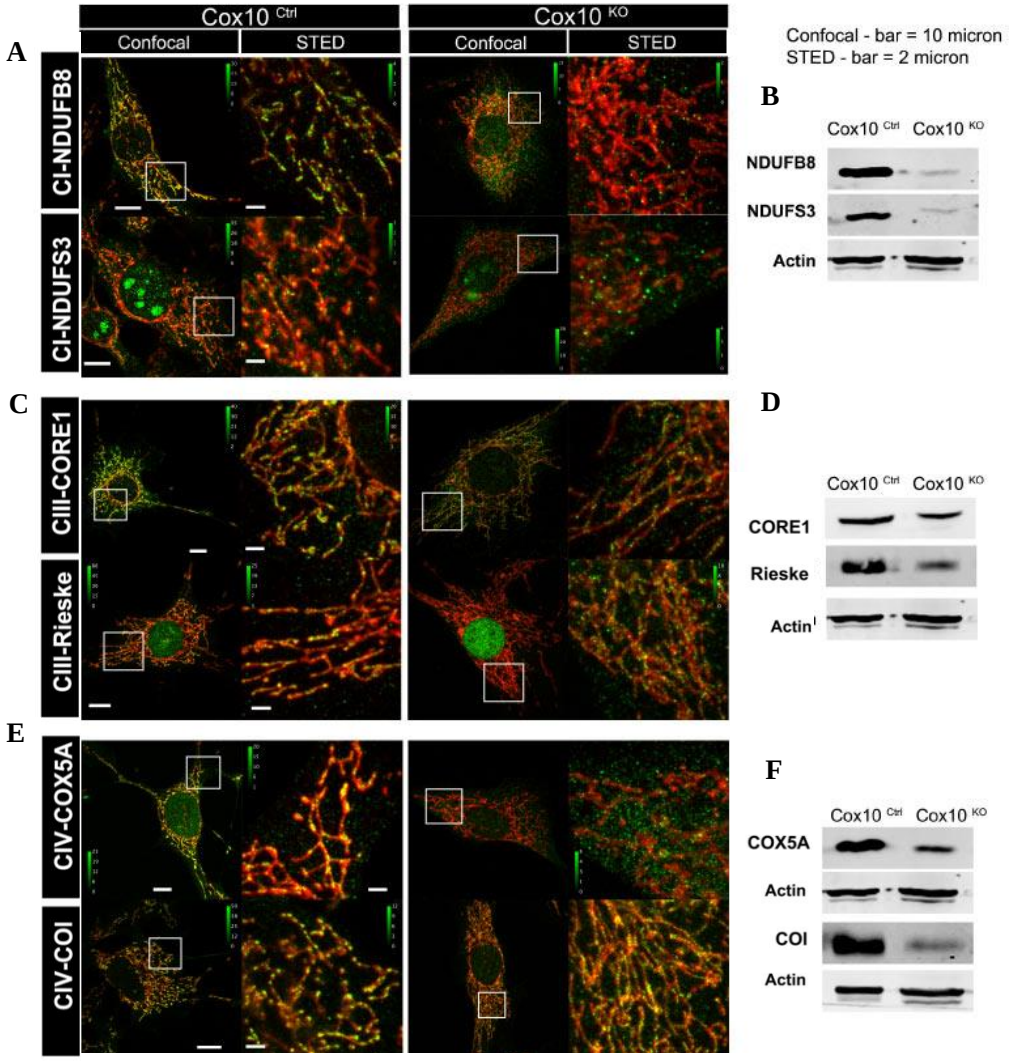

Figure 32. Single mitochondrial subunits localization in Cox10 cells. (A,C,E) Immunofluorescence of mitochondrial subunits in green and mitochondria outer membrane marker TOM20 in red. Left images are confocal scans, confocal scale bar: 10 µm. . The 7x zoomed composite images of confocal TOM20 and STED-subunits are shown in on the right. STED scale bar: 2µm **(B,D,F)** Western Blot analysis for both cell lines against each subunit of CI, CIII and CIV. Actin was used as loading control.

We should notice that the immunostaining applied for NDUFS3 subunit, also showed high disorganized fluorescence in the nuclei. STED super resolution analysis of region of interest (ROI) randomly chosen on the mitochondrial network indicate sparse distribution of the NDUFS3 subunit in the mitochondrial membrane. In contrast, the NDUFB8 subunit appeared to accumulate heavily in the mitochondrial membrane and also showed punctuate structure (Figure 32A).

As mentioned before, Cox10^{KO} cell line has a disruption of CIV biogenesis by the ablation of the COX10 assembly factor, the lack in CIV compromises the stability of CI. Therefore, the results of these alterations are evident in both confocal and STED analysis. In particular, STED images clearly demonstrated the complete delocalization along mitochondria of both subunits (Figure 32A).

These observations were confirmed in total protein content by SDS gel electrophoresis, where NDUFB8 was more abundant than NDUFS3 in control cells, and lower amount of both subunits was found in the mutant cells (Figure 32B).

Complex III subunits. In control cells, confocal images showed homogeneous distribution of both subunits along the mitochondria. However, anti-Rieske also reveals an intense signal in the nucleus. Using Rieske^{KO} cell line, we could confirm that the mitochondrial signal corresponds to true Rieske immunodetection, while the nuclear signal is spurious (Figure 33). The areas analyzed in STED, confirmed a specific mitochondrial localization for both subunits in these cells. On the other hand, Cox10 ^{KO} cells confocal images only present specific mitochondrial distribution when using CORE1 subunit, since this distribution was almost negligible when Rieske was labelled. However, STED images allowed us to distinguish the mitochondrial localization of these subunits in Cox10 ^{KO} cells. (Figure 32C).

The confocal- STED analysis was in good agreement with the total protein content for complex III subunits (Figure 32D).

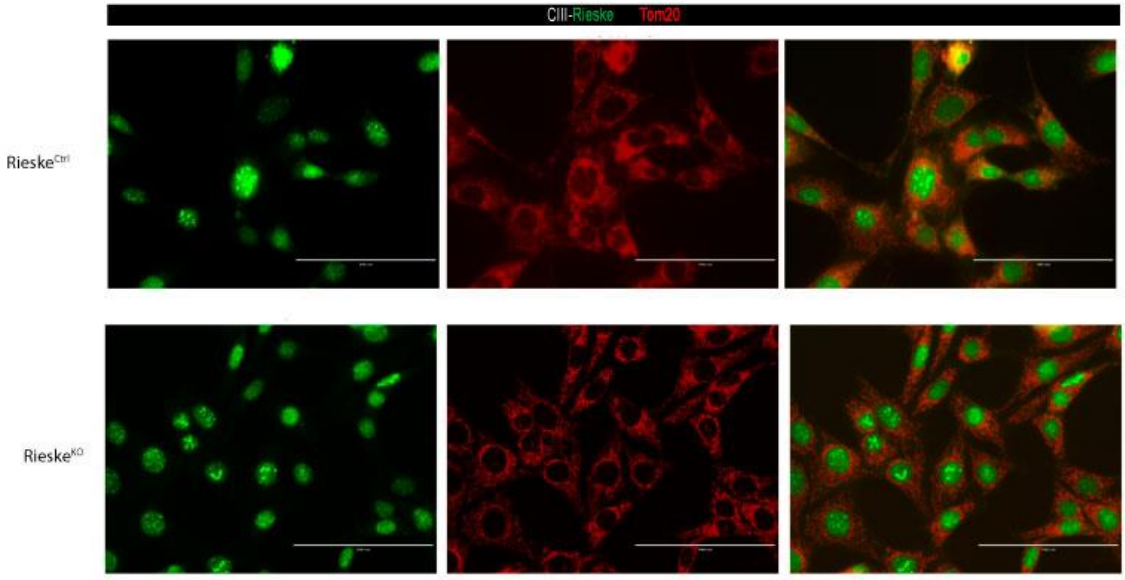

Figure 33. Rieske Immunodetection. We confirmed the nuclear staining of Rieske subunit in cells Rieske^{KO} and its isogenic control Rieske$^{Ctrl.}$ The immunostaining was done against Rieske and TOM20 for both cell lines. Images were acquired in Carlos Moraes Lab in a Fluorescent microscope. Scale bar: 100 µm.

Complex IV subunits. When studying complex IV subunits, Cox10^{Ctrl} cells showed specific mitochondrial localization in both confocal or STED images. However, in Cox10 ^{KO} cells, which are unable to assemble CIV, mitochondrial localization for these complex IV subunits was barely detected in confocal images, even though a preserved dynamic network for mitochondria was observed. The STED ROI analysis confirmed the delocalization of the nuclear encoded COX5A subunit. Conversely the mtDNA encoded Co-I subunit, presented an organized pattern along the mitochondria network in spite of the fact that it is not assembled (Figure 32E).

SDS determination confirmed that the amount of both complex IV subunits was reduced in Cox10^{KO} cells (Figure 32F).

I.3.2 CYTb^{Ctrl} and CYTb^{M}

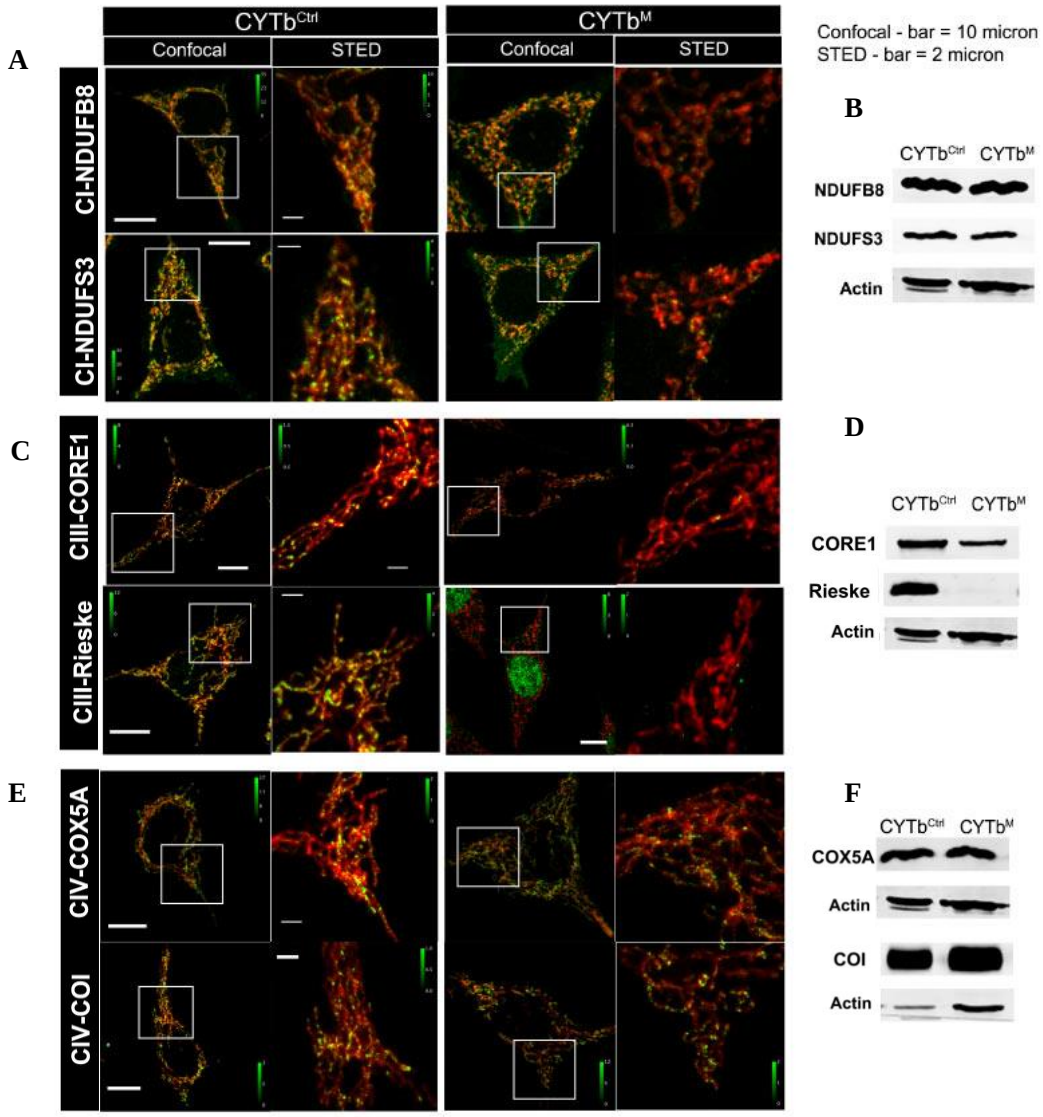

Figure 34. Single mitochondrial subunits localization in CYTb cells (A,C,E) Immunofluorescence of mitochondrial subunits in green and mitochondria outer membrane marker TOM20 in red. Left images are confocal scans, confocal scale bar: 10 µm. . The 7x zoomed composite images of confocal TOM20 and STED-subunits are shown in on the right. STED scale bar: 2µm **(B,D,F)** Western Blot analysis for both cell lines against each subunit of CI, CIII and CIV. Actin was used as loading control.

Complex I subunits. Confocal images in $CYTb^{Ctrl}$ cells, indicated a homogeneous distribution for both complex I subunits along the mitochondrial membrane marked by TOM20. STED-ROI analysis confirmed a homogenous staining for both subunits. $CYTb^{M}$ cells do not assemble CIII, therefore their CI is unstable. Confocal images in these $CYTb^{M}$ cells, did allowed to show any difference in distribution of these subunits compared with the control cells. However, STED ROIs, showed that these mitochondrial subunits had barely no distribution along the mitocondria (Figure 34A).

SDS gel electrophoresis assessed the total subunit content in the cell samples, being similar for both subunits, confirming that the major difference was due to mislocalization.

Complex III subunits. The endogenous complex III subunits in $CYTb^{Ctrl}$ cells showed a homogeneous distribution along the mitochondria in confocal scans and a punctuate staining in STED-ROIs scans. In contrast, we detected a relevant decrease of expression of both subunits in the $CYTb^{M}$, lacking mitochondrial localization (Figure 34C). Again, we observed the nuclear spurious staining with anti-Rieske antibody. However, the total protein content still indicated the presence of a low yet detectable CORE1 subunit in $CYTb^{M}$ cells. The partial disagreement between the two results might be due to the detectability limit of fluorescence immunostaining in STED images (Figure 34D).

Complex IV subunits. In $CYTb^{Ctrl}$ cells, we can highlight the mitochondrial localization of CIV subunits, COI and COX5A, in both confocal and STED images. Similarly, $CYTb^{M}$ cells showed a discrete localization of these mitochondrial subunits, both in confocal and STED images (Figure 34E).

These observations were confirmed by SDS results, where no differences were found among this cell lines (Figure 34F).

I.3.3 ρ^+ and ρ^0

Complex I subunits. Confocal images in ρ^+ cells showed a sparse distribution of both complex I subunits along the mitochondrial membrane marked by TOM20. STED ROIs showed this punctuate staining for both subunits and no signals out of the mitochondrial membrane. ρ^0 cells lacking mtDNA, are unable to assemble CI. Nevertheless, the CI subunits NDUFB8 and NDUFS3 might be produced by these cells, delocalized out of the mitochondria and quickly degraded. As a result of this alteration, the degraded subunits might be exposed to antibodies better than the integral subunits assembled in CI in ρ^+ cells. This would yield an intense and nonspecific immunostaining, while the fragments would escape from SDS detection, as revealed in the no mitochondria localization when STED images were studied (Figure 35A).

SDS gel electrophoresis barely detect NDUFB8 subunit in ρ^0 cells (only upon over exposing it) while NDUFS3 was albeit decreased, since is more stable when unassembled (Figure 35B).

Complex III subunits. Confocal images in ρ^+ cells showed a homogeneous distribution along the mitochondria. STED ROI analysis, confirmed a specific mitochondrial localization for both subunits in these cells, being greater the localization for Rieske subunit. These subunits had no localization and expression in ρ^0 mitochondria, for both confocal and STED images (Figure 35C).

SDS confirmed the reduction of these subunits in ρ^0 cells, being greater when using Rieske subunits (Figure 35D).

Complex IV subunits. Confocal images in ρ^+ cells showed specific mitochondrial localization in both confocal or STED images. However, in ρ^0 cells, which are unable to assemble CIV, low distribution for these complex IV subunits was found in confocal images for COX5A. The STED selections against this subunit confirmed the lack in organization. Co I subunit is codified by the mtDNA that is absent in ρ^0 cells, as expected no COI was observed by confocal or STED analysis (Figure 35E).

Total protein content analysis confirmed the reduction of COI subunit in $Cox10^{KO}$ cells (Figure 35F).

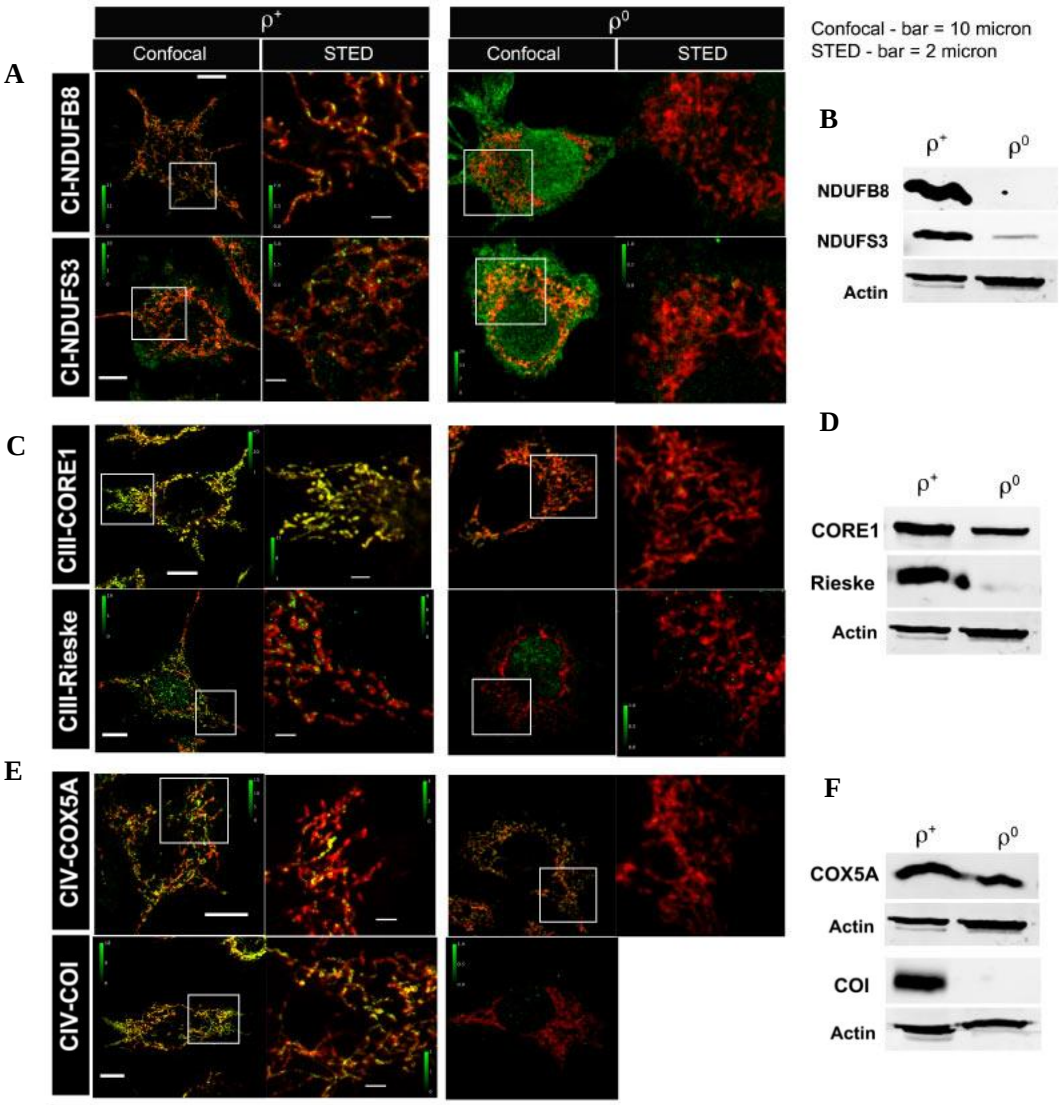

Figure 35. Single mitochondrial subunits localization in ρ cells (A,C,E). Immunofluorescence of mitochondrial subunits in green and mitochondria outer membrane marker TOM20 in red. Left images are confocal scans, confocal scale bar: 10 µm. . The 7x zoomed composite images of confocal TOM20 and STED-subunits are shown in on the right. STED scale bar: 2µm **(B,D,F)** Western Blot analysis for both cell lines against each subunit of CI, CIII and CIV. Actin was used as loading control.

I.4 *In situ* cellular localization of CI and CIII pair subunits

To determine the co-occurrence of CI and CIII within the resolution achieved by STED, we co-labelled our cells against two subunits for complex I (NDUFB8 and NDUFS3) and the Rieske subunit for complex III. All the images are processed with the color code described in Figure 27.

I.4.1 Cox10^{Ctrl} and Cox10^{KO}

In Cox10^{Ctrl} cells both NDUFB8 and NDUFS3 subunits presented similar overall spatial distribution and closeness expression in a number of replicated samples analyzed in STED (Figure 36A).

The result obtained in Figure36B, pointed out an increased co-occurrence when NDUFS3/Rieske pair was used.

The result of individual subunit localization (Results I.3.1) indicated low expression of NDUFB8 and NDUFS3 subunits in Cox10^{KO} mitochondria. This sparse expression was confirmed in confocal experiments by double immunostaining. Moreover, STED-ROIs analysis detected null co-localization between these subunits (Figure 36A-rightpanel).

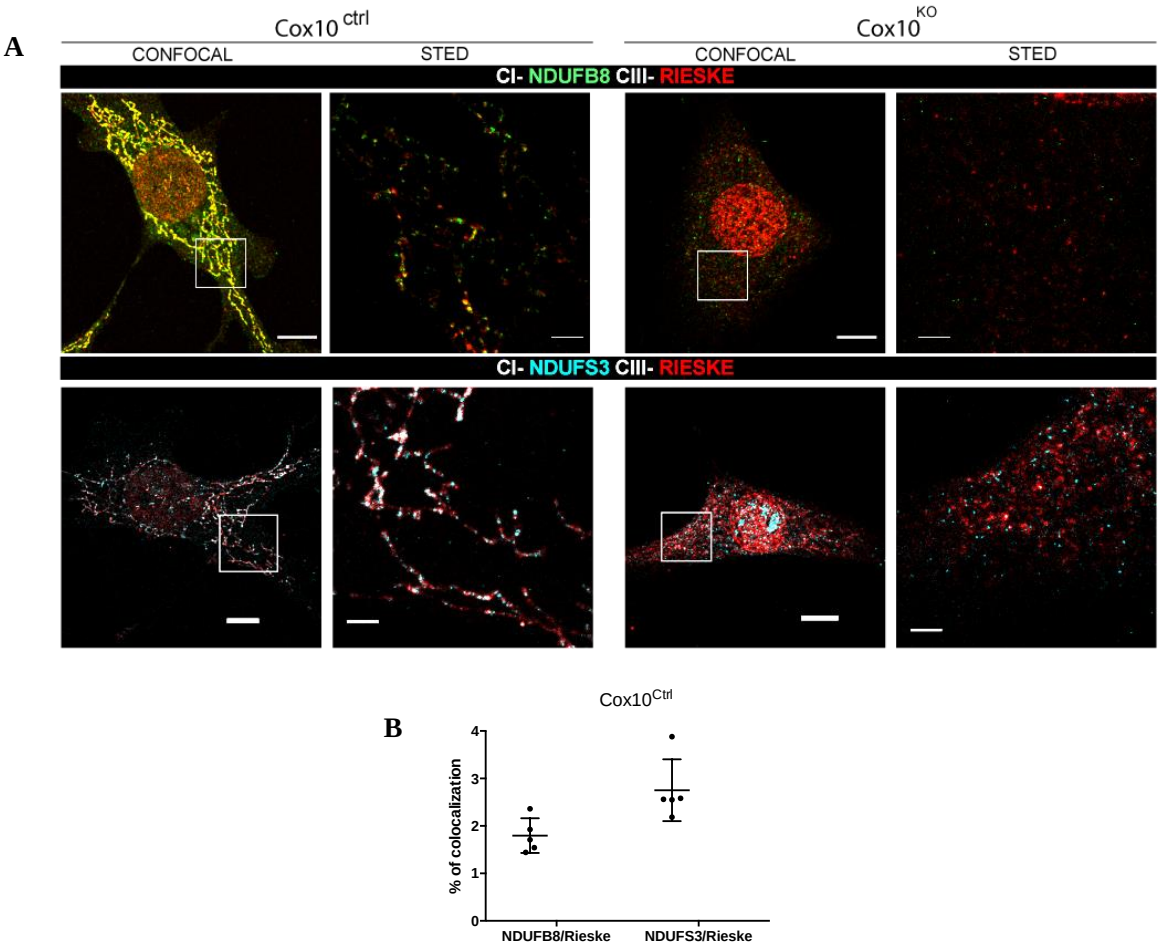

Figure 36. Immunostaining of endogenous CI (NDUFB8 and NDUFS3) and CIII-containing subunits (Rieske). Confocal and STED-ROI images of **(A)** Cox10 ^{Ctrl} and Cox10^{KO} cells labelled endogenously with anti-Rieske (red), anti-NDUFB8(green) and anti-NDUFS3 (Cyan). Confocal scale bars: 10 µm. STED scale bars: 2 µm. **(B)** % of colocalization for CI and CIII in Cox10^{Ctrl} cells. 5 STED-ROI on replicated cells.

I.4.2 CYTb^{Ctrl} and CYTb^{M}

Visual inspection of confocal images suggested extensive proximity of CI and CIII independently on the CI subunits used as immunostaining marker. When selected areas were imaged in super resolution we could detect pairs of both complexes and isolated CI and CIII signals (Figure 37A).

In CYTb^{Ctrl} cell, co-localization was confirmed analyzing the % of colocalization on replicated STED-ROIs, as shown in Figure 37B.

The previous results from single color experiments obtained on CYTb^{M} cells, indicated that the expression of Rieske in this cell line was below the detection limit in both SDS and STED analysis. This observation was fully confirmed in the double immunostaining of CI and CIII experiments. In fact, the low expression of complex III subunit was evident in the images. (Figure 37A). STED-ROIs analysis was not performed due to the very low fluorescence signal found with these labelled subunits and the complete lack of co-localization visible in the confocal tests.

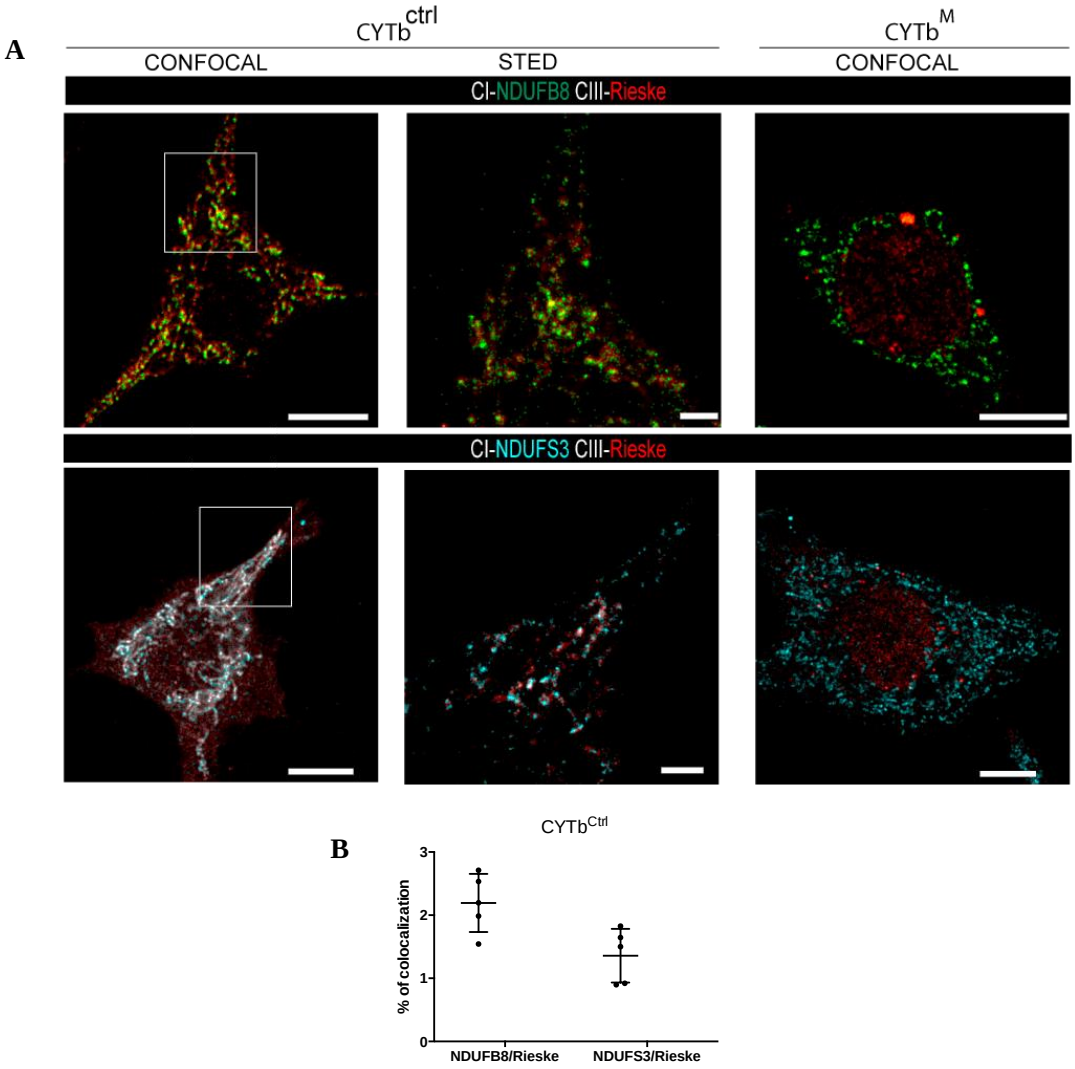

Figure 37. Immunostaining of endogenous CI (NDUFB8 and NDUFS3) and CIII-containing subunits (Rieske). Confocal and STED-ROI images of **(A)** CYTb ^{Ctrl} and CYTb^{M} cells labelled endogenously with anti-Rieske (red), anti-NDUFB8(green) and anti-NDUFS3 (Cyan). Confocal scale bars: 10 µm. STED scale bars: 2 µm. **(B)** % of colocalization for CI and CIII in CYTb^{Ctrl} cells. 5 STED-ROI on replicated cells.

I.4.3 ρ^+ and ρ^0

Confocal images showed extensive proximity of CI and CIII independently on the CI subunits used as immunostaining marker. When ROIs were imaged in super resolution we could confirm a high degree of close proximity in the control cells, in addition to verify the presence of isolated CI and CIII signals (Figure 38A).

The % of co-localization of CI and CIII in replicated STED-ROIs shown in Figure 38B supported the conclusion that in ρ^+ cell, both NDUFB8 and NDUFS3 subunits are indicative of similar spatial distribution of complex I.

The result of individual subunit localization (Results I.3.3) indicated that the expression of NDUFB8, NDUFS3 and Rieske in ρ^0 cell line was not specific for the mitochondrial membrane. This observation was fully confirmed in the double immunostaining of CI and CIII. In fact, the low and sparse residual and delocalized expression of the three subunits was evident already in confocal images. Therefore, STED analysis was not required.

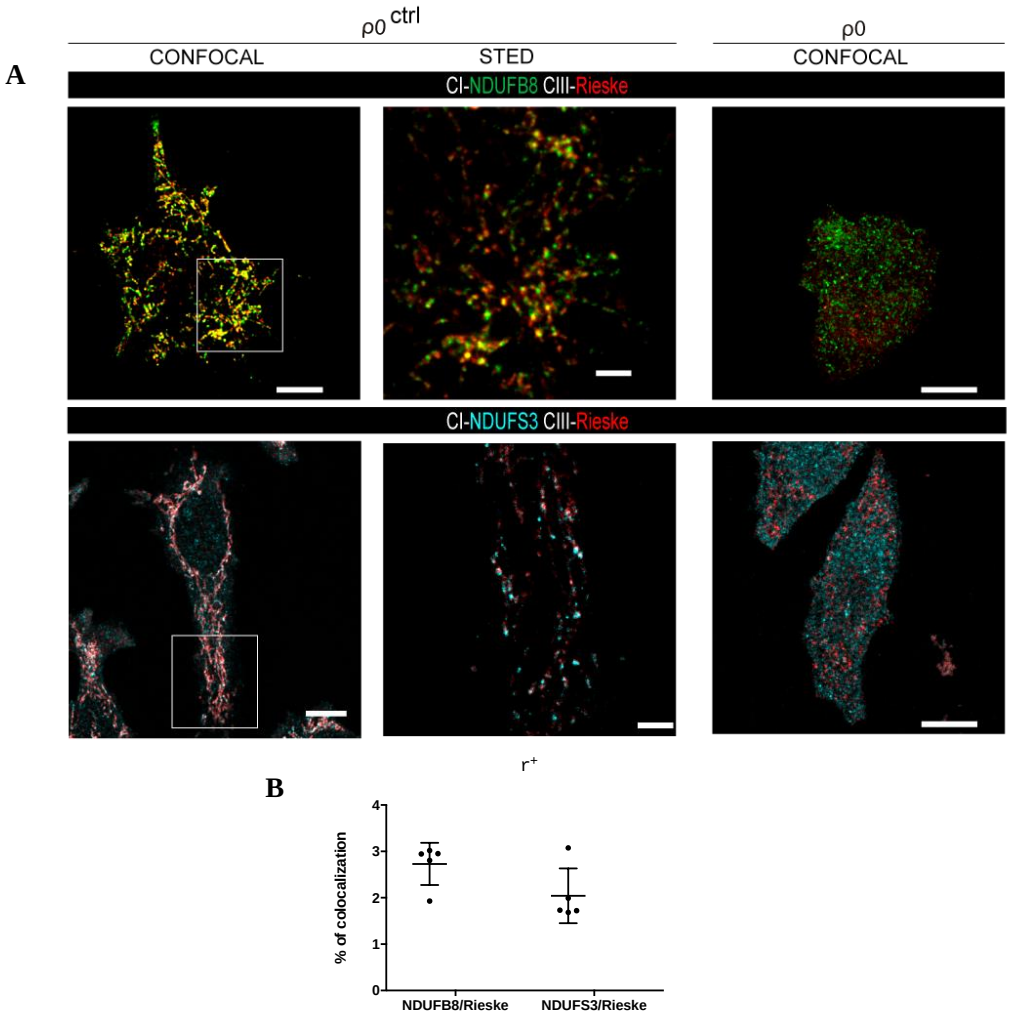

Figure 38. Immunostaining of endogenous CI (NDUFB8 and NDUFS3) and CIII-containing subunits (Rieske). Confocal and STED-ROI images of **(A)** ρ^+ and ρ^0 cells labeled endogenously with anti-Rieske (red), anti-NDUFB8(green) and anti-NDUFS3 (Cyan). Confocal scale bars: 10 µm. STED scale bars: 2 µm. **(B)** % of colocalization for CI and CIII in ρ^+ cells. 5 STED-ROI on replicated cells.

To determine the close proximity of CIII and CIV within the resolution achieved, we co-labelled our cells against two subunits for complex III (CORE1 and Rieske) and two subunits of complex IV (COX5A and COI). All the images are processed with the color code described in Figure 27.

I.5.1 Cox10^{Ctrl} and Cox10 ^{KO}

We observed a high degree of co-occurrence of complex III and complex IV in Cox10^{Ctrl} cells, which was not dependent on the subunits used for immunostaining. When ROIs were studied in STED, we could confirm extensive and precise mitochondrial co-localization of the complexes (Figure 39A).

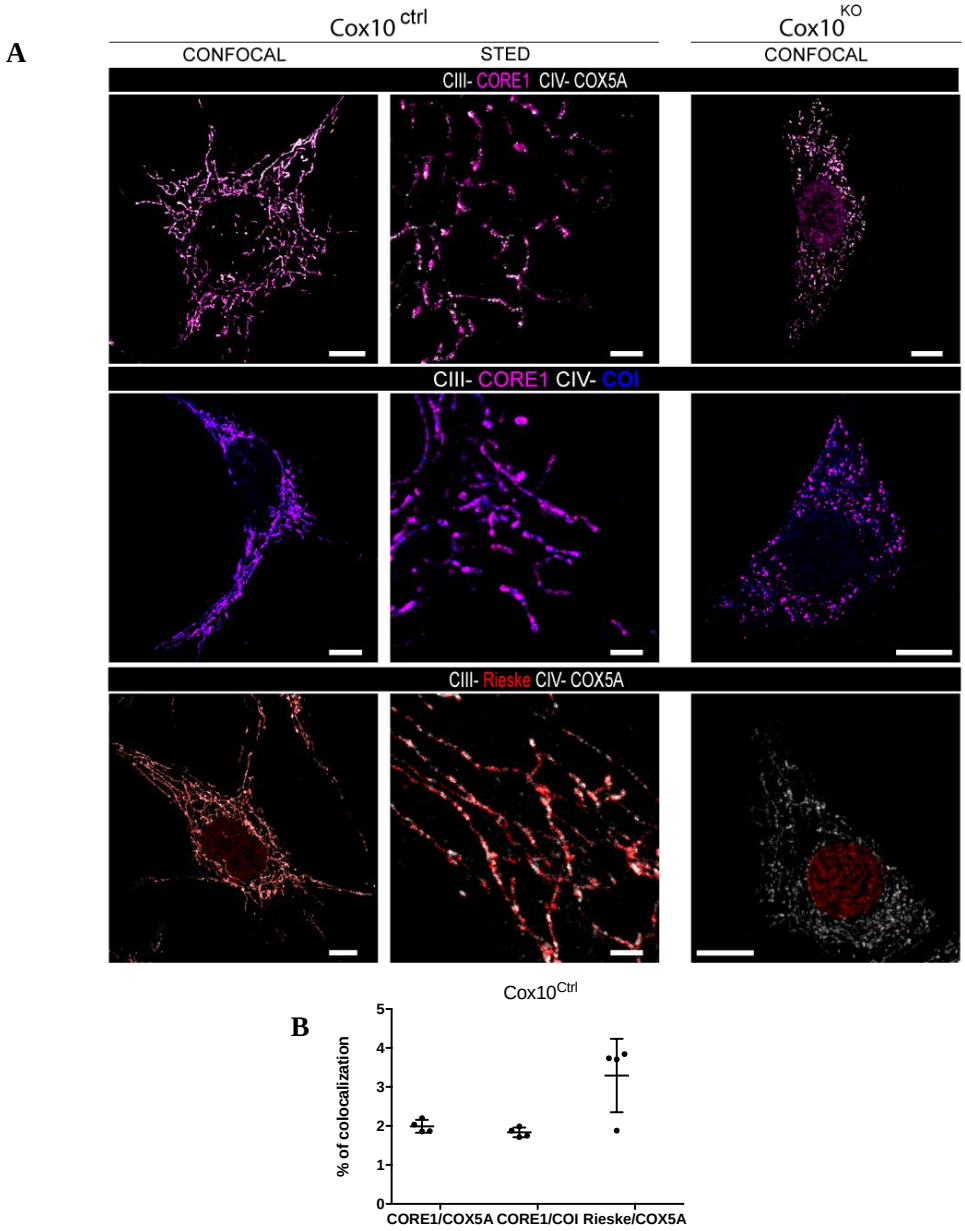

Figure 39. Immunostaining of endogenous CIII (Rieske and CORE1) and CIV-containing subunits (COX5A and COI). Confocal and STED-ROI images of **(A)** Cox10^{Ctrl} and Cox10^{Ko} cells labeled endogenously with anti-Rieske (red), anti-CORE1 (pink), anti-COX5A (grey) and anti-COI (blue). Confocal scale bars: 10 µm. STED scale bars: 2 µm. **(B)** % of colocalization for CIII and CIV in Cox10^{Ctrl} cells. 4 STED-ROI on replicated cells.

The co-localization analysis performed in Cox10^{Ctrl} cells, showed a consistent distribution of these subunits, supporting the conclusions obtained from the immunostaining. Figure 39B.

We observed delocalized distribution in CIII and CIV subunits without overlaps between signals in Cox10^{KO} confocal images. Therefore, there was no reason to apply STED analysis (Figure 39A).

I.5.2 CYTb^{Ctrl} and CYTb^{M}

A notable level of co-occurrence between complex III and complex IV in CYTb^{Ctrl} cells was observed, non-dependent on the immunomarker used. When selected areas were studied in STED, proximity in these complexes was fully confirmed (Figure 40A).

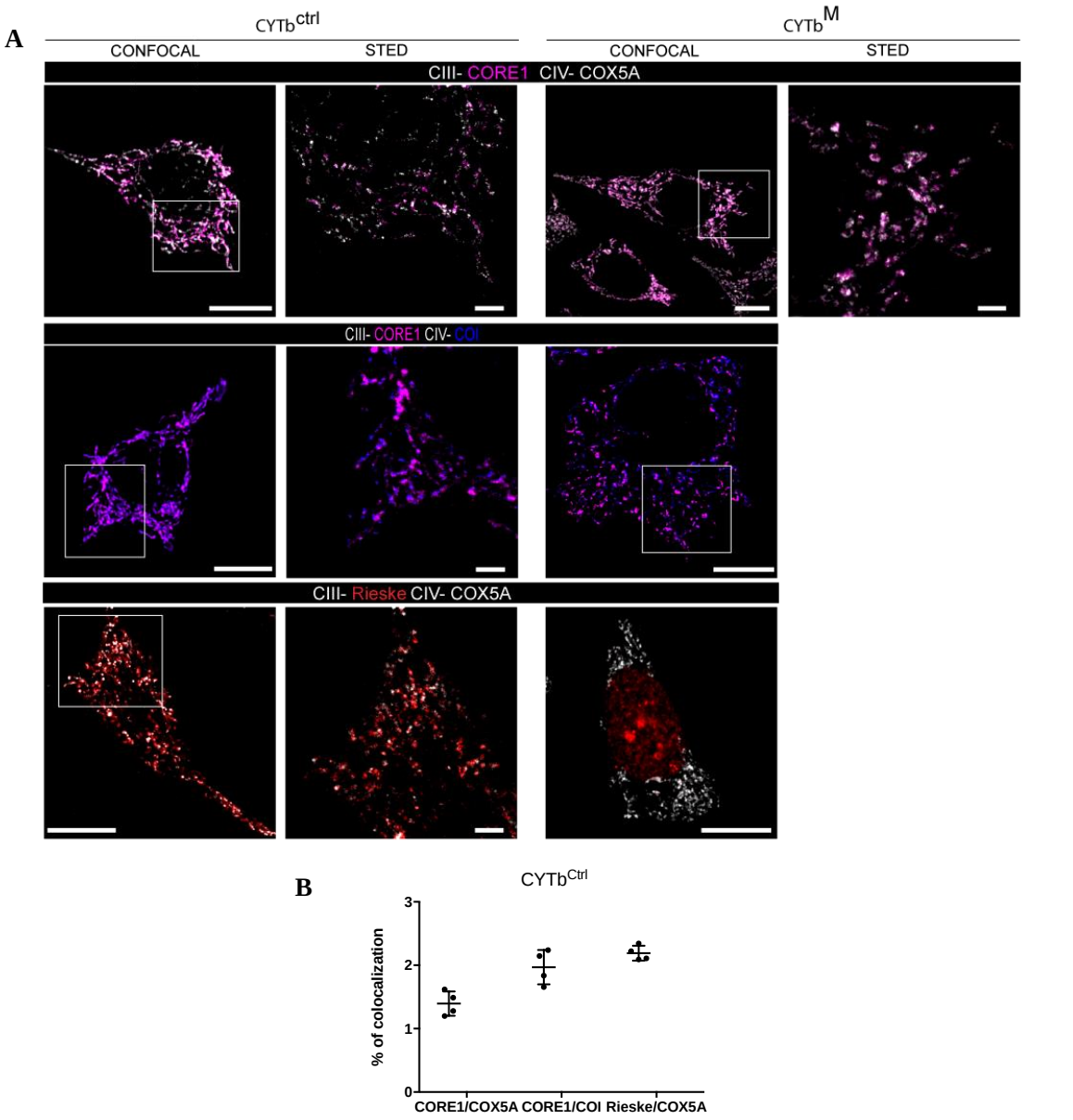

Figure 40. Immunostaining of endogenous CIII (Rieske and CORE1) and CIV-containing subunits (COX5A and COI). Confocal and STED-ROI images of **(A)** CYTb^{Ctrl} and CYTb^{M} cells labeled endogenously with anti-Rieske (red), anti-CORE1 (pink), anti-COX5A (grey) and anti-COI (blue). Confocal scale bars: 10 µm. STED scale bars: 2 µm. **(B)** % of colocalization for CIII and CIV in CYTb^{Ctrl} cells. 5 STED-ROI on replicated cells.

The overall colocalization in replicated STED images shown in Figure 40B supported the conclusion that in $CYTb^{Ctrl}$ cell, complex III subunits had similar spatial distribution, non-dependent on the combination used.

The result of single subunit localization (Results I.3.2) indicated that the expression of CORE1, COX5A and Co-I in $CYTb^{M}$ cell line was mitochondria specific. However, the expression of Rieske in this cell line was negligible and not specifically localized in the mitochondrial membrane. All these observations were fully confirmed by double immunostaining of CIII and CIV.

$CYTb^{M}$ cells are not able to assemble SC III+IV, but in the BNGE result labeled with COX5A an unspecific band was observed migration close to position of SC III_2+IV (Figure 30C), band that was not observed in all other BNGE probed against different antibodies. This result was confirmed in the confocal and STED images when using these subunits as markers.

The confocal analysis of $CYTb^{M}$ cells for subunits CORE1 and Co-I indicated a distribution pattern of proximity between CIII and CIV. The increase in resolution in the STED area, elucidated that this proximity was not confirmed. The low and sparse residual expression of Rieske was evident in the confocal images. Therefore, there was no reason to improve the resolution by STED imaging.

I.5.3 ρ^+ and ρ^0

We analyzed the distribution pattern of OXPHOS CIII and CIV, finding a preservation in the mitochondrial structure and proximity of the complexes in ρ^+ cells. This observation was independent of the particular OXPHOS complex combination and reconfirmed when STED-ROIs were selected for further analysis (Figure 41A).

A quantitative analysis in the replicated STED experiments, determined the level of proximity between the complexes, confirming the immunofluorescence observations. Figure 41B.

We analyzed the proximity behavior of these complexes in ρ^0 cells, finding different distribution states. Confocal experiments seemed to indicate dense and extensive overlap between CORE1 and COX5A. However, this micro-organization of the proteins was not confirmed at the nanoscale level.

Single subunit localization experiments (Results I.3.3) indicated that the ρ^0 cell line did not express Rieske and Co-I proteins. This observation was confirmed in the double immunostaining of CIII and CIV subunits from confocal images, making the STED analysis unnecessary.

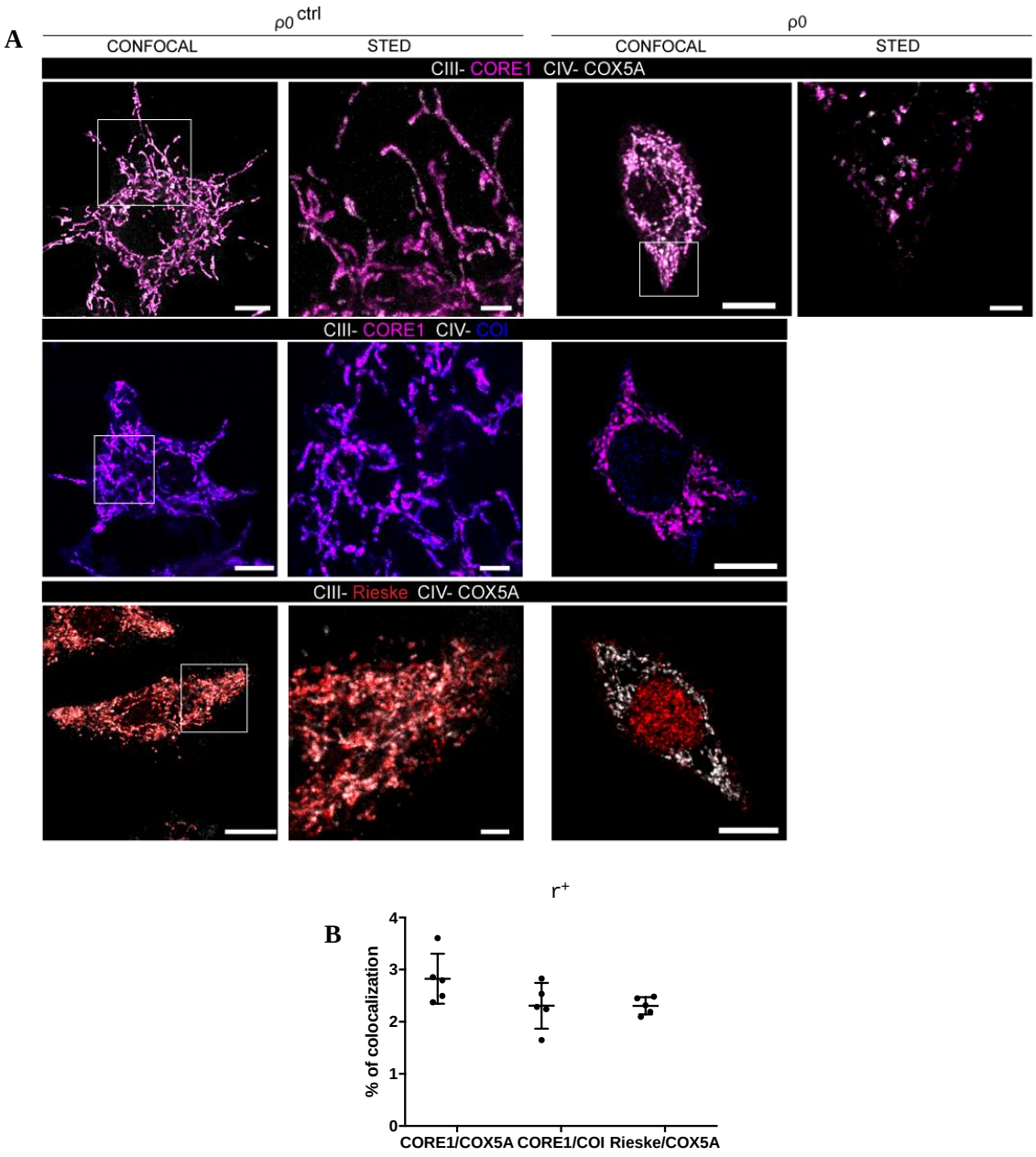

Figure 41. Immunostaining of endogenous CIII (Rieske and CORE1) and CIV-containing subunits (COX5A and COI). Confocal and STED-ROI images of **(A)** ρ^+ and ρ^0 cells labeled endogenously with anti-Rieske (red), anti-CORE1 (pink), anti-COX5A (grey) and anti-COI (blue). Confocal scale bars: 10 µm. STED scale bars: 2 µm. . **(B)** % of colocalization for CIII and CIV in ρ^+ cells. 5 STED-ROI on replicated cells.

I.6 *In situ* cellular localization of CI and CIV pair subunits

To explore the proximity of CI and CIV within the resolution achieved, we co-labelled our cells against two subunits for complex I (NDUFB8 and NDUFS3) and two subunits for complex IV (COX5A and COI). All the images are processed with the color code described in Figure 27.

I.6.1 $Cox10^{Ctrl}$ and $Cox10^{KO}$

Confocal images of $Cox10^{Ctrl}$ cells show discrete proximity of CI and CV independently on the mitochondrial subunits used as immunostaining marker. When ROIs were imaged in super resolution we could confirm co-occurrence in the control cells in addition to verify the presence of isolated CI and CIV signals.

Colocalization analysis of CI and CIV in replicated STED images shown in Figure 42B, supported the conclusion that $Cox10^{Ctrl}$ cell had similar spatial distribution for all the pair combinations, with the exception of NDUFS3/COX5A pair, result that is coherent with the immunofluorescence example shown in Figure 42A.

Individual subunit localization analysis (Results I.3.1) indicated that the expression of NDUFB8, NDUFS3 in the mutant cell line was negligible, and complex IV subunits were not specifically localized in the mitochondrial membrane. This observation was fully confirmed by double immunostaining of CI and CIV. In fact, the low and sparse residual expression of the three subunits was evident in the images.

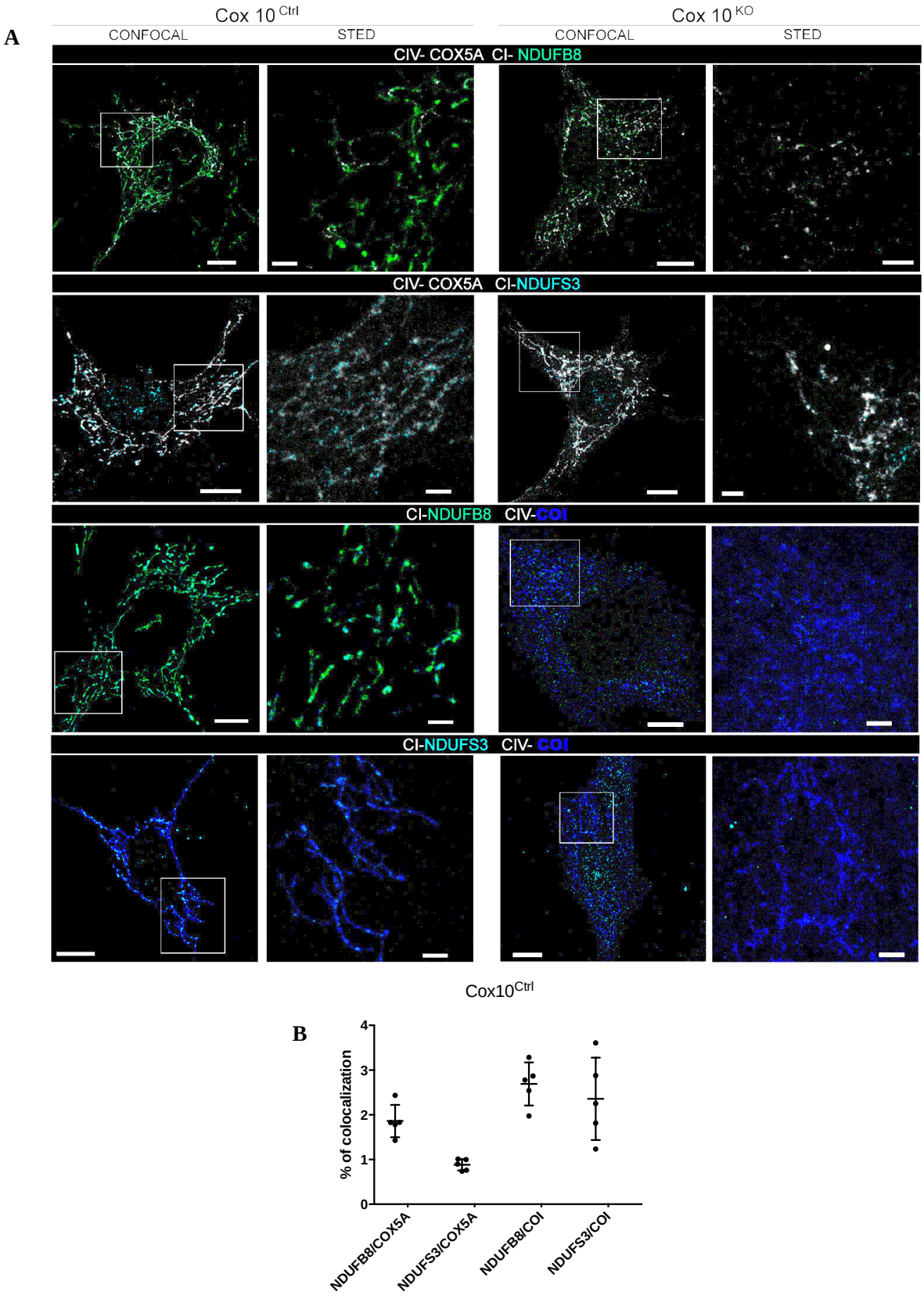

Figure 42. Immunostaining of endogenous CI (NDUFB8 and NDUFS3) and CIV-containing subunits (COX5A and COI). **(A)** Confocal and STED images of Cox10^{Ctrl} and Cox10 ^{KO} cells labeled endogenously with anti-COX5A(white), anti-COI (blue), anti-NDUFB8 (green) and anti-NDUFS3 (cyan). Confocal scale bars: 10 µm. STED scale bars: 2 µm**.** **(B)** % of colocalization for CI and CIV in Cox10^{Ctrl} cells. 5 STED-ROI on replicated cells.

I.6.2 CYTb^{Ctrl} and CYTb^{M}

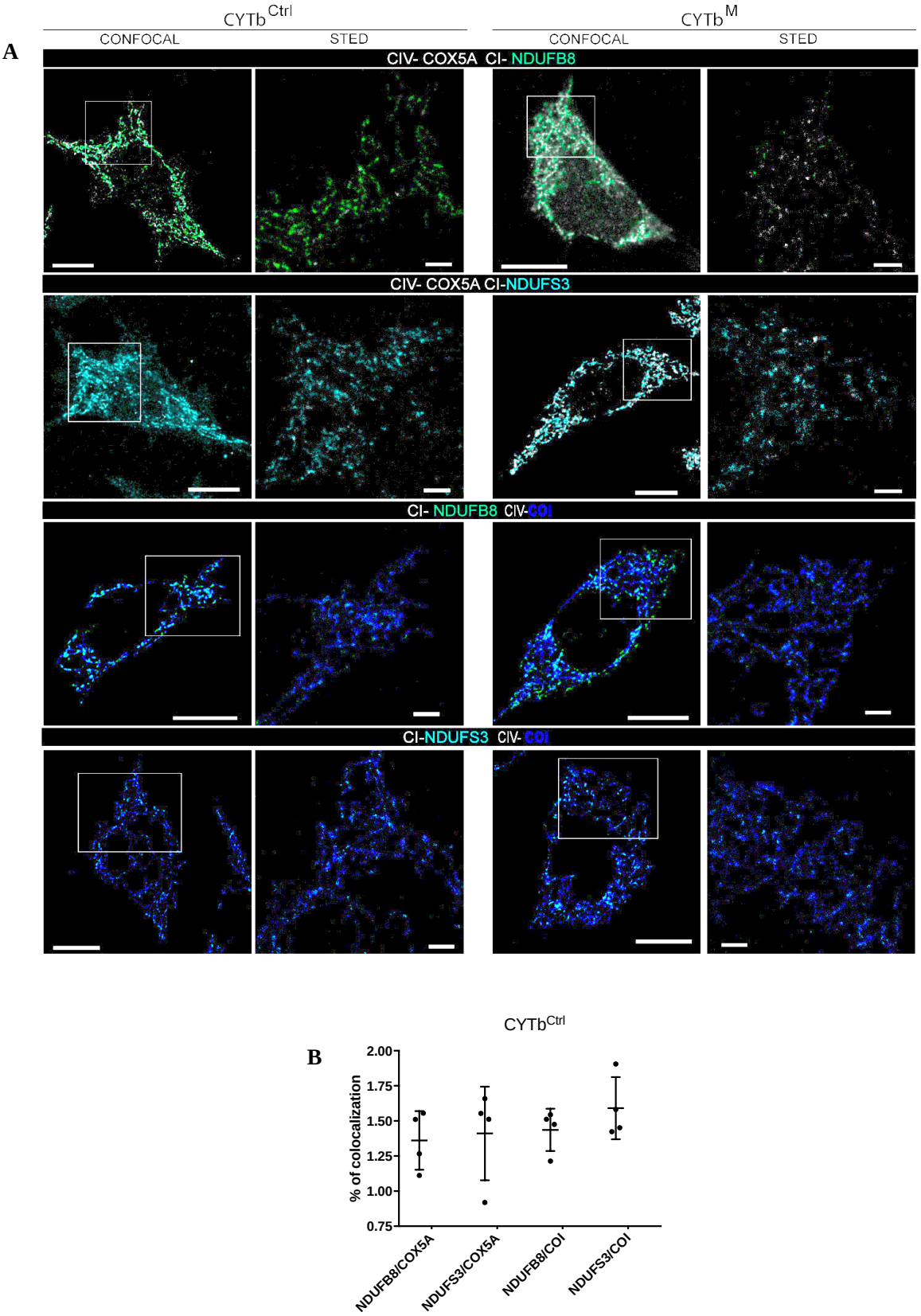

Figure 43. Immunostaining of endogenous CI (NDUFB8 and NDUFS3) and CIV-containing subunits (COX5A and COI). **(A)** Confocal and STED images of CYTb^{Ctrl} and CYTb^{M} cells labeled endogenously with anti-COX5A(grey), anti-COI (blue), anti-NDUFB8 (green) and anti-NDUFS3 (cyan). Confocal scale bars: 10 µm. STED scale bars: 2 µm**. (B)** % of colocalization for CI and CIV in CYTb^{Ctrl} cells. 5 STED-ROI on replicated cells.

A notable level of co-occurrence between complex I and complex IV in $CYTb^{Ctrl}$ cells was observed, non-dependent on the immunomarker used. When selected areas were studied in STED, partial close proximity in these complexes was confirmed (Figure 43A).

The overall colocalization in replicated STED analysis shown in FIGURE XB supported the conclusion that in $CYTb^{Ctrl}$ cell, complex I and IV pair combinations indicated similar spatial distribution, non-dependent in the combination used (Figure 43B).

The confocal analysis of $CYTb^{M}$ cells indicated a distribution pattern of proximity between CI and CIV. The increase in resolution in the STED area, elucidated that this proximity was not identified. The low and sparse residual expression of complex I subunits was evident in the confocal images and STED images (Figure 43A).

I.6.3 ρ^+ and ρ^0

Confocal analysis shows extensive co-localization of CI and CIV independently on the subunits used as immunostaining marker. When selected areas were imaged in super resolution we could confirm a high degree of proximity in control cells. In addition to super complexes, STED also clearly evidenciated the presence of individual subunits (Figure 44A).

We next determined the colocalization in replicated STED experiments (Figure 44B) that univocally probed the proximity in the particles. The quantitative % of colocalization also confirmed the differences observed in the case of NDUFS3/ COI pair, which showed 3-fold lower co-localization index.

Single subunit localization experiments (Results I.3.3) indicated that the expression of NDUFB8, NDUFS3 and Co-I in ρ^0 cell line was negligible and not specifically localized in the mitochondrial membrane. However, COX5A expression was distributed along ρ^0 mitochondria.

Only COX5A co-stained cells had signal sufficient for STED-ROI analysis. Even though some co-localization appeared in confocal images, at nanoscale resolution both NDUFS3/COX5A and NDUFB8/COX5A protein pairs appeared as isolated entities (Figure 44A).

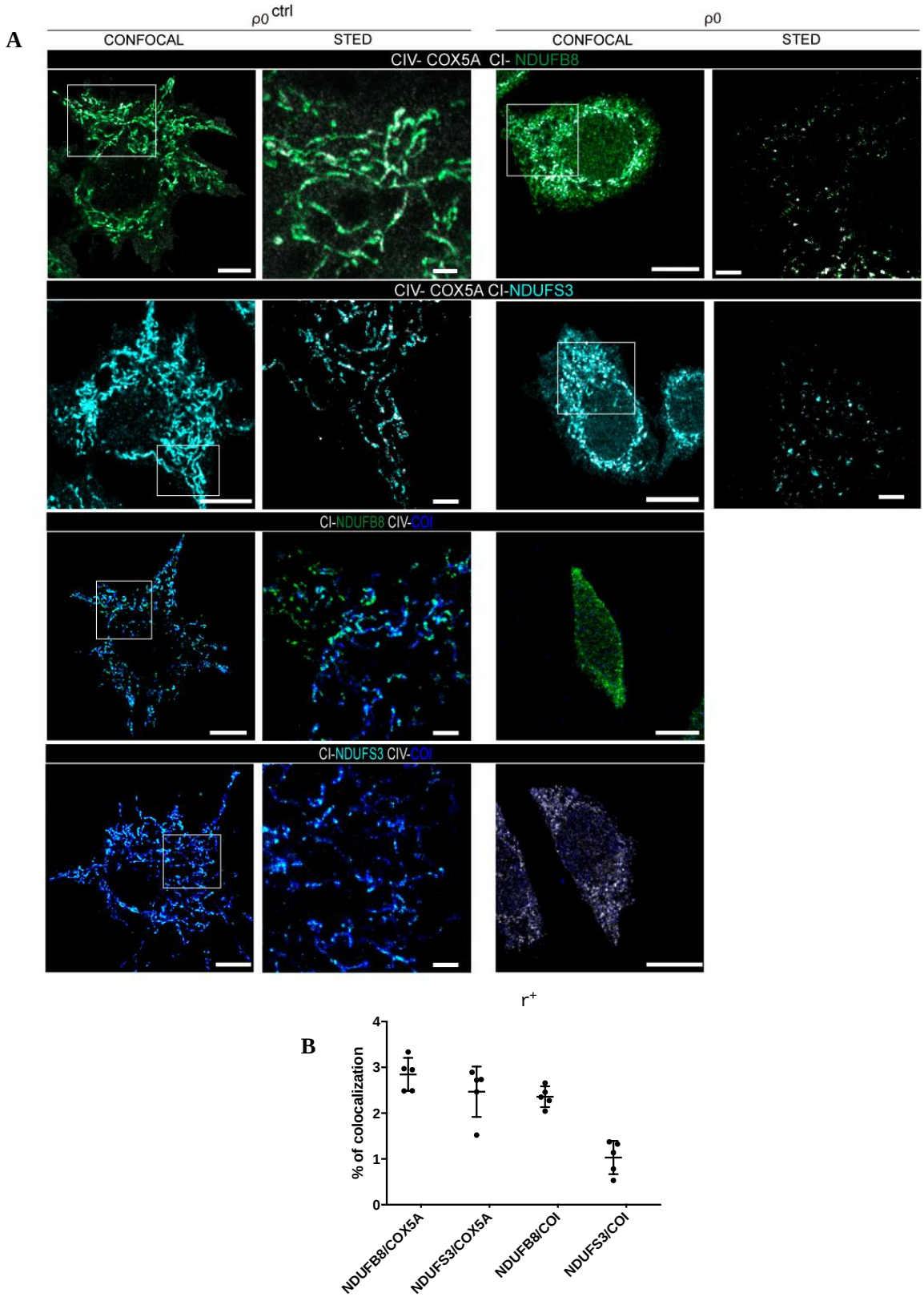

Figure 44. Immunostaining of endogenous CI (NDUFB8 and NDUFS3) and CIV-containing subunits (COX5A and COI). (A) Confocal and STED images of ρ^+ and ρ^0 cells labeled endogenously with anti-COX5A(grey), anti-COI (blue), anti-NDUFB8 (reen) and anti-NDUFS3 (cyan). Confocal scale bars: 10 µm. STED scale bars: 2 µm**. (B)** % of colocalization for CI and CIV in ρ^+ cells. 5 STED-ROI on replicated cells.

I.7 *In situ* cellular localization of CI, CIII and CIV subunits

To determine the proximity of CI, CIII and CIV we optimized a 3-colour immunostaining. We selected one subunit for each mitochondrial complex based on the antibody selection criteria applied in this work. Among all the combinations, the only 3 subunits that can be co-labelled were NDUFB8, Rieske and COX5A, because of the secondary antibodies constrains (Table 3 Material and Methods).

I.7.1 Cox10^{Ctrl} and Cox10^{KO}

Confocal images of Cox10^{Ctrl} cells show extensive proximity of CI, CIII and CIV when we performed the triple immunostaining. When ROIs were imaged in super resolution we could quantitatively detect co-occurrence in the control cells (Figure 45) in addition to verify the presence of isolated CI, CIII and CIV signals.

The quantitative analysis of the distribution of the complexes is reported in Results I.8 in detail.

Individual subunit localization analysis (Results I.3.1) indicated that the expression of NDUFB8 in the mutant cell line was negligible. Rieske and COX5A were homogeneous distributed along the mitochondria in these cells. Confocal images presented extensive co-occurrence in the mutant cells. However, when the STED ROIs were studied we found delocalized distribution in these subunits without overlaps between signals in Cox10^{KO} images.

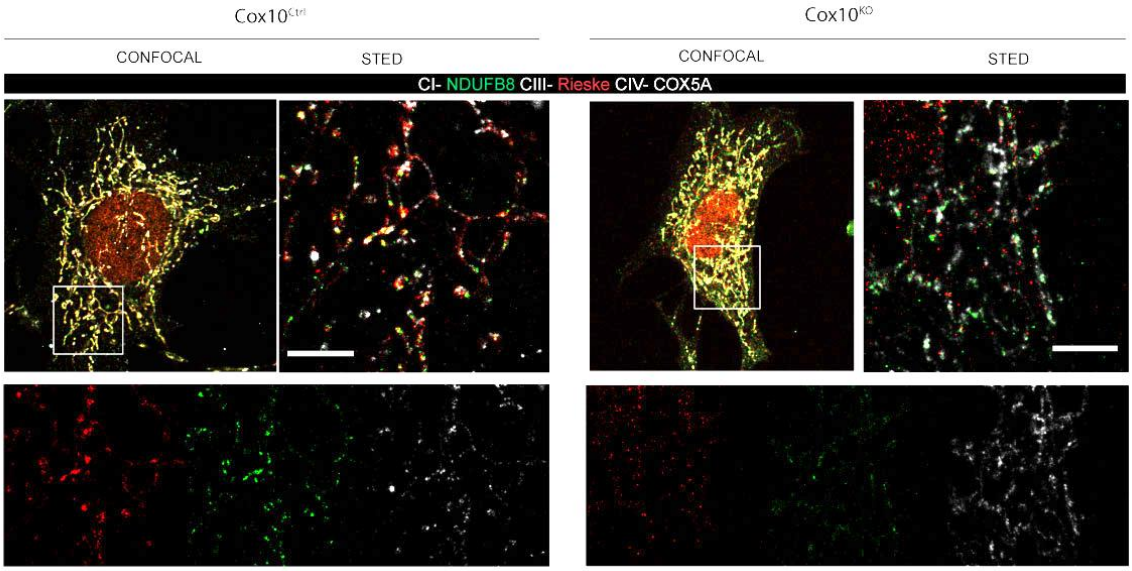

Figure 45. Immunostaining of endogenous CI (NDUFB8), CIII (Rieske) and CIV (COX5A). Confocal and STED images of Cox10^{Ctrl} and Cox10^{KO} cells labeled endogenously with anti-NDUFB8 (green), Rieske (red) and anti-COX5A(grey). Confocal scale bars: 10 µm. STED scale bars: 2 µm.

I.7.2 CYTb^{Ctrl} and CYTb^{M}

A notable level of co-occurrence between complex I, complex III and complex IV in CYTb^{Ctrl} cells was observed. When selected areas were studied in STED, proximity in these complexes was fully confirmed.

The result of single subunit localization (Results I.3.2) indicated that the expression of COX5A and NDUFB8 in CYTb^{M} cell line was mitochondria specific. However, the expression of Rieske in this cell line was negligible and not specifically localized in the mitochondrial membrane. All these observations were fully confirmed by triple immunostaining of CI, CIII and CIV (Figure 46).

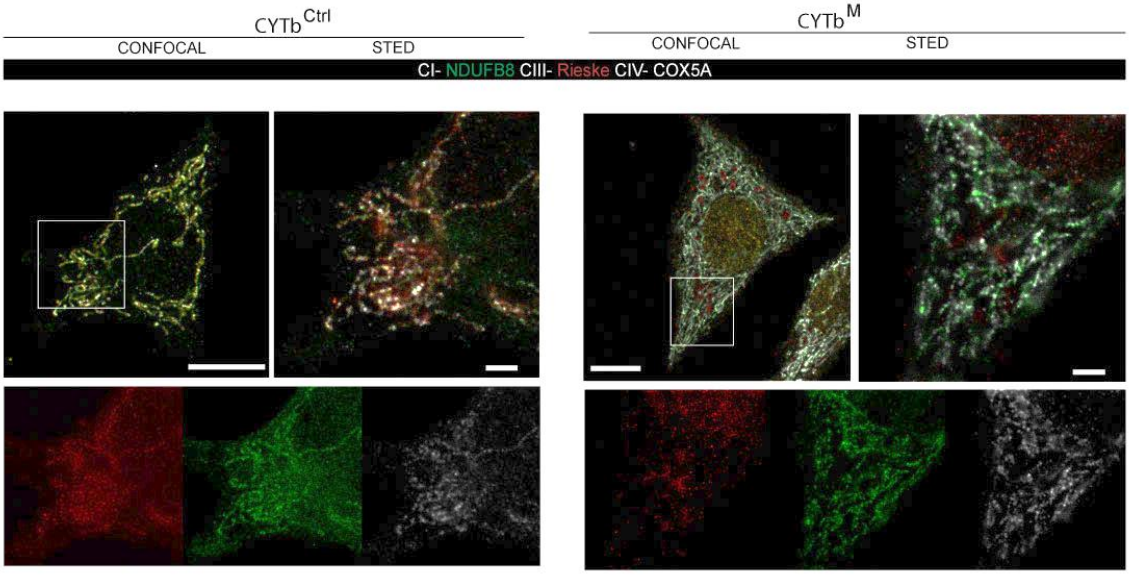

Figure 46. Immunostaining of endogenous CI (NDUFB8), CIII (Rieske) and CIV (COX5A). Confocal and STED images of CYTb^{Ctrl} and CYTb^{M} cells labeled endogenously with anti-NDUFB8 (green), Rieske (red) and anti-COX5A(grey). Confocal scale bars: 10 µm. STED scale bars: 2 µm.

I.7.3 ρ^+ and ρ^0

Confocal analysis showed dense and extensive co-localization that was confirmed by imaging in super resolution in control cells. In addition to super complexes, STED also clearly evidence the presence of individual subunits.

Previous experiments to determine the cellular localization of the subunits, determined that ρ^0 cell line did not express Rieske. Moreover, NDUFB8 and COX5A, although detectable, were not found to colocalize. These observations were confirmed in the triple immunostaining of CI, CIII and CIV subunits from confocal images. STED-ROI experiments detected null co-localization between CIII and the other two subunits (Figure 47).

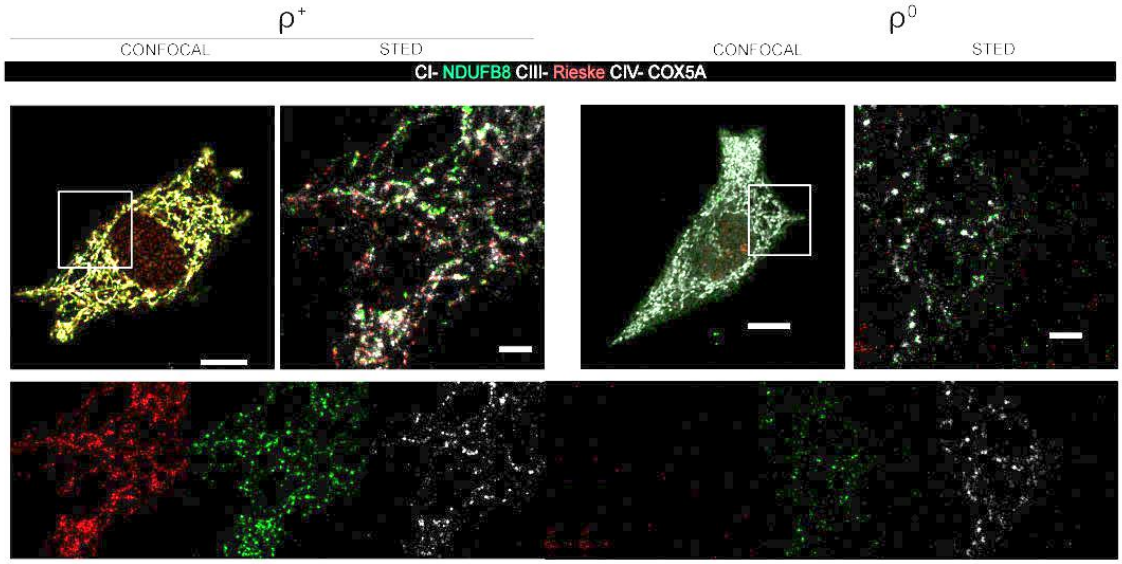

Figure 47. Immunostaining of endogenous CI (NDUFB8), CIII (Rieske) and CIV (COX5A). (A) Confocal and STED images of ρ^+ and ρ^0 cells labeled endogenously with anti-NDUFB8 (green), Rieske (red) and anti-COX5A(grey). Confocal scale bars: 10 µm. STED scale bars: 2 µm.

I.8 Quantitative analysis of complex distributions

I.8.1 Colocalization in (x,y) 3 color STED images

Quantitative determination of the distribution between complexes in situ was achieved using FIJI open source software (Command line details in Material and Methods-IV.6.1).

The images were first post processed by channel to eliminate background. A Gaussian filter between 0.5-0.7 was also applied to improve signal-to-noise ratio.

The mitochondria network was probed with vectors 300nm large and of variable length (6-10µm). Intensity profile of each channel along the selected vector was then measured.

Figure 48 shows the results for three $Cox10^{Ctrl}$ replicated cells. The dynamics of supercomplex assembly was clearly detected by the superimposition of intensity peaks.

The intensity profiles clearly demonstrate the presence of different mitochondrial assembly status. The superimposition of intensity peaks recognizes in the same individual cell the presence of free CI, CIII and CIV. Supercomplex combinations III_2 +IV; In +IIIn and the respirasome I+III_2+IV can also be identified.

Previous analysis confirmed the presence of super-complexes containing CI and CIV (Müller *et al.*, 2016), as confirmed in our work.

Similar demonstration was achieved in the other two model cell lines $CYTb^{Ctrl}$ and ρ^+ as shown in Figure 49 and Figure 50, respectively.

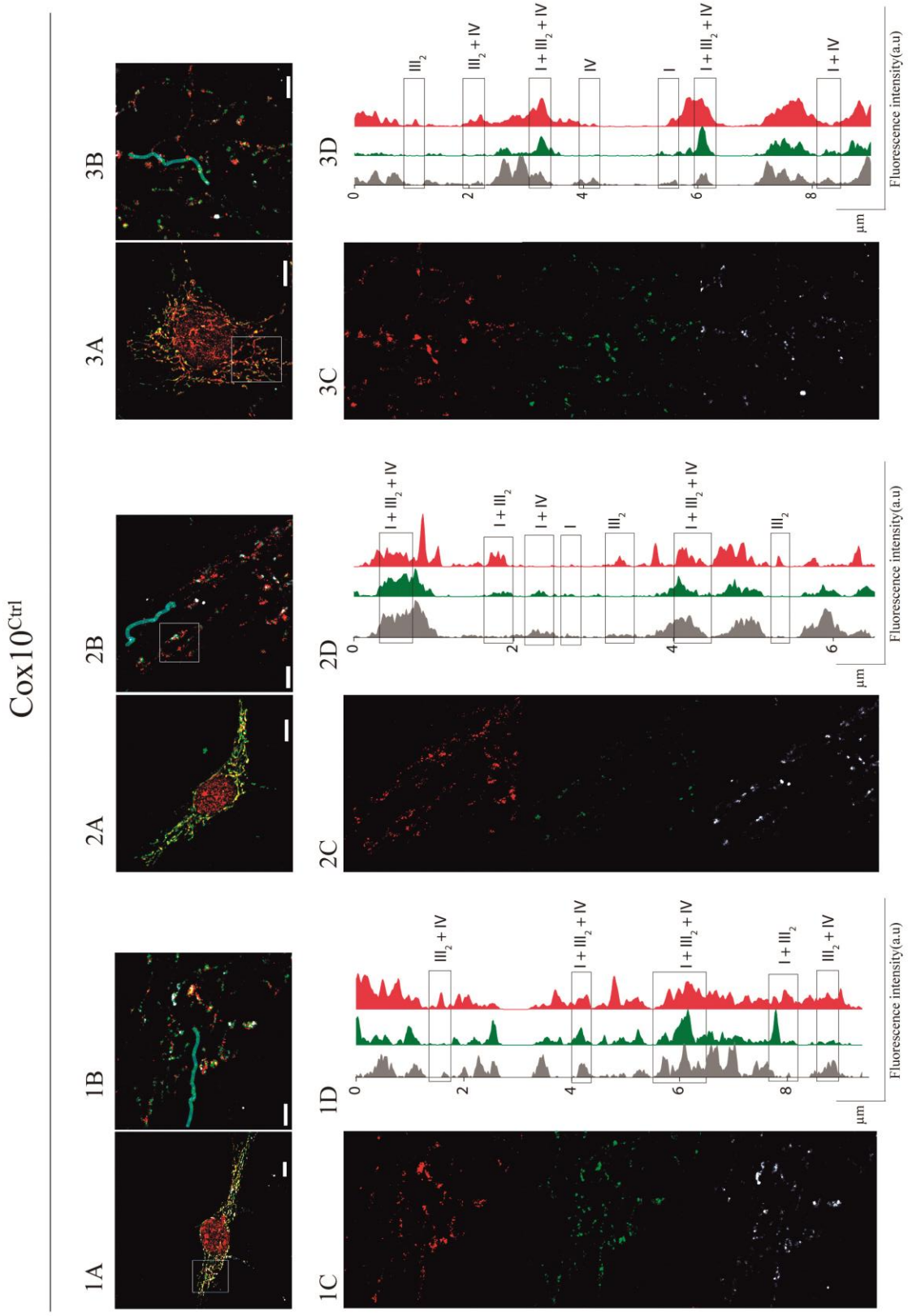

Figure 48. Intensity profiles along mitochondria network. 1A, 2A, 3A. Confocal images of three different cells. **1B, 2B, 3B**. STED-ROI in which the probing vector are shown in turquoise. **1C, 2C, 3C** Channels over imposed in B correspond to NDUFB8(green), Rieske(reed) and COX5A(grey). **1D, 2D, 3D** Normalized intensity profiles along the selected vectors for each channel.

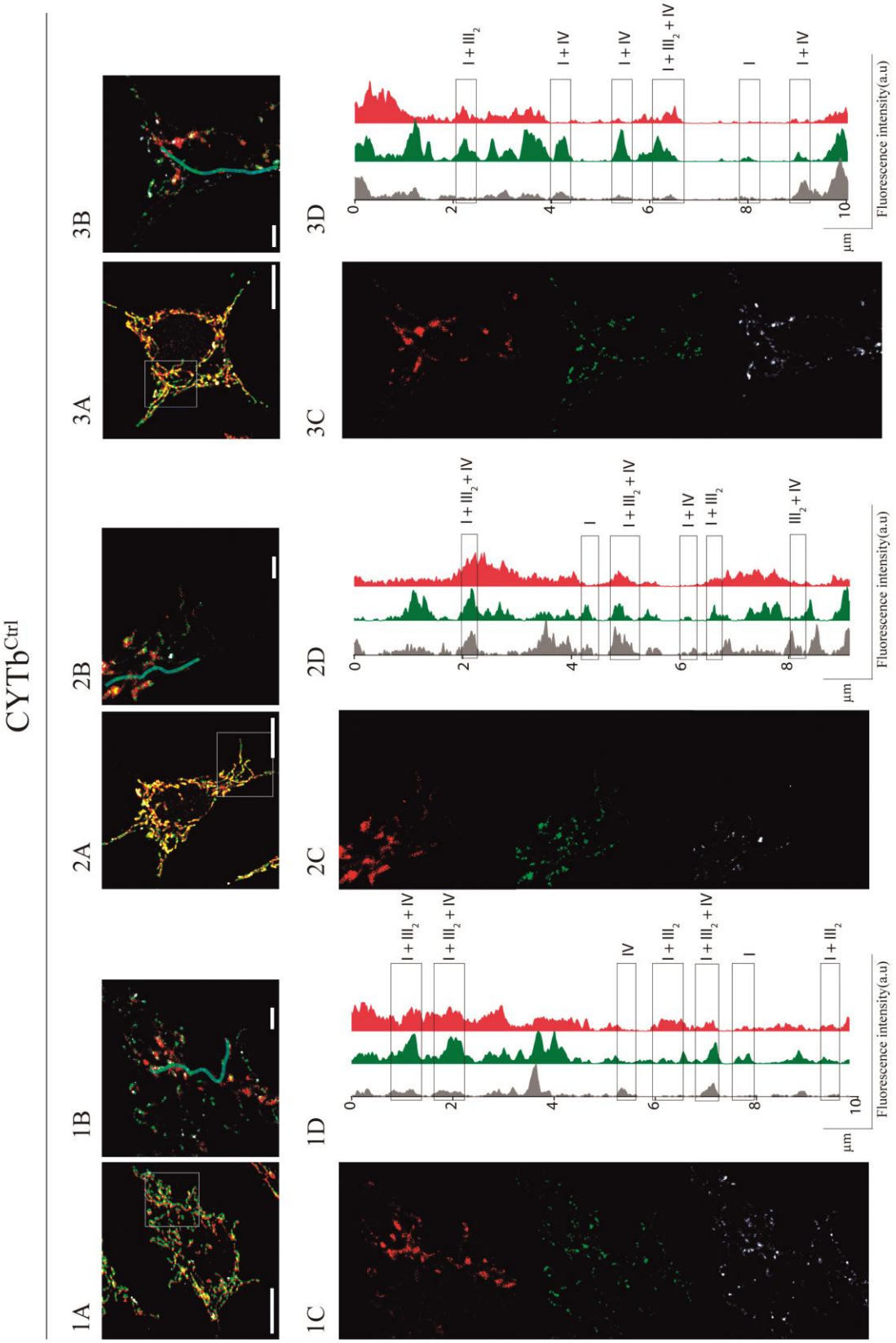

Figure 49. Intensity profiles along mitochondria network. 1A, 2A, 3A. Confocal images of three different cells. **1B, 2B, 3B**. STED-ROI in which the probing vector are shown in turquoise. **1C, 2C, 3C** Channels over imposed in B correspond to NDUFB8(green), Rieske(reed) and COX5A(grey). **1D, 2D, 3D** Normalized intensity profiles along the selected vectors for each channel.

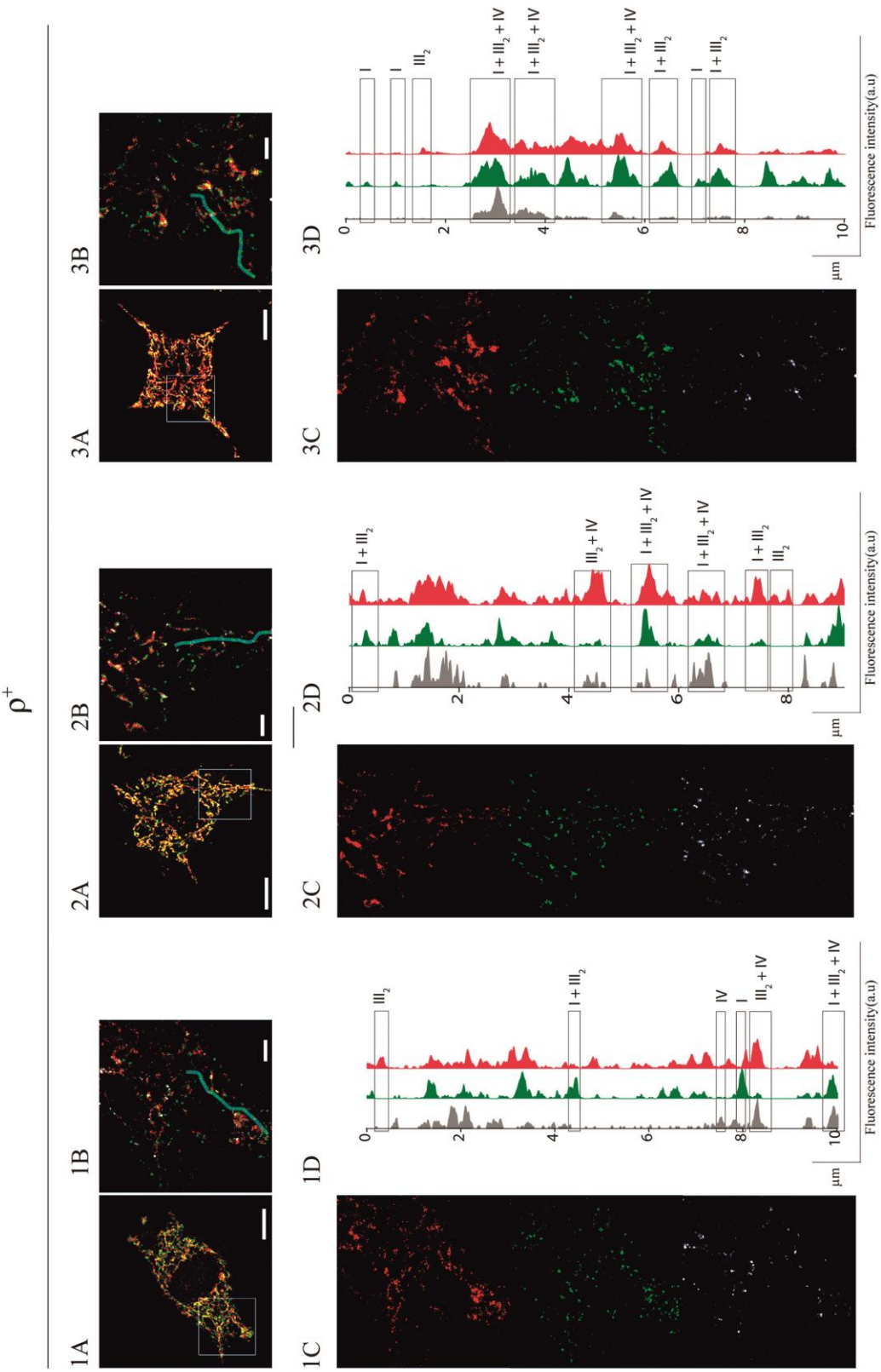

Figure 50. Intensity profiles along mitochondria network. 1A, 2A, 3A. Confocal images of three different cells. **1B, 2B, 3B**. STED-ROI in which the probing vector are shown in turquoise. **1C, 2C, 3C** Channels over imposed in B correspond to NDUFB8(green), Rieske(reed) and COX5A(grey). **1D, 2D, 3D** Normalized intensity profiles along the selected vectors for each channel.

I.8.2 3D reconstruction from (x,y,z) 3 color STED images

The estimation of the relative volume of immunostained complexes and supercomplexes in situ was achieved by acquiring (x, y, z)- STED images. It is important to notice that STED-depletion was applied along the three (x, y, z) axis in order to obtain the most possible quasi-isotropic voxel as illustrated in Figure 31.

With this work, we have implemented stimulated emission depletion (STED) microscopy with simultaneous three-dimensional super-resolution imaging in three colors. In order to achieve maximal depletion efficiency, we worked in resonant mode for the acquisition of the images. The quasi isotropic volume was in the range of x=y=z ≈ 240nm.

To develop this experiment, we selected the cell line $Cox10^{Ctrl}$, that presented a preserve mitochondrial network and optimal detection of all mitochondrial subunits.

We developed then the 3D reconstruction about 500nm volume, as described in Material and Methods I.V.6.2. In the 3D- rendering and volume reconstruction we applied a suitable pseudo-color scale for optimal visualization.

We observed dense and extensive proximity of CI, CIII and CIV in Figure 51A and Figure 51B. Moreover, when 3D reconstruction was analyzed we confirmed this dense distribution with specific mitochondrial localization (Figure 51C).

3D STED-ROIs clearly identified the presence of different associations between complexes, as highlighted in the images. We identified relative abundance profiles of respiratory chain complexes I, III and IV and supercomplexes. Molecular heterogeneity of individual complexes was visible in all the samples analyzed (Figure 51 D).

The images were acquired and processed as described in Material and Methods IV.6.2.

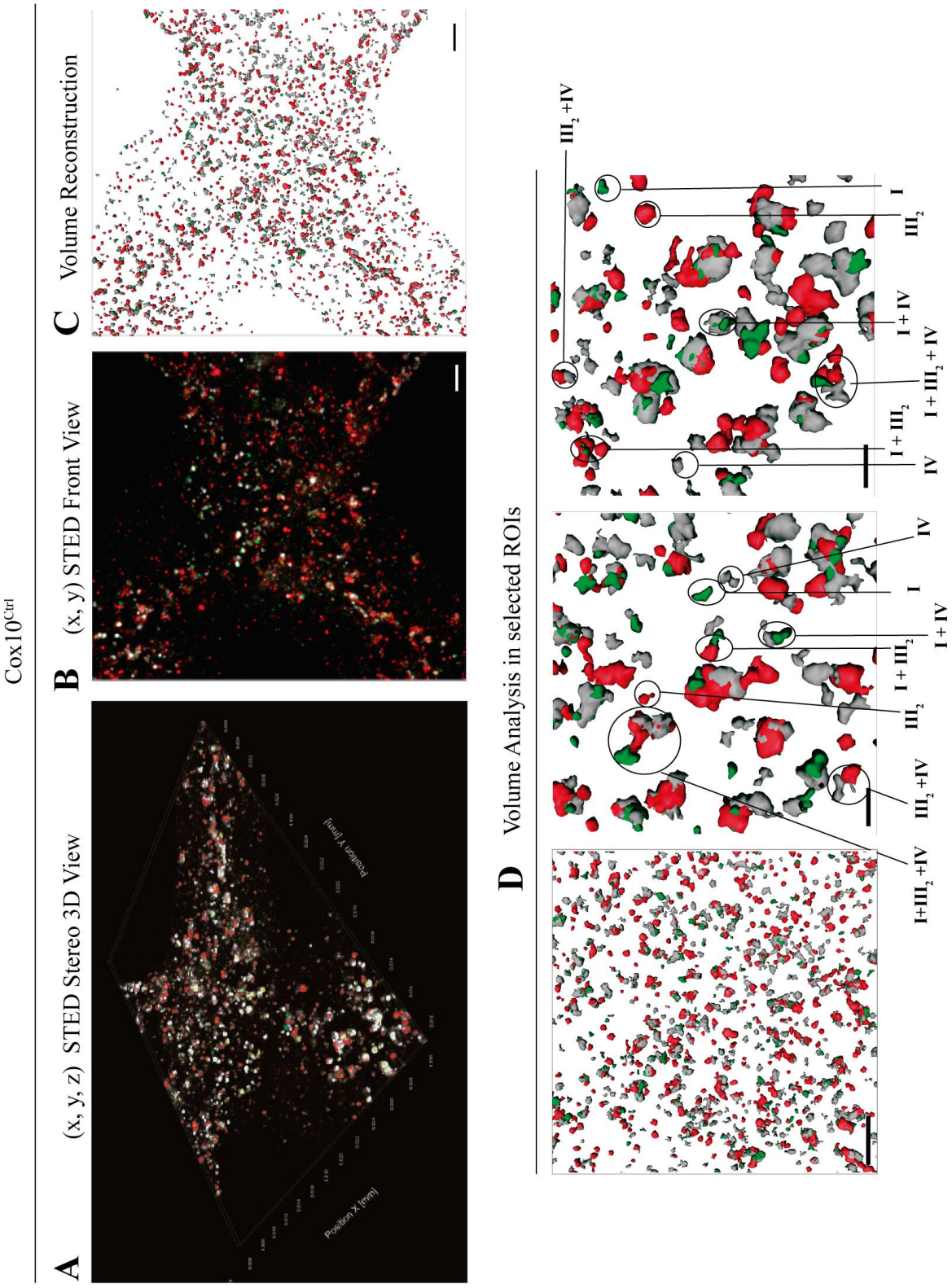

Figure 51. Cox10^{Ctrl} 3D reconstruction. (A) (x ,y ,z) STED Stereo 3D view **(B)** (x,y) front view of triple immunostained Cox10^{Ctrl} cells of green NDUFB8, red Rieske and grey COX5A. Scale bar 2µm **(C)** Volume reconstruction is shown with the same color code for each of the mitochondrial subunits Scale bar 2µm **(D)** Three different ROI. Scale bar 2µm, 0,5 µm and 0,5 µm, respectively.

The abundance of the complexes and supercomplexes is represented as % volumes computed in an optical depth of 500nm inside a cell (Figure 52).

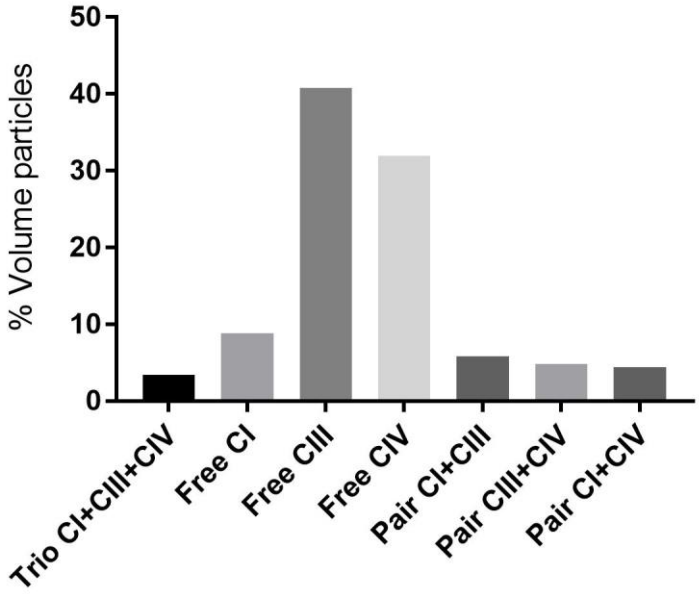

Figure 52. Particles Volume from the 3D reconstruction. Sum Volume for each subunit in μm^3. The analysis was done on the individual subunits, pairs and trios found in the 3D reconstruction from 4 different cells which were done in 3D tricolor STED.

To ensure the question whether immunostaining-STED analysis recapitulates the plasticity model proposed on the basis of the BNGE (Figure 53), we run in parallel the standard biochemistry applying identical triple detection. This experiment, revealed the different assembly status of the three subunits used in this chapter, as free subunits or superassembled in the following SC combinations: III_2+IV; In + IIIn and SC I + III_2 + IV.

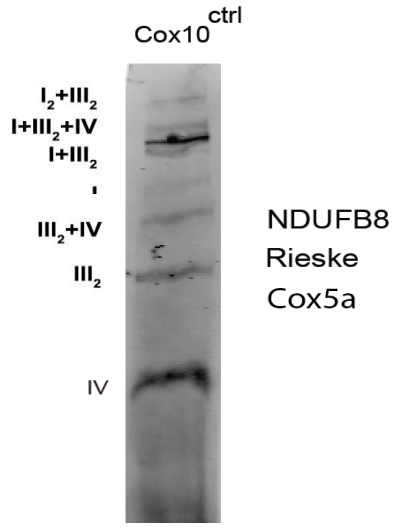

Figure 53. Analysis of the Assembly Status of the Different OXPHOS Complexes. Blue-Native gel electrophoresis of the mitochondrial OXPHOS complex I, III and IV. Subunits used NDUFB8, Rieske and COX5A for the cell line $Cox10^{Ctrl}$.

II. Compensatory pathways for OXPHOS deficiency

One of the puzzling observations from mtDNA-linked diseases is that two patients with exactly the same mutation may manifest very different collections of symptoms ranging from no-diseases to a life-threatening syndrome. The majority of the complex III genetic defects characterized to date are due to mutations in cytochrome b. Our group isolated the first mouse cells ($CYTb^{M}$) harboring a defective mutation in CYTb, a G15263A mutation in the mtDNA that causes an amino acid substitution from E to K (Acín-Pérez 2004). When described, this mutation impeded the assembly of CIII. Later, we isolated a sub-clone of this cell line ($CYTb^{S}$) that despite having the same mutation, was able to assemble a low amount of CIII, sufficient to allow growth of the cells in galactose (Lapuente-Brun *et al.*, 2013). The molecular cause of this functional reversion was unclear. Therefore, we have $CYTb^{M}$ and $CYTb^{S}$, two mouse cell models with the same mutation but with different phenotype, a condition that resemble that of the patients.

The entire set of cDNAs for structural complex III subunits as well chaperones BCS1L and OXA1 did not reveal mutations that would explain the suppressor phenotype in the $CYTb^{S}$ (Raquel Moreno-Loshuertos (2009). "DNA mitocondrial: de la variabilidad poblacional a las mutaciones patologicas". Universidad de Zaragoza). Here we analyzed in deep the biochemical and molecular phenotype of the $CYTb^{S}$ cells and we performed RNASeq analysis to inquire for a molecular explanation for this reversion.

II.1 G15263A Mutation and OXPHOS performance

We confirmed the presence in our cells lines, $CYTb^{Ctrl}$, $CYTb^{S}$, $CYTb^{M}$, of the G15263A mutation in the mt-CYTb from complex III as described in (Acín-Pérez 2004).

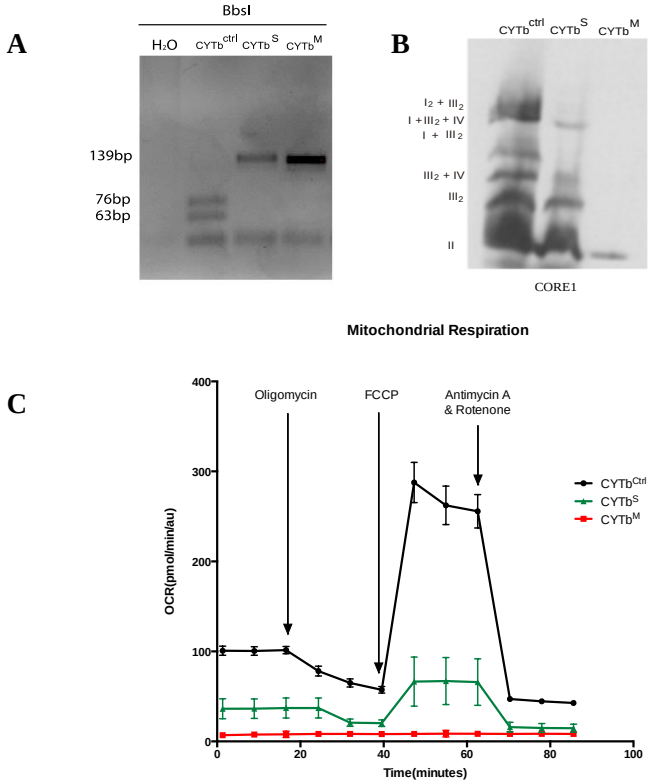

Figure 54. Characterization of the CYTb mutation and functional analysis of OXPHOS performance (A) RFLP analysis of the presence and homoplasmic status for the G15263A transition that disrupts a restriction site for BbsI was demonstrated for both $CYTb^{S}$ and $CYTb^{M}$ cells lines, but nor $CYTb^{Ctrl}$ or H_2O. **(B)** Blue-Native gel electrophoresis (BNGE) probed against CORE 1 protein of the mitocondrial OXPHOS complex III with the anti CORE 1 protein in the $CYTb^{ctrl}$, $CYTb^{S}$, $CYTb^{M}$ cells lines. **(C)** Representation of Oxygen Consumption Rate (pmol/min/au) obtained after the SeaHorse measurement for the 3 cell lines. The injections media are represented at different time points and the drugs used are: FCCP, Olygomicin and Rotenone + Antimicin.

The sequence present in the mutated form of the gen A15263, creates a recognition site for the enzyme BbsI. This site is not present when the variant of this mutant appears G15263. The analyzed fragment obtained from the RFLP is about 138bp. Therefore, we recognize the same mutation within the CYTb in the cell lines $CYTb^{M}$ and the $CYTb^{S}$ (Figure 54A)

Next, we evaluated the assembly of the bc1 complex, using the antibody anti-complex III CORE1 protein. In the control cells we found, free complex III and the association between complex I and IV. In the mutant cell line $CYTb^{M}$ no assembled complex III could be observed either as free form or superassembled with other complexes, confirming that CIII is not assembled in cells carrying the CYTb mutation. However, the $CYTb^{S}$ showed a lower amount of both free and superassembled CIII, despite of having the same mutation in the CYTb, (Figure 54B).

While $CYTb^{M}$ cells were unable to respire, the low level of assembled CIII in $CYTb^{S}$ cells was sufficient to restore the respiratory capacity, albeit at lower rate than in controls (Figure 54C). As a consequence, $CYTb^{M}$ cells require glucose and uridine supplementation to growth, dying when transferred to galactose containing media and without uridine. $CYTb^{S}$ cells however, were able to growth in both media (Figure 55A-B).

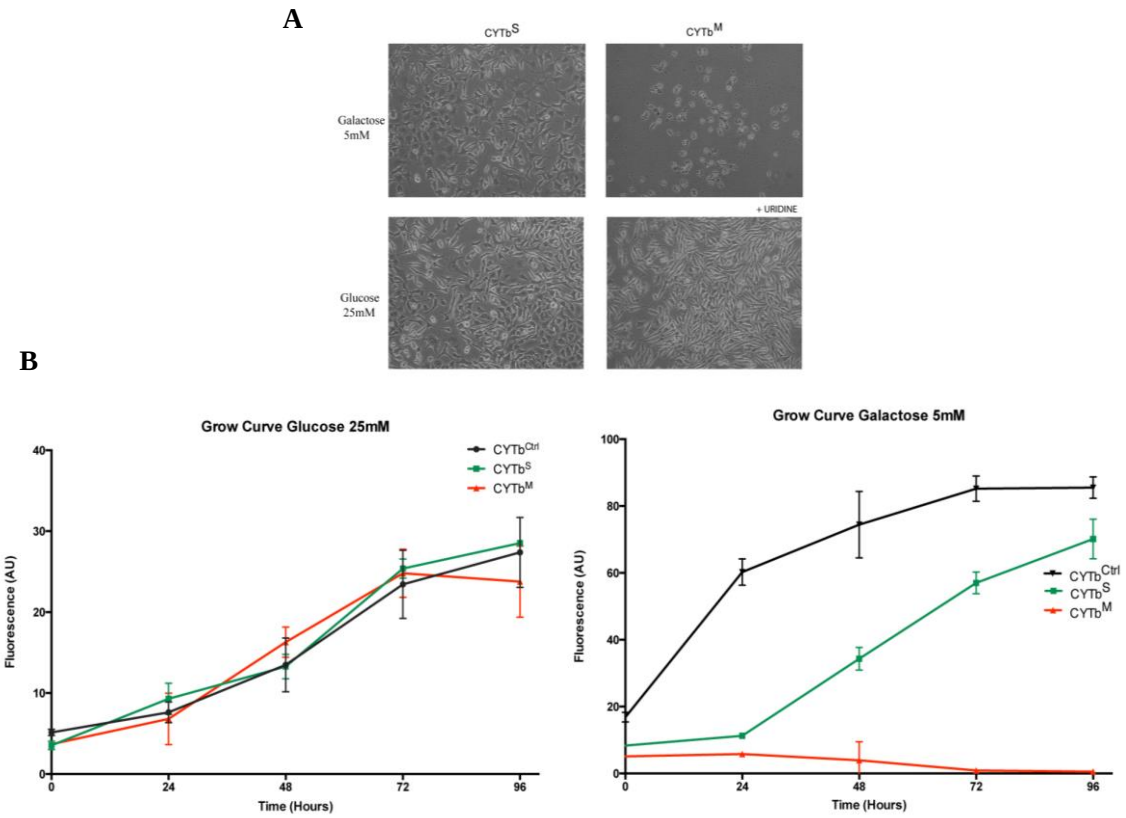

Figure 55. Cell viability analysis (A) Representative images of cultures containing the indicated $CYTb^{S}$ and the $CYTb^{M}$ at 48h, in the cultute media used in this manuscript. Galactose 5mM and Glucose 25mM, supplemented with uridine for the $CYTb^{M}$ cells. **(B)** Cell proliferation assay in glucose 25mM and galactose 5mM for the $CYTb^{Ctrl}$, $CYTb^{S}$, $CYTb^{M}$. Representation of the fluorescence in AU of average of the samples at 0, 24, 48, 72 and 96 hours.

Mitochondria Dynamics is impaired by OXPHOS deficiency

Mitochondria are highly dynamic organelles that are continuously monitored by the cells for their performance by different levels of quality controls. Among them, the capability to fuse and divide provides functional and morphological flexibility and is a key feature in mitochondrial quality maintenance and shorting of the impaired organelles for degradation.

To study the impact of different structural defects on the respiratory chain on the mitochondrial dynamics of our $CYTb^{M}$ cells and compare them with other types of OXPHOS deficiencies, cells without mtDNA (ρ^{o}) and cells with CIII but without CIV ($Cox10^{KO}$ cells) were used (Figure 56A). Our results showed that all mutants have reduced mitochondrial fusion compared with their isogenic controls (Figure 56B).

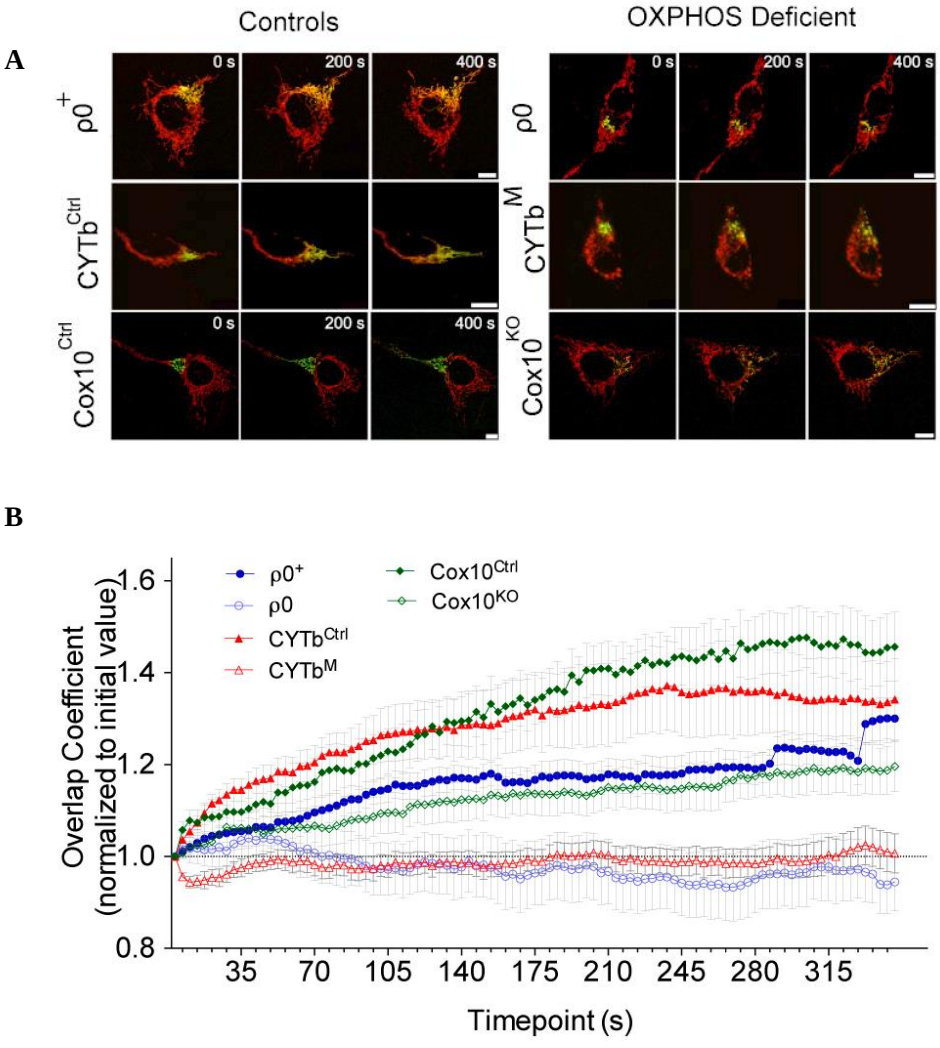

Figure 56. Mitochondrial dynamics of RCs mutant cell lines. (A) ρ^{0} and ρ^{+}, $CYTb^{M}$ and $CYTb^{Ctrl}$ cells, $Cox10^{KO}$ and $Cox10^{Ctrl}$ cells were transfected with mt-DsRed and mito-PAGFP. Mito-PAGFP was photoactivated, mt-DsRed was photobleached at t = 0 s. **(B)** Panel shows cells at a range of time points. Scale bar: 25 μm. Data show mean ± s.e.m (n = 10 for CYTb and Cox10, n= 8 for ρo cells). Two-away ANOVA was employed between each mutant and the respective control with the representative timepoints: ρ^{0} cells 294* and 336***, CYTb cells 84*, 126** and 178 s***, Cox10 cells 231*, 283** and 325*($p < 0.05$, **$p < 0.01$ and ***$p < 0.001$).

The suppressor phenotype depends on the mitochondrial metabolic demands

CYTb^{S} where isolated by growing high number of cells in galactose and in the absence of uridine to look for potential suppressors of the deficiency. These cells were regularly maintained in selective medium. To inquire is selective pressure was required to maintain the phenotype, we transferred CYTb^{S} cells to a non-selective medium containing glucose instead of galactose and supplemented with uridine. Immunoblot of digitonin-permeabilized mitochondria separated by BNGE and probed with monoclonal antibodies for CIII (anti-CORE1) and CIV (anti-COI) detected the assembled supercomplexes. When CYTb^{S} cells were kept long term in permissive medium they lost the ability to assemble CIII (Figure 57A). Therefore, the maintenance suppressor phenotype requires a continuous level of metabolic stress.

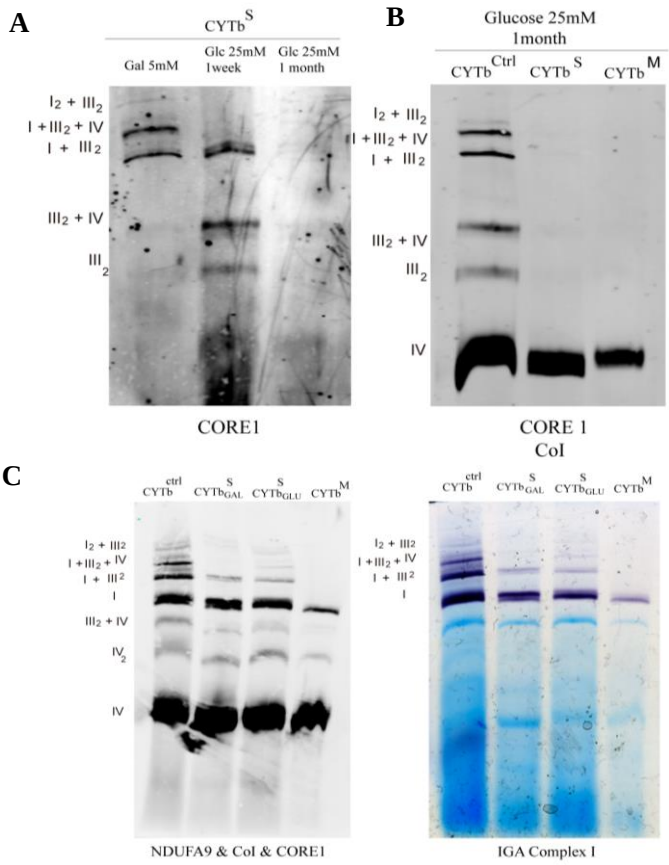

Figure 57. The effect of sugar source on the assembly of respiratory complexes was tested by the detection of complexes and SC in the mitochondria solubilized with digitonin by BN-PAGE for CI (NDUFA9), CIII (anti-CORE1) and CIV (anti-COI). **(A)** Different assembly pattern when we studied CYTb^{S} cell lines cultured in selection Galactose 5mM medium, and two times for Glucose 25mM. **(B)** CYTb^{Ctrl}, CYTb^{S}, CYTb^{M} cells lines in Glucose 25mM long term culture conditions**. (C)** The effect of sugar source on the rest of the respiratory complexes was tested by BN-PAGE. CYTb^{M} presented assembly CI, despite of the lack of CIII that was further studied with the IGA for CI in the right panel, finding an active CI for this mutated cell line.

The effect of sugar source on the assembly of respiratory complexes was tested by the detection of complexes and SC in the mitochondria solubilized with digitonin by BN-PAGE for CI (NDUFA9), CIII (anti-CORE1) and CIV (anti-COI) (Figure 57B). The lack of CIII in our cell line CYTb^{M} promotes degradation of CI immediately after its assembly (Lapuente-Brun *et al.*, 2013).

This observation was even more puzzling when it was revealed that the physical ablation of CIII destabilizes CI, by making CI susceptible to active degradation within mitochondria. However, after several years of continuous culture, lack in CIII, does not promote the full degradation of CI and a stable band of free CI can be observed (Figure 57C left).

Moreover, In Gel activity assay for CI was performed, finding an active CI, as the one that we can find in our control or suppressor cells lines. (Figure 57C right).

RNA sequencing

To futher investigate the molecular processes leading to the supressor phenotype, we compared the transcriptome profile of $CYTb^{S}$ and $CYTb^{M}$ cells by RNA sequencing. Two sets of RNASeq experiments were performed by three biological replicas.

The Volcano plot summarizes the results of the RNAseq (Figure 58). The genes that are up/down regulated by at least 1-fold and have a p-value less than 0.05 are at the upper-right and lower-left corner of the plot and are highlighted in different colors. Significantly up regulated genes in $CYTb^{S}$ cell line are in green, significantly down regulated genes in $CYTb^{S}$ cell line are in purple. In yellow we have labeled those genes with changes that are significantly regulated (p value less than 0.05) but have less than 1-fold alteration. The remaining genes are shown in black. Interestingly, within the upregulated genes we identified several protease inhibitors (Serpina3 proteins) highly increased and the abnormal elevation of the hypoxia induced isoform of NDUFA4 a CIV subunit (NDUF4L2).

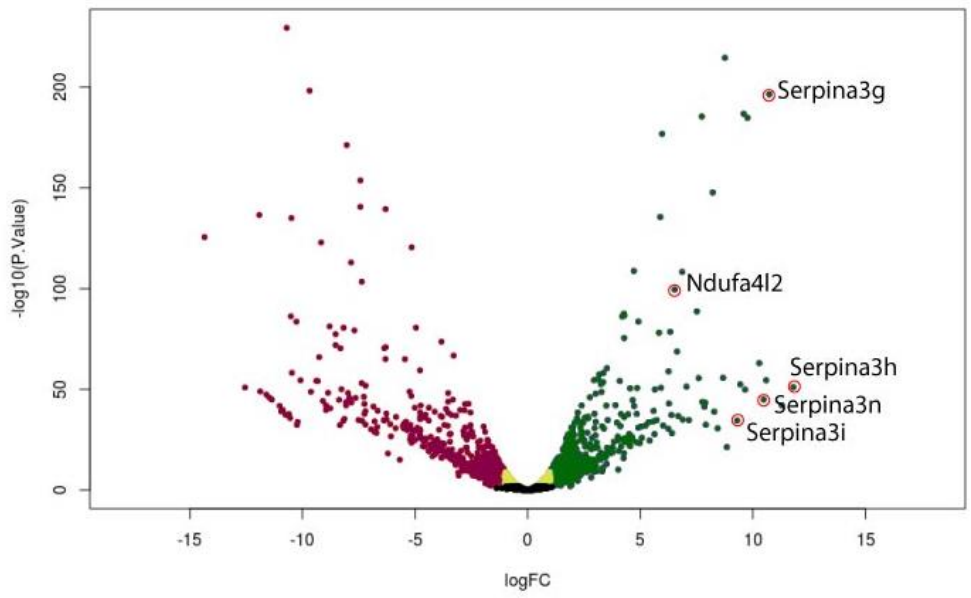

Figure 58. RNAseq Volcano Plot. The log fold change is plotted on the x-axis and the negative log10 p-value is plotted on the y-axis, between $CYTb^{S}$ and $CYTb^{M}$ cell lines. Each dot on the plot is a single gene. Colour coding is based on the fold change. We assign a a threshold for the fold change between -1 and 1 and significant p-value of 0.05. Significantly up regulated genes are in green, significantly down regulated genes are in purple. In yellow we have those genes with changes that are significantly regulated but have less than a single fold .The remaining features are in black.

II.2 SERPINA3

SERPINA3 is a member of the serpin super-family of protease inhibitors. The overexpression of this proteins in CYTb^{S} cells was confirmed by western blot and by immunofluorescence experiments (Figure 59A-C).

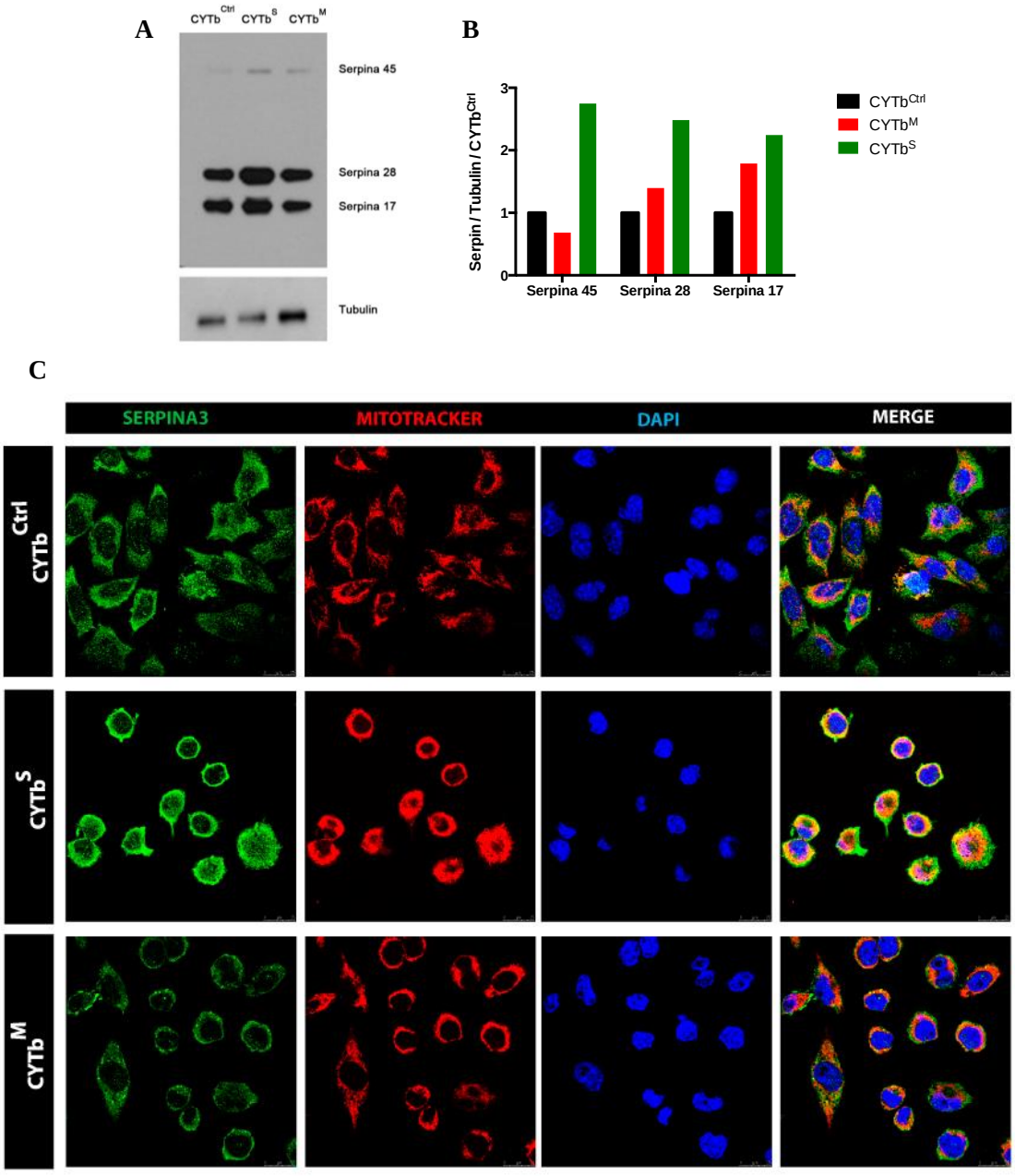

Figure 59. Serpina3 Expression Level. (A) Western Blot analysis of Serpina3 protein expression in the three cell lines used in this work. Tubulin as loading control. **(B)** WesternBlot quantification of the three isoforms **(C)** Immunofluorescence was performed on fixed cells for detection of endogenous Serpina3, mitochondrial network with Mitotracker and nuclei with DAPI. Composite image is shown. Images were adquired with a SP5 confocal system.

The overexpression of SERPINA3 may induce a decrease in cell adhesion to the extracellular matrix and to neighboring cells, and in doing that, it may protect from apoptosis (Chelbi *et al.*, 2012). We estimated by flow cytometry if the apoptotic tendency could be different in control, mutant and suppressor cells. Annexin-V was used to label apoptotic cells and DAPI was used to mark DNA and to determine cell viability. Thus, live cells were not labelled for either Annexin-V or DAPI, early apoptotic cells were Annexin-V positive and DAPI negative, and cells simultaneous labelled for Annexin-V and DAPI were positive for death. As shown in Figure 60, the CYTb mutation increases the frequency of early apoptotic cells (Annexin V^+) and non-viable cells. Interestingly, $CYTb^S$ cells present the same proportion of live cells than controls.

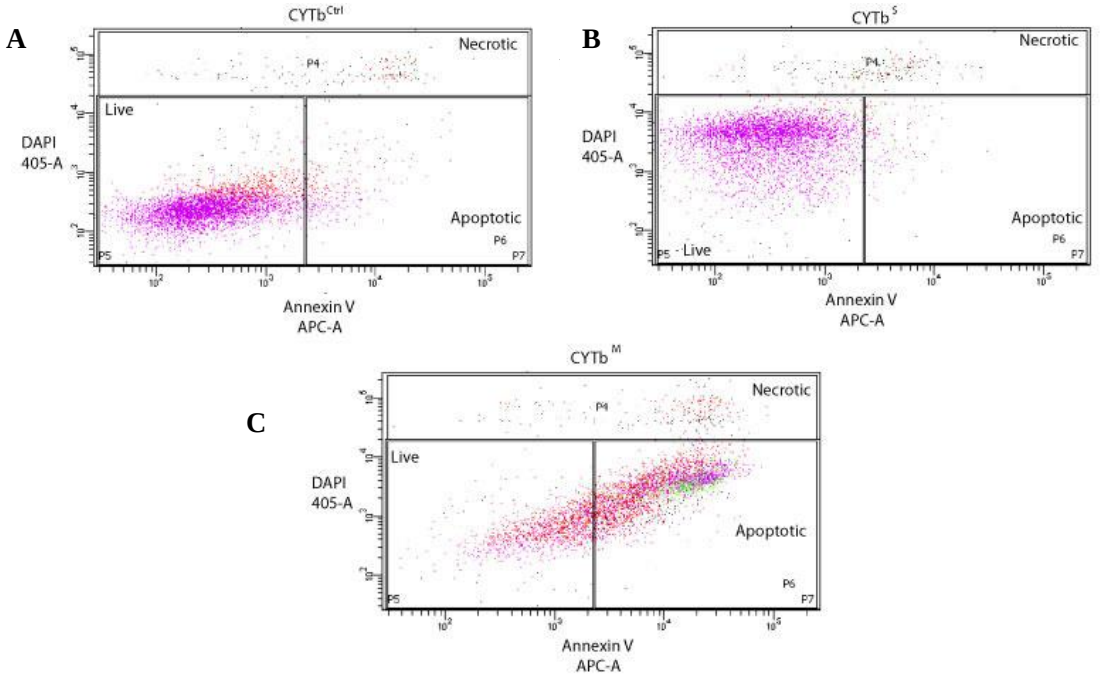

Figure 60. **Apoptosis detection by Flow Cytometry.** Cells were labelled with annexin V and a viability dye (DAPI) for **(A)** $CYTb^{Ctrl}$ cells **(B)** $CYTb^S$ cell line and **(C)** $CYTb^M$ cell line. Live cells, apoptotic and necrotic cells are shown in quadrants.

II.3 Induction of NDUFA4L2 expression

Cells collected for RNAseq were grown in normoxic conditions. In spite of that, NDUFA4L2, a gene known to be strongly induced by hypoxia (Tello et al., 2011), was overexpressed in $CYTb^{S}$ cells. Previous work from our group revealed that NDUFA4L2 expression is dependent of Hif1α, therefore, we determined by qPCR if other Hif1α targets were also upregulated (Figure 61A). As shown in figure 61A, the expression of several other Hif1α regulated genes were also upregulated in $CYTb^{S}$ but not in $CYTb^{M}$ cells in normal oxygen and in spite that Hif1α was not stabilized (Figure 61B). Interestingly, when cells were grown either in hypoxia or in normoxia but in the presence of DMOG to stabilize Hif1α, NDUF4L2 as well as Hif1α was upregulated in $CYTb^{Ctrl}$ cells. Hif1α was also stabilized by these two treatments in $CYTb^{M}$ and $CYTb^{S}$ cells. NDUF4L2 expression was not stimulated by the stabilization of Hif1α in $CYTb^{M}$ cells and was also overexpressed in $CYTb^{S}$ cells by a Hif1α insensitive regulation.

NDUFA4L2 is a mitochondrial inner membrane protein, we inquired if the overexpressed protein in the $CYTb^{S}$ cells maintains its cellular localization. As a positive control for cytoplasmic or mitochondrial localization, we used Actin and Tim23, respectively. NDUFA4L2 was only detected in the mitochondrial fraction under hypoxic conditions, confirming the mitochondrial localization of this protein (Figure 61C).

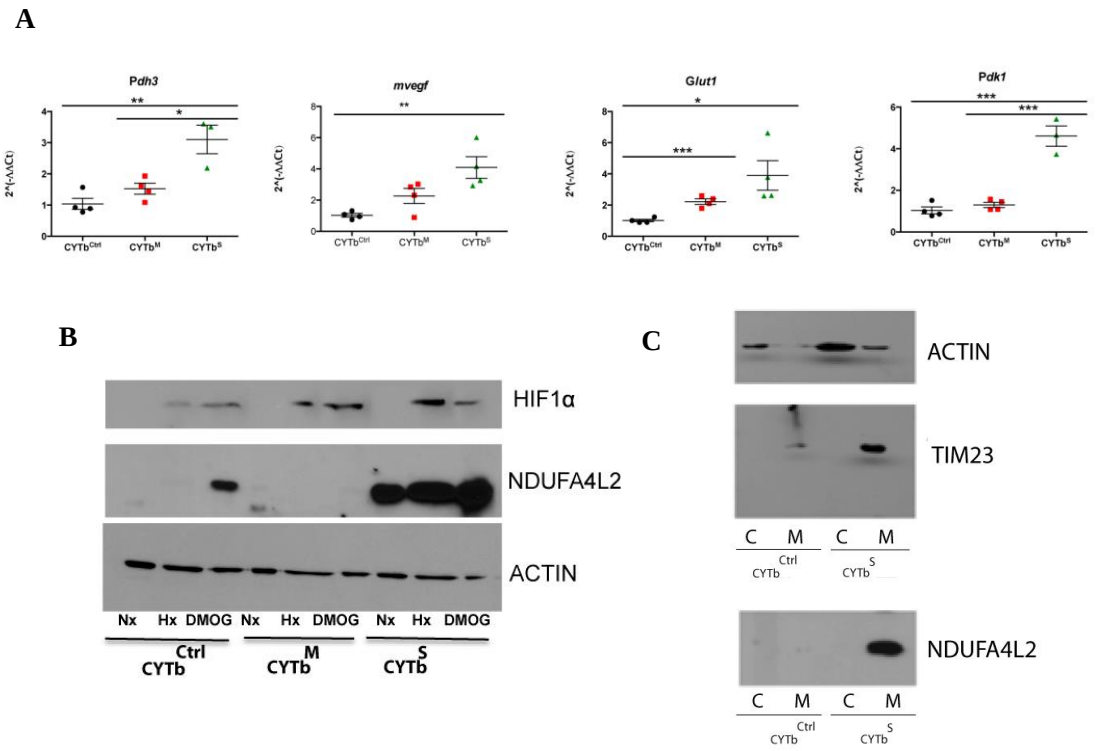

Figure 61. NDUFA4L2 Induction (A) Hif1α target genes validation by q-PCR Analysis of the cuadruplicates of each cell line for PDH3, mVEGF, GLUT1, PDK1. The mean values and statistical significance obtained by t-test analysis are shown with asterisks (*P value< 0,05 **P value<0,01 ***P value < 0,001). **(B)** $CYTb^{Ctrl}$, $CYTb^{S}$, $CYTb^{M}$ cells were cultured in hypoxic conditions (Hx) 1% O_2 for 72h and in 1mM DMOG for 24h. Normoxic conditions (Nx) are in 21% O_2 The cell lysates were assayed in immunoblots that were probed with antibodies against: Hif1α as a positive control of hypoxic gene induction NDUFA4L2 and actin as a loading control. **(C)** $CYTb^{Ctrl}$ and $CYTb^{S}$ cytoplasmic and mitochondrial fractions. Actin as a positive control for cytoplasmic localization and Tim23 as positive control for mitochondrial localization.

NDUFA4L2 and NDUFA4 Homology

NDUFA4L2 has 70% sequence homology with NDUFA4, and this evidence could result in an antibody cross-reaction for the two proteins. Thus, if CYTb^S cells overexpress NDUFA4 and if the NDUFA4L2 antibody cross-reacts, then the reading would appear as an apparent rise of the NDUFA4L2 protein in normoxia.

We investigated this hypothesis by SDS-PAGE of digitonin-treated mitochondria followed by consecutive immunodetection using the antibodies against NDUFA4 and NDUFA4L2 (Figure 62). At shown, both proteins were sufficiently different in size to be resolved by the SDS-PAGE gel. Thus, NDUFA4 antibody detected a single and lower molecular weight band in normoxic conditions in the three cell lines (Figure 62A), which corresponds with NDUFA4.

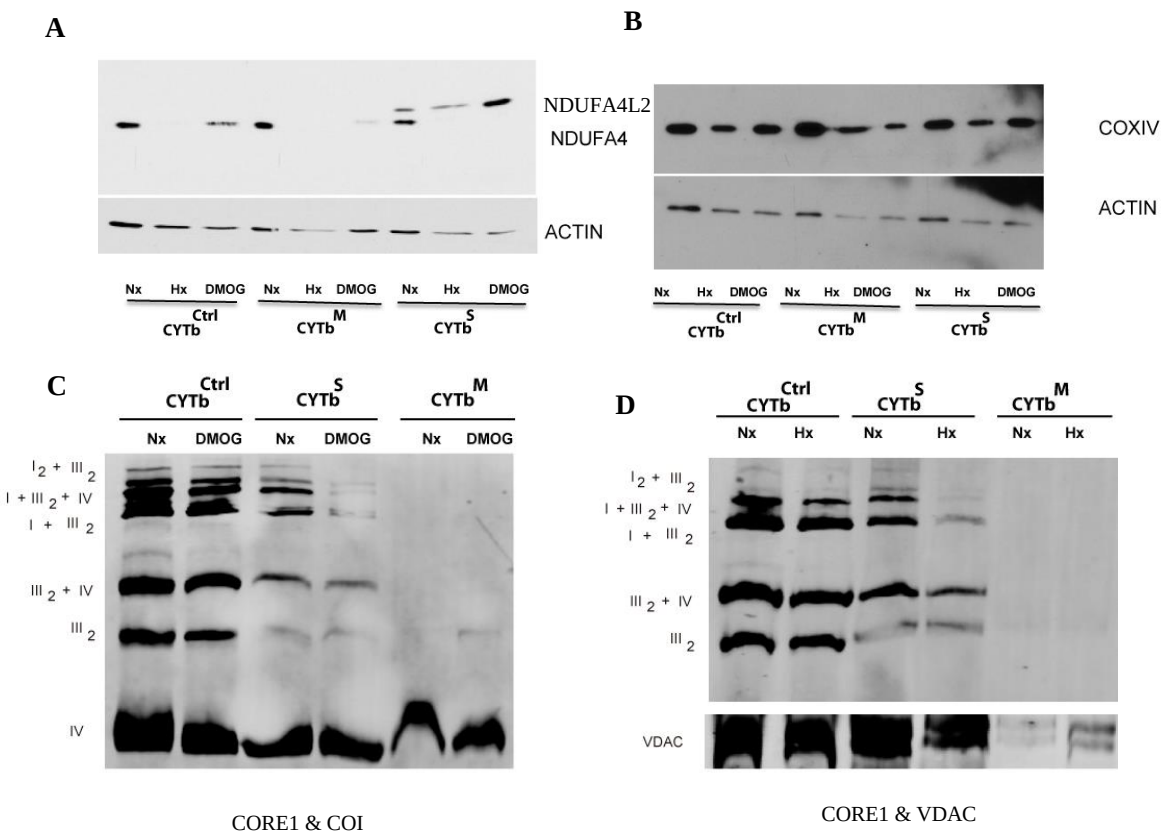

Figure 62. NDUFA4L vs. NDUFA4 and complex III stabilization. (A, B) cell lysates assayed in immunoblots that were probed with antibodies against **(A)** NDUFA4L2 and NDUFA4 **(B)** Subunit IV from complex IV. Actin was used as loading control. **(C, D)** BNGE and western blot of mitochondria solubilized by digitonine of the indicated cell line grown under **(C)** DMOG 1mM for 24 h and probed against complex III (UQCRC2) and COI, or **(D)** hypoxia, 1% O_2 for 72h and probed against CORE1 and VDAC as loading control.

On the other hand, NDUFA4L2 antibody also detected a second band of lower molecular weight under normoxia (NDUFA4) in all cell lines. Only in CYTb^M cells both NDUFA4 and NDUFA4L2 are co-expressed. When cells are switched to hypoxia, theNDUFA4 protein is dramatically downregulated in the three cell lines, as it happened in the presence of DMOG, with a parallel reduction of the overall complex IV content (Figure 62A&B). This result confirms previous observations from our group (Balsa *et al.*, 2012). As expected, hypoxia and DMOG also induce the expression of NDUFA4L2, in

control and mutated cells but have little impact in $CYTb^S$ cells, which already express NDUFA4L2 in normoxia.

Our group recently demonstrated that NDUFA4 is the 14th subunit of complex IV (Balsa *et al.*, 2012) and unpublished results of our group suggest that NDUFA4L2 may replace NDUFA4 under hypoxia (Oscar Yang Li, personal communication on his PhD work). If this is the case, the suppressor cells will have two types of complex IV. If this represents a component of the suppressor phenotype or is just parallel and independent phenomenon needs to be clarify.

Then we induced the overexpression of NDUF4AL in $CYTb^M$ cells under normoxia using DMOG (Figure 52C) or by culturing them under 1 % of O_2 (Figure 62D) and tested if this induction was enough to restore the assembly of CIII in $CYTb^M$. As shown the induction of the expression of NDUF4L was insufficient to induce the stabilization of complex III in mutant cells. Moreover, the stabilization of Hif1a reduced the number of respiratory complexes in control and suppressor cells.

II.4 Mitochondrial proteostasis

The missense mutation causing the amino acid at the E373 residue in the cyt b of mutant cells, affects the proper folding of the protein. Since CYTb is the only CIII protein encoded and synthesized in mitochondria and is required for the early steps of the assembly of the holocomplex, the misfolding might have two concomitant consequences, the accumulation of misfolded and unassembled proteins in the mitochondria. Therefore, genes involved in the role of efficient mitochondrial protein folding and thier interplay in complex assembly might be involved in the suppressor mechanism. We hypothesize that the mutation may induce a mtUPR response to account for the predicted stress and that the suppressor cells may have mitigated this response to allow the assembling of a certain amount of CIII with the mutant CYTb.

RNAseq analysis did not confirm our hypothesis since no significant changes were found in the expression of the mitochondrial proteases and chaperones. However, quantitative PCR suggested that both mutant and suppressor cells have increased mRNA expression for a number of mitochondrial proteases (AFG3L1, AFG3L2, YME1L1, PARL, SPG7, LONP, CLPX, CLPp, Htra2) and chaperones (HSP60, HSPA9) with respect to control cells (Figure 63 A-C). In contrast with our hypothesis, this overexpression is consistently higher in the $CYTb^S$ compared with $CYTb^M$ cells. To clarify the discrepancy between the RNAseq and the qPCR data and determine if the three cell lines have different mtUPR, we performed WB estimation of the protein levels for a subset of proteases and chaperones (LONP, YMA1L1, HTRA2, HSP70, HSP60). We could not observe any difference between control, suppresor and mutant cells at the protein level (Figure 64 A-B).

Despite that, we found no evidences of altered mtUPR, additional regulation of its activity could be achieved by mechansims indepenent of protein abundacy. Therefore, we performed the downregulation of 4 different mitochondrial proteases (YME1L1, Htra2/Omi, Lonp, ClpP) by interference in the $CYTb^M$ cells to inquire whether there could be the assembly of CIII with the mutant CYTb.

Lonp and ClpP are both AAA proteases required for organism development. Lon targets oxidatively modified proteins and ClpP is required for the degradation of misfolded proteins. In the inter membrane space the protease Htra2/Omi, a homo-trimeric serine protease, has a fundamental role in proteostasis and degradation of aberrant proteins.

Inner Membrane protein quality control is monitored by two AAA proteolytic complexes, namely YME1L1 (i-AAA) and AFG3L2 (m-AAA). The exposed hydrophobic stretches of unfolded polypeptide chains are recognize and gives the ability to distinguish correctly folded and assembled proteins form misfolded subunits (Baker and Haynes, 2011).

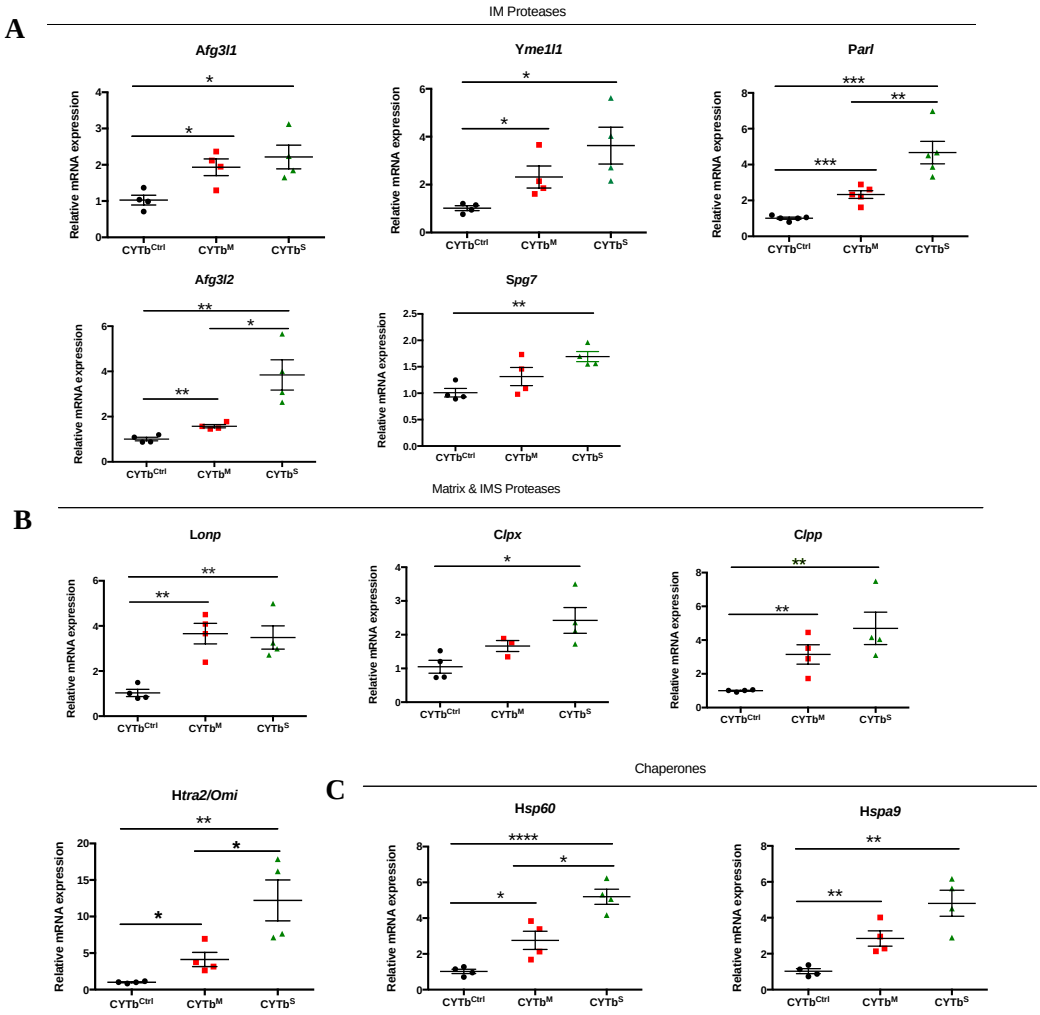

Figure 63. UPR response genes validation by q-PCR. Analysis of the cuadruplicates of each cell line for **(A)** Inner membrane proteases: AFG3L1, AFG3L2, YME1L1, SPG7, PARL **(B)** Matrix proteases: LonP, ClPp, ClPx and Inter membrane space Htra2/Omi and **(C)** Chaperones HSP60 and HSPA9. Standarization with Actin and relativized to the CYTb ^{Ctrl}. The mean values and statistical significance obtained by t-test analysis are shown with asterisks (*P value< 0,05 **P value<0.01 ***P value < 0.001 ****P value < 0.0001).

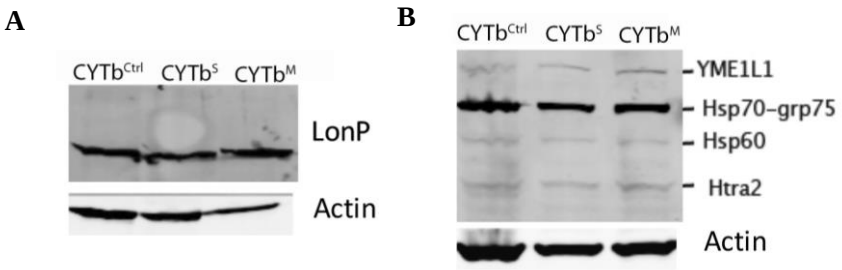

Figure 64. Proteases expression Level. (A) Western Blot analysis of LonP protein expression in the three cell lines used in this work. Actin as loading control. **(B)** Western Blot analysis of YME1L1, Hsp70, Hsp60 and Htra2, protein expression in the three cell lines used in this work. Actin as loading control.

By q-RT-PCR we validated the efficient reduction of the targeted mRNA by the interference in $CYTb^{M}$ cells. We observed basal levels for the isogenic control $CYTb^{Ctrl}$ and higher levels for $CYTb^{S}$ cells. mRNA levels for the $CYTb^{M}$ that have the knock down gene were lower than the non-treated $CYTb^{M}$ for YME1L1, Htra2/Omi and Lon, but for ClpP the interference did not affect the mRNA levels (Figure 65A-D).

Importantly, Blue-Native gel electrophoresis of all the $CYTb^{M}$ lines that were interfered and for the positive controls $CYTb^{Ctrl}$ and $CYTb^{S}$, revealed that the all interfered $CYTb^{M}$ cells reassemble complex III regardless of the efficiency of the interference (Figure 66A-D).

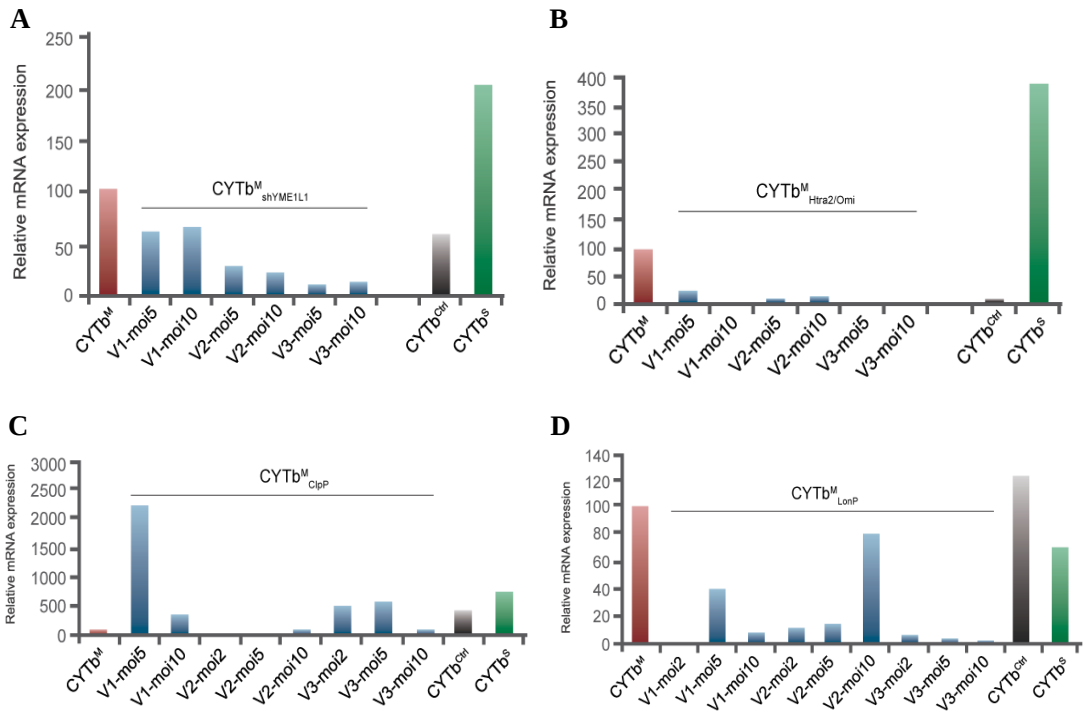

Figure 65. q-RT-PCR analysis of the mRNA levels in the treated cells with shRNA against each of the proteases **(A)** YME1L1 **(B)** Htra2/Omi **(C)** ClpP **(D)** LonP. $CYTb^{Ctrl}$, $CYTb^{S}$ and $CYTb^{M}$ without shRNA where used as controls. 2(ΔΔCT) is represented in the Y-axis and the cells for each interference are represented in the X-axis, normalized with actin.

These observations seemed to support our hypothesis proposing that a reduction in the mtUPR may allow the partial assembly of mutant CIII. However, the fact that this phenomenon was equally triggered regardless the identity of interfered protease was unexpected. Moreover, the assembly pattern obtained with the empty vector in the mutant cells may suggest that it was the viral infection rather than the nature of the protein interfered the factor that trigger the assembly of CIII with the mutant CYTb in the mutant cells. Recent literature had shown that viral infection trigger ER stress and the ER unfolded protein response, as homeostatic cellular response infections. This raises the possibility that endoplasmic reticulum stress response could regulate the assembly of complexes III in the mutant cells.

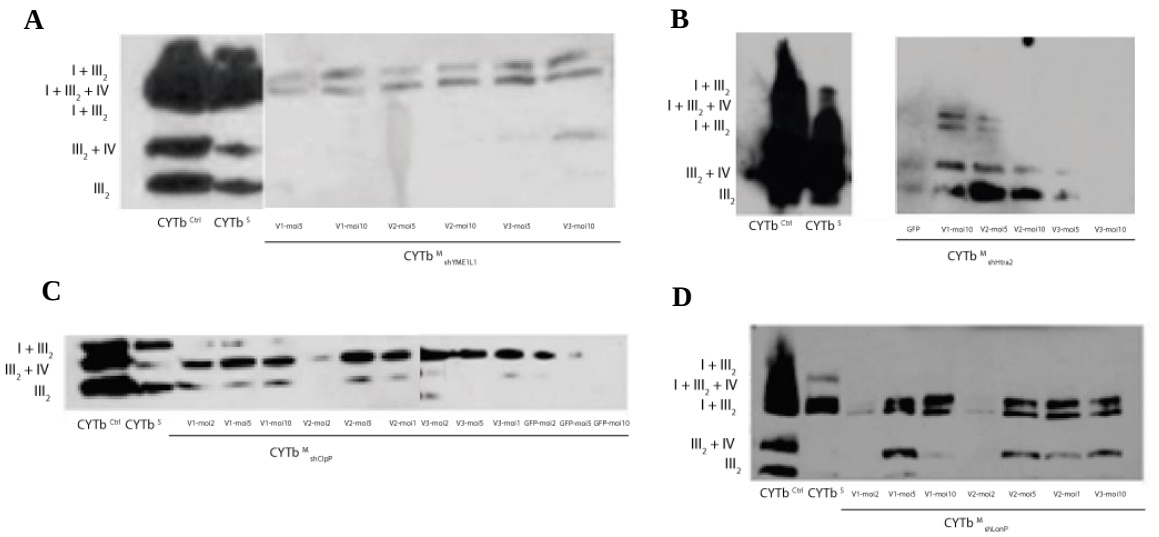

Figure 66. **Detection of the respiratory complexes and potential supercomplexes**, obtained with Digitonin after BNGE by western blot using specific antibodies against complex III (UQCRC2). CYTb^{M}cell line with shRNA against (A)YME1L1 protease. **(B)** Htra2/Omi protease **(C)** ClpP protease and the shGFP **(D)** LonP protease. Each number represent different moi of each of the shRNA delivered in different viral vectors.

II.5 Endoplasmic reticulum stress, UPR and Mitophagy regulation

CYTb^{M} cells are unable to assembly a functional CIII. The protease activity in mutant cells may prevent, under permissive growth condition, the excessive accumulation of unassembled CIII proteins in the mitochondria, to prevent the transference of the proteostasis stress outside the mitochondria and, in that way, avoid a chronic ER stress. However, the selective medium that allows the isolation of the suppressor cells, galactose instead glucose, strongly activates the mitochondrial biogenesis and the synthesis of OXPHOS proteins. The overproduced unassembled CIII proteins might overwhelm the capacity of the proteostatic response and fail to prevent its contention within the organelle. As a consequence, endoplasmic reticulum (ER) stress and a strong cellular UPR response and the regulation of the degradation of mitochondria by autophagy would be triggered. We hypothesized that this response should be required for the expression of the suppressor phenotype.

II.5.1 Autophagy induction

We inquired whether the autophagy status is modified in CYTb^{S} and CYTb^{M} cell lines. First, the RNAseq analysis showed that the genes involved in MTORC1 inhibition (as ATF4, SESN2, DDIT3 and TRIB3) were upregulated in the CYTb^{M} cells (Figure 67A). Strikingly, AKT1, an mTOR activator, and the ribosomal protein S6 kinase (S6K) levels, a downstream component of the mTOR signaling pathway, were strongly decreased (Figure 67B). Interestingly, CYTb^{S} cells restored both AKT and S6K protein levels to normal. This evidence suggested that autophagy might be strongly down-regulated in CYTb^{S} cells. In fact, ATG7 and Beclin, two proteins required for the assembly of early autophagosomes were also significantly reduced in CYTb^{M} cells and overexpressed in CYTb^{S} cells (Figure 67B).

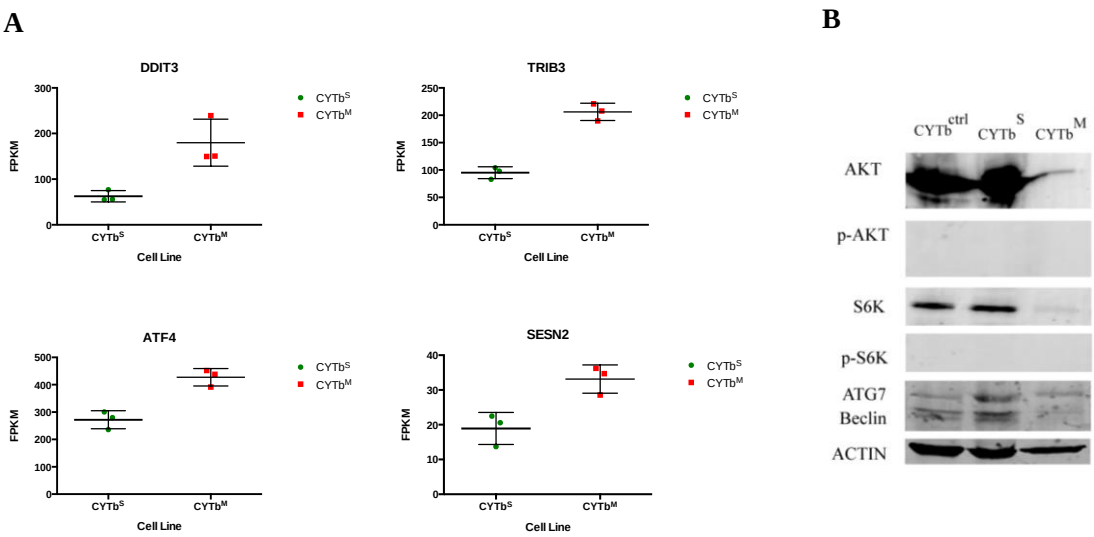

Figure 67. Autofagy induction relationship with mTOR inhibition. (A) FPKM triplicates representation for each gene in both CYTb^{S} and CYTb ^{M} cell lines, obtained after RNAseq. The studied genes were DDIT3, TRIB3, ATF4 and SESN2. **(B)** Immunoblot analysis of autophagic proteins, AKT, S6K and both phosphorilated isoforms, ATG7 and Beclin. Actin is used as loading control.

During autophagy, the cytoplasmic form of LC3 (LC3-I) is processed and recruited to the autophagosomes, where LC3 II is generated by proteolysis and accumulated. The conversion of LC3I to LC3II serves as a marker of autophagy activity. LC3 western-blot allows the determination of LC3-II/LC3-I proportion. We estimated this parameter to determine whether the autophagic activity differs between suppressor and mutant cells. Interestingly, an accumulation of autophagy marker LC3-II was detected in CYTB^{M} cells (Figure 68A).

This observation might suggest that autophagy was stalled in CYTB^{M} cells. Therefore, we monitored the endogenous GFP-LC3 by fluorescence microscopy (Figure 68B).

As shown, LC3 appeared mainly as a diffuse cytoplasmic pool in CYTb^{Ctrl} and CYTb^{S} cells, with few punctate structures that were identified as autophagosomes. The relative amounts of diffuse and punctuated forms suggested an active and normal flux of autophagy in control CYTb^{Ctrl} and CYTb^{S} cells. The slightly higher content of autophagosomes in CYTb^{S} cells may indicate a more active autophagy. On the contrary, the determination of the endogenous GFP-LC3 revealed an abnormal amount of foci in the CYTB^{M} cell line, suggestive again of a stalled autophagy (Figure 68C). However, we cannot discarded the possibility that a hyperactive autophagy activity would be responsible of this phenotype.

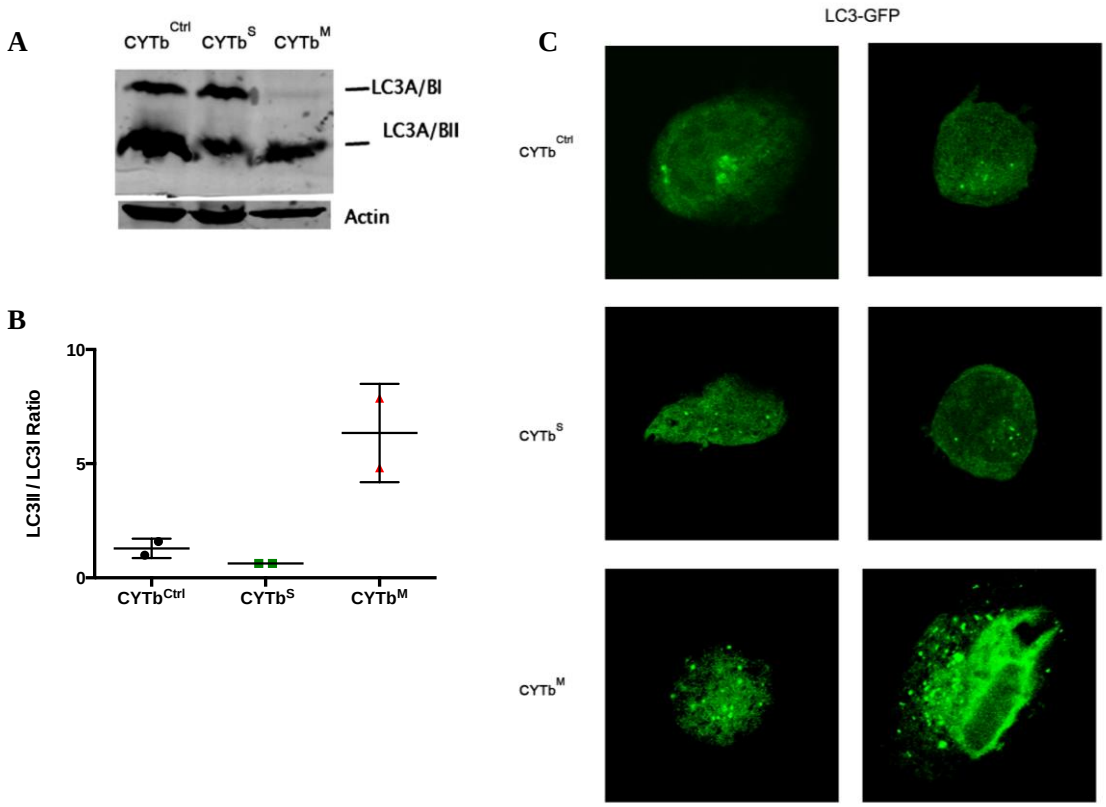

Figure 68. LC3 conversion. (A) Lc3 is detected in both cell lines by Western Blot, tracking the conversion of LC3-I to LC3-II as an indicative of autophagic activity. **(B)** GFP-LC3 puncta formation assays by fluorescent microscopy. Cells in culture stably expressing GFP-LC3, $CYTb^{M}$ showed an increase in GFP-LC3 puncta number, that primarily represent autophagosomes.

One of the primary methods currently applied to measure the autophagy flux is the monitoring of LC3 turnover. Chloroquine is known as one most common lysosomal inhibitors. We used DAPI nuclei staining to find an optimal concentration of chloroquine that did not affect $CYTb^{M}$ cell viability. The DAPI analysis on cells treated with chloroquine 20 µg/ml for 24-hours and 4-hour incubation periods, showed that cell viability was time and dosage dependent ($p < 0.05$, $n = 6$) (Figure 69A-D).

Chloriquine is a lysosomotropic reagent that inhibits autophagosome-lysosome fusion. In the presence of this drug the degradation of LC3-II is blocked, resulting in the accumulation of LC3-II. Treatment of $CYTb^{M}$ cells with chloroquine for 24h did not substantially affect the proportion of LC3-II, indicating that in basal conditions autophagy was already stalled in these cells (Figure 70A). To undoubtedly distinguish whether hyperactive or a stalled mitophagy could be responsible for the impossibility of $CYTb^{M}$ cells to assemble complex III, we performed BNGE of digitonin-treated mitochondria of chloroquine treated $CYTb^{M}$ cells, followed by immunodetection against complex III protein CORE1. As shown, chloroquine treated $CYTb^{M}$ cells did not restore CIII assembly capacity (Figure 70B).

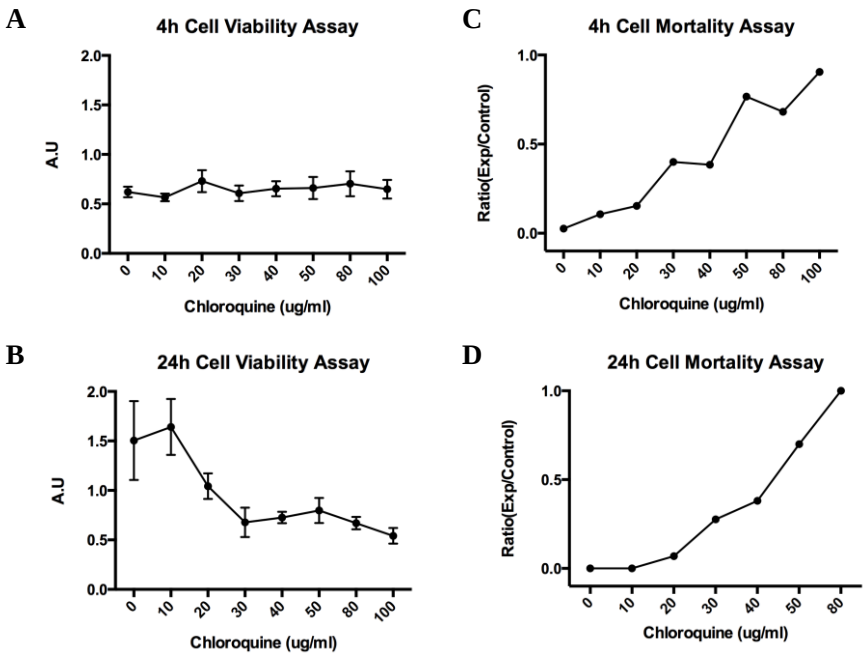

Figure 69. Cell Viability Assay. (A-B) Viavility assay shows chloroquine toxicity is both time and dose dependent for 4h and 24 h. Chloroquine concentrations of 10-30 μg/ml ($p < 0.05$) do not significantly affect cell viability at different times **(C-D)** Mortality Assay at 4h and 24h time of administration between control cell line $CYTb^{Ctrl}$and $CYTb^{M}$, shows that the optimal concentration after which cells became non-viable is 20 μg/ml.

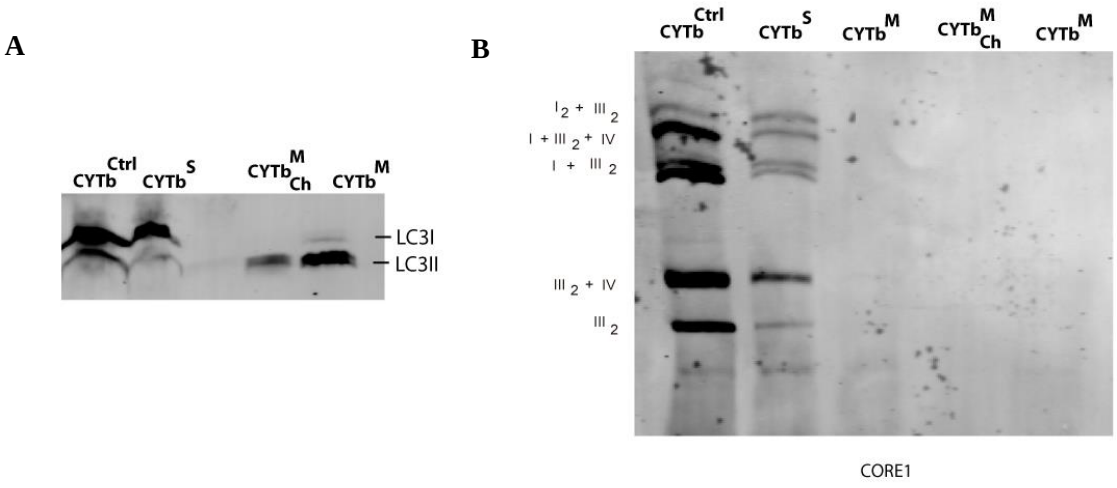

Figure 70. LC3 Turnover Assay with chloroquine treatment 20 μg/ml in $CYTb^{M}$ (A) Lc3 is detected in both cell lines by Western Blot, tracking the conversion of LC3-I to LC3-II . Accumulation of LC3-II is observed in $CYTb^{M}$ cells treated with the drug. **(B)** Detection of complexes and SC in the mitochondria solubilized with digitonin by BN-PAGE for CIII (anti-CORE1).

II.5.2 ER & Nutrient stress in promoting assembly of RCs

We hypothesized that regulation of the ER stress pathway is required for the expression of the suppressor phenotype. Therefore, we used low doses of tunicamycin to block protein glycosylation and trigger ER stress when growing the cells under glucose.

We observed that tunicamycin did not induce the suppressor phenotype in CYTb^{M} cells. However, we noticed a significant increase of the amount of CIV monomer and dimer and a novel CIV band co-migrating with supercomplex III_2+IV, but not containing CIII (Figure 71A). Therefore, the sole activation of ER stress was insufficient to trigger the suppressor phenotype.

The UPR signaling pathway occurs with multiple mechanisms, and it is triggered by three ER membrane-associated sensors, namely ATF6, IRE1 and PERK. These factors initiate an adaptive response to maintain protein folding and ER activity. PERK activation induces the phosphorylation of the eIF2α translation factor to initiate its action. We found that the phosphorylation of the Eukaryotic Initiation Factor 2 alpha (eIF2α) was strongly reduced in the suppressor cells (Figure 71B). To evaluate whether the inhibition of the PERK arm of the ER stress response is necessary to induce the suppressor phenotype we took advantage of the inhibitors of PERK activity (GSK2606414). Thus, induction of ER stress by tunicamycin with simultaneous inhibition of PERK was able to induce the suppressor phenotype (Figure 71C).

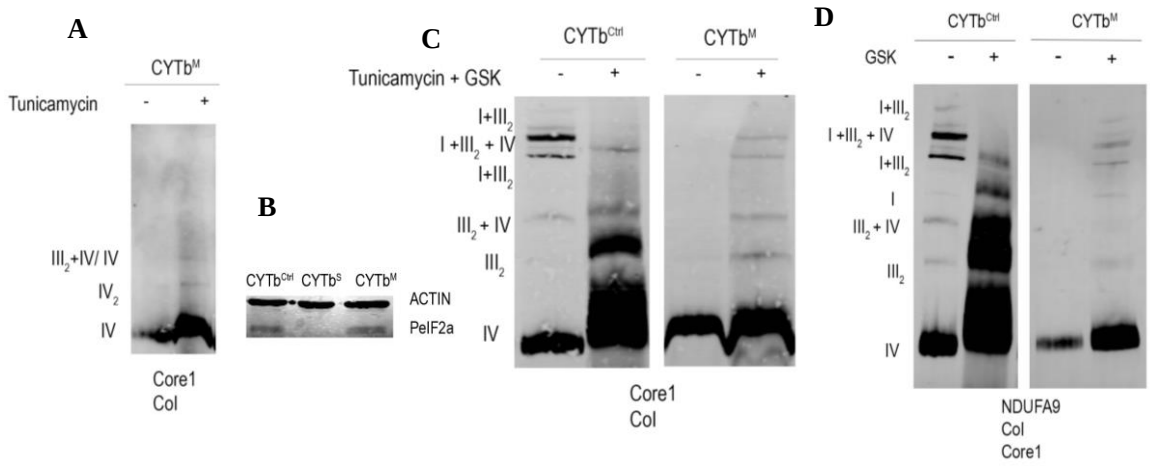

Figure 71. Respiratory complexes assembly in ER stress activation with Tunicamycin and PERK inhibition. (A) Tunicamicin (20nM) administration in CYTb^{M} in glucose medium with uridine. **(B)** Total protein content for the three cell lines used in this work against PeIF2a. Actin as loading control. **(C)** PERK inhibitor (GSK2606414 - 1µm) and Tunicamicin (20nM) administration in CYTb^{Ctrl} glucose medium and CYTb^{M} in glucose medium with uridine. Mitochondria was solubilized with digitonin for BN-PAGE and probed against CIII (anti-CORE1) and CIV (anti-COI) **(D)** PERK inhibitor (GSK2606414 1µm) administration in CYTb^{Ctrl} glucose medium, CYTb^{S} glucose medium CYTb^{M} in glucose medium with uridine. Mitochondria was solubilized with digitonin for BN-PAGE and probed against CI (NDUFA9), CIII (anti-CORE1) and CIV (anti-COI).

Moreover, the inhibition of PERK activity was sufficient to induce the reassembly of CIII and the suppressor phenotype (Figure 71D)., The reassembly however was less efficient, since the assembly of CIII and CIII + CIV was not complete, as shown in Figure 71C. These results suggest a particular activation mechanism of ER stress in which PERK should not be activated is responsible for the suppressor phenotype.

Finally, we also tested the effect of PERK activation in basal conditions in our cell lines. Administration of the PERK activator to CYTb^{M} cells maintained in glucose medium increased the assembly of CIV in its monomer and dimer forms as it did Tunicamycin. However, activation of PERK failed to induce the assembly of CIII (Figure 72A). In agreement with that, PERK activation failed to promote survival of CYTb^{M} cells in galactose medium (Figure 72B).

We also noticed that as under tunicamycin treatment, a novel, high molecular band containing CIV but lacking CIII could be detected, the nature of which was not further investigated. Surprisingly, PERK activation recovered the original phenotype of CYTb^{M} cells with respect to CI, enhancing again its degradation in the absence of CIII and suggesting that the progressive adaptation to the proteostatic stress in the CYTb^{M} cells over the years of continuous cultures involves the attenuation of the PERK ER-stress (Figure 72A). This unexpected observation may explain some apparent discrepancy on the relevance of the ablation of CIII in the stability of CI.

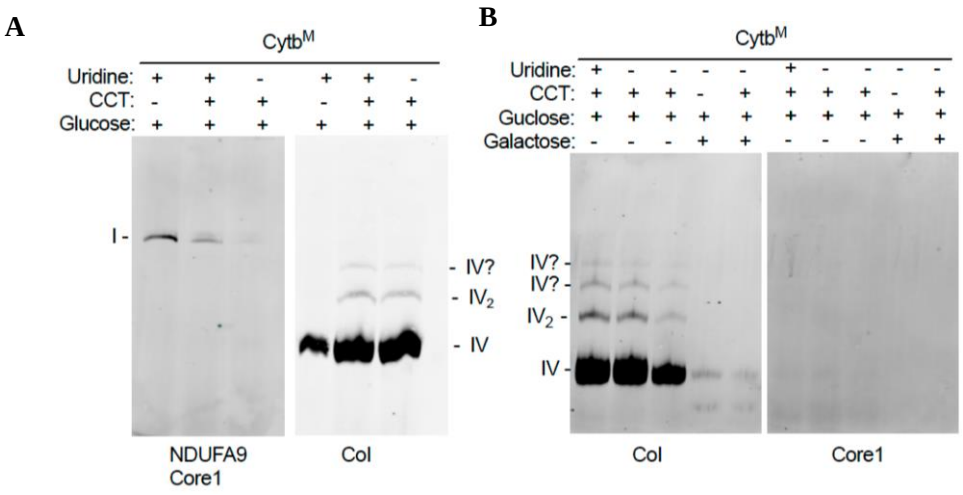

Figure 72. CYTb^{M} respiratory complexes assembly in ER stress activation (A) PERK activator (CCT020312 1µm) administration in CYTb^{M} in glucose medium with or without uridine. Mitochondria was solubilized with digitonin for BN-PAGE and probed against CI (NDUFA9), CIII (anti-CORE1) and CIV (anti-COI). **(B)** The effect of sugar source (glucose and galactose) with the use of the activator CCT020312 in the mitochondria solubilized with digitonin by BN-PAGE for CIII (anti-CORE1) and CIV (anti-COI) in the CYTb^{M} cells line.

DISCUSSION

I. NOVEL *IN SITU* VALIDATION OF THE PLASTICITY MODEL

Mitochondria are organelles that reside in eukaryotic cells. Their main role is providing the cell with the energy requirements in the form of ATP through the oxidative phosphorylation system (OXPHOS) (Acin-Perez and Enriquez, 2014).

An unsolved question in mitochondrial research is the distribution in situ of protein complexes and their interactions. Revealing the *in situ* distributions of the OXPHOS components would definitely contribute to explain the structural organization of the mETC.

Different models have been proposed for the structural organization of the mETC, the solid state (B Chance *et al.*, 1955), the random collision (Hackenbrock, Chazotte and Gupte, 1986) and the plasticity (Acín-Pérez *et al.*, 2008) models.

The plasticity model proposes that complexes I, III and IV can act free or super-assembled in supramolecular structures (supercomplexes) as $I_n + III_n$, $III_2 + IV_1$ or $I + III_2 + IV_1$ (Respirasome) (Acin-Perez et al al. 2008; Enriquez 2016). Other associations containing multiple copies of complex IV and the interaction of complex I with complex IV have been also suggested. The formation of supercomplexes is necessary to maintain the stability of their individual components, therefore there is a structural interdependence among the complexes of the respiratory chain.

On one hand, the existence of the mitochondrial respiratory supercomplexes has been documented by detergent disruption of mitochondrial membranes followed by BNGE (Schägger and Pfeiffer, 2000; Acín-Pérez *et al.*, 2008). However, the type or the amount of different detergents can influence the size of the generated micelles, which as a consequence, can lead to contradictory results. Moreover, the identification can be done by density gradients (Acín-Pérez et al., 2008; Dudkina et al., 2005) followed by proteomic analysis (Heide *et al.*, 2012) or cryo-electron microscopy (Dudkina et al., 2005). Nevertheless, the latter approaches still do not allow localization of complexes *in situ*. Electron tomography can be used for imaging intact membranes at a high resolution (Gan *et al.*, 2012), but still no detailed information is available for SCs within lipid bilayers.

On the other hand, *in situ* visualization has suffered of the intrinsic limitations of electron microscopy imaging (no multiple staining) and of the low resolution of fluorescent microscopy. The era of super-resolution microscopy has emerged with new possibilities for studying the mitochondria localization of proteins. As an example, the PINK1 protein was found to co-localizes with CI at the inner mitochondrial membrane when the organelle is energized, as demonstrated by FPALM and TALM single molecule localization microscopy (Beinlich *et al.*, 2015). The discrimination between outer and inner mitochondrial membranes was reached by single molecule localization and tracking (Appelhans *et al.*, 2012). Mitochondrial inner membrane proteins were studied for MINOS clusters in human cell lines, revealing the co-localization of the subunits mitofilin, MINOS1 and CHCHD3 in the cristae junctions (Jans *et al.*, 2013).

For our multicolor *in situ* studies we have chosen to apply STED microscopy, which is one of the super-resolution approaches developed to bypass the diffraction limit of light microscopy and increase resolution.

STED super-resolution microscopy was used to investigate the assembly status of different OXPHOS deficient cell lines as negative controls in parallel with their endogenous control cell lines. For that we used different immunostaining combinations of mitochondrial endogenous proteins.

It has been shown that mutations in genes encoding subunits of the mitochondrial complexes may affect the stability of other complexes (Budde *et al.*, 2000; Ugalde *et al.*, 2004; Saada *et al.*, 2012). These subunits can potentially be stable as individual proteins, associated with others in assembled complex intermediates, or forming supramolecular structures. Therefore, a panel of genetically modified cells incapable of assembling one or more respiratory complexes, as probed in the BNGE, was used to compare the distribution and relative abundance of the subunits when mitochondrial function is altered.

The firsts parameters under consideration in this thesis were the selection of the optimal working photophysical conditions for each pair of control and mutant cell lines to minimize potential artifacts. We have taken precautions about excessive photobleaching along with optimization of the STED depletion (intensity, wavelength, and scan time) to reduce issues related to a high power illumination (Hotta *et al.*, 2010).

We have carefully determined the increase in resolution in the STED images along the three axes by calibrating with GATTAquant nano-beads for each fluorophore. Because the STED photophysics strictly depends on the fluorophore nature, we obtained an average of 126nm x,y,z axial resolution (that is 3 to 8 fold better than confocal imaging). It is worth noticing the good agreement between the resolution obtained in this study and the size of the mitochondria nuclei (Kukat *et al.*, 2015).

In this thesis we developed a new methodology that provides a robust tool to determine the presence of respiratory complexes and supercomplexes *in situ*.

We found that in this OXPHOS deficient cells, the endogenous distribution of the mitochondrial subunits was either detectable, decreased or just negligible, depending on the phenotype of each cell line, as expected and in agreement with the relative abundance by total protein in SDS gels.

We co- immunolabelled different mitochondria subunits combinations as the ones detected in a BNGE. Each combination was analyzed as % of co-localization. These experiments provided valuable information about the co-existence and co-localization of the pair subunits. Therefore, we could establish that a high degree of co-occurrence between complexes exists in individual cells, confirming the presence of supercomplexes.

Furthermore, we performed triple immunostaining STED analysis. The high degree of co-occurrence between CI, CIII and CIV confirms the existence of the respirasome. The proximity found between the selected subunits correlated with the results obtained when using permeabilized digitonin cells in BNGE. One puzzling observation was the close proximity between complex I and complex IV. This interaction is not observed in digitonin-permeabilized samples run in BNGE. However, recent publications have opened a new debate about existence of CI-CIV supercomplexes. In this work we confirm by double and triple immunostaining, the presence of supercomplexes containing CI and CIV, validating the worked proposed by Müller et al. (Müller *et al.*, 2016).

The structural analysis of 3 color STED images, evidenced the different degree of distribution and presence of the various forms of mitochondrial associations. In this way, we found that CI and CIII were equally detected in BNGE and immunostaining. However, CIV was found less in immunostaining than in BNGE, likely due to the different sensitivities of the anti-CIV Ab in the two techniques. This observation was in fact reproduced in the other two cell lines. CIV was imaged with an Alexa488-labelled Ab following the depletion sequence 568→532→488nm that could not be changed because of the intrinsic photophysical properties of the fluorophores. Therefore, in addition to the constrains we needed to apply for minimizing photobleaching, the 488nm label was always imaged as the last, being also the Ab with the lowest efficiency under depletion conditions.

Finally, to overcome the limitations of 2D-imaging we approached a partial volume reconstruction of the mitochondrial complexes *in situ.* Accordingly, we aimed at exploring a cellular volume of about 500nm depth along the mitochondrial network.

We have found that to achieve that level of (x,y,z)-STED images, we could not follow the previous protocols of depletion, which were successfully applied in Results I.8.1. This was due to the necessity of obtaining z-optical sections smaller than 100nm. Because of that, we have set up an innovative approach based on resonant scanning at 8000frames per second of each fluorophore during depletion at 660nm. The results of this strategy were impressive in revealing that in a single cell, the relative abundance along depth of ≈500nm was very similar to what it is found by a BNGE run on permeabilized digitonin cell large populations.

The 3D STED volume reconstruction provides the first experimental evidence of specific details and quantification of each combination of SCs and individual complexes as observed in the BNGE probed against the same mitochondrial subunits.

Entirely new possibilities for mitochondrial research are open up by this work. New methods for data analysis were developed to fit the criteria of this project, which can be applied in further investigations.

To further exploit the full resolution potential of our approach, new labeling tools such as Fabs and nanobodies will be required.

In conclusion, we designed an experimental methodology able to directly visualize the nanoscale details of the respiratory SCs in intact cells. Our observations support the notion that free RCs and SCs co-exist simultaneously in the same single cell.

Here we have shown that super-resolution imaging can be used to determine very close proximity of mitochondria inner membrane proteins, strongly suggesting direct association. The *in situ* results and the BNGE analysis return the same qualitative and quantitative information about RCs distribution and assembly.

To the best of our knowledge, this is the first study that has obtained superresolved images on endogenous mitochondrial proteins, providing conclusive demonstration of the plasticity model for the organization of the electron transport chain (Acín-Pérez *et al.*, 2008; Acin-perez and Enriquez, 2014; Enríquez, 2016b).

II. COMPENSATORY PATHWAYS FOR OXPHOS DEFICIENCY

Mitochondrial function and dysfunction contribute to different fundamental aspects in biomedical research. Currently mitochondria have a recognized role in cellular homeostasis. The oxidative phosphorylation system (OXPHOS) in fact, being the main source of energy in most cell types, controls the redox state of the cell as well as the cellular metablism and it participates in signaling pathways that range from the synthesis of pyrimidines to the regulation of apoptosis.

Mitochondrial diseases are characterized by heterogeneous genetic pathologies, the only common aspect is the dysfunction in the oxidative phosphorylation system (OXPHOS). The various functions performed by this organelle in the cell include the supply of energy in the form of ATP through oxidative phosphorylation, the regulation of Ca2 + homeostasis and of the levels of oxygen free radicals (ROS), the regulation of the apoptosis and the synthesis of pyrimidine nucleotides for cellular redox regulation (NAD + / NADH). The biogenesis of the oxidative phosphorylation system depends on both the mitochondrial and nuclear genomes, so that different mitochondrial myopathies can be due to mutations in either genome. The diseases are usually multisystemic, and predominantly affect tissues with high energy demand (skeletal muscle, heart, brain ...).

The wide variety of mitochondrial diseases that are known at the present carry a high socio-health importance. In addition to these types of pathologies, mitochondrial involvement in other diseases such as Parkinson's or cancer and their relevant role have been demonstrated. The therapeutic advance against mitochondrial diseases has been interrupted due to the lack of adequate experimental models that can represent the exact characteristics of the pathologies, as well as the lack of an accurate molecular diagnosis.

The number of genetic defects that affect the system of oxidative phosphorylation in humans is an important source of information. These defects are characterized in the genes and in the nuclear and mitochondrial DNA. Many mutations in the genes of OXPHOS system that cause diseases result in variable phenotypic manifestations.

Alterations in the association of complexes I + III can only be found when the genetic defects are found in complex III (ubiquinol cytochrome c reductase). Similarly, genetic alterations of mitochondrial DNA that encode complex I genes only cause a deficiency of the isolated complex and have never been associated with the combined I + III complex (DiMauro and Schon, 2003). The only case in which a partial reduction of the complex III and the total loss of the activity of the complex I have been observed wasn associated with mutations in the nuclear NDUFS4 complex I gene (Budde et al., 2000). Most of the genetic defects of complexes III characterized to date are due to mutations in cytochrome b (Andreu et al, 1998, 1999, Keightley et al, 2000; Lamantea et al, 2002), the only gene encoded by mitochondrial DNA, fundamental for the assembly of this complex (di Rago et al, 1993, Sidhu and Beattie, 1983).

Mitochondrial myopathies affect different organs and are associated with mutations in mitochondrial DNA. The term of mitochondrial encephalomyopathies refers to a heterogeneous group of clinical symptoms due to defects in the mitochondrial respiratory chain. At present, a sporadic form of mitochondrial myopathy is known in which exercise intolerance is a predominant symptom. The biochemical and molecular bases of the pathology is still unknown.

After the sequencing of the cytochrome b oxidase gene, being evidence of Complex III deficiency, different mutations were found in several patients, such as nonsense mutations (G15084A, G15168A and G15723A), missense mutations (G14846A) and deletions of 24 base pairs (nucleotides 15498 and

15521). In these patients, clinical manifestations include progressive intolerance to exercise, joint weakness or different attacks of myoglobinuria.

As mentioned previously, our laboratory has developed mutated cell lines in the mtDNA(Bayona-Bafaluy *et al.*, 2008)The cells studied in this thesis belong to a mouse line carrying a missense mutation (15263 G>A) in the mitochondrial-encoded protein CYTb. Confirmation of the suppressor phenotype in the $CYTb^M$ cells and assembly of complex III in the $CYTb^S$ cells, allows us to investigate the specific characteristics of this phenotype. We found that as a consequence of the loss of CIII, CI is degraded, but after years in culture these cells became less efficient in degrading CI (Guarás *et al.*, 2016). We found that the CI degradation is connected with PERK activity and that failure in the elimination mechanism of the mutated CYTb in $CYTb^S$, results in the partial assembly of CIII.

In addition, we found that the suppressor cells have a defined program that induced a protection against apoptosis mediated by the overexpression of SERPINA3 (Chelbi *et al.*, 2012; Yang *et al.*, 2014); the triggering of a metabolic adaptation involving the ectopic expression of several Hif1α dependent genes but without stabilization of Hif1α, specially the CIV isoform NDUF4L (Tello *et al.*, 2011) (Balsa *et al.*, 2012). A third program that differentiated suppressor from mutant cells involves the ER stress response including mitophagy.

Our work led to propose a model for the suppressor phenotype. In mutant cells and under permissive growth conditions, the increase in the protease activity may prevent the excessive accumulation of unassembled CIII proteins in the mitochondria. This may allow the contention of the proteostatic stress within mitochondria but at the cost of collapsing the autophagy flux by the excess of damaged mitochondria.

Under non-permissive conditions (galactose) the energetic stress triggers the biogenesis of mitochondrial OXPHOS and the increase in the proteostatic mitochondrial stress, overwhelming the capacity of the mitochondrial proteases. Thus, the turnover of the mutant cty b protein may be reduced, allowing its forced folding. Then the mutant cty b protein can be assembled into complex III that, since the mutation does not affect the catalytic centers, would be functional.

In addition, overwhelming the capacity of the mitochondrial proteases would lead to the extension of the mtUPR to the rest of the cell, inducing ER-UPR response and ER-stress. ER stress enhances proteostatic response, folding capacity (chaperones) and autophagy flux. ER response is complex and it balances the activation of three different routes (PERK, ATF6, or IRE1 dependent).

The PERK route is responsible of minimizing UPR both in the ER and the mitochondria by attenuating the overall protein synthesis through the phosphorylation of the eIF2α, reducing de burden of proteins arriving to the ER and to the mitochondria. In addition, PERK activation promotes the synthesis of ER, mitochondrial chaperones and proteases by the ATF4/CHOP pathway, and reduces the mitochondrial protein import by specific modulation of the TIM17a protein (Rainbolt *et al.*, 2013). The actions triggered by PERK induce a reduction of mitochondrial biogenesis and simultaneously increase the proteostatic capacity of the organelle that prevents the assembly of complex III with the mutant CYTb.

Since mutant cells are unable to assemble CIII they die because cannot generate enough energy to survive in galactose medium. We found that triggering ER stress response but preventing PERK route activation is required to allow the assembly of CYTb mutant carrying CIII.

These conditions allow the overall increase of mitochondrial biogenesis and impose enough pressure on the proteostatic capacity of the mitochondria to allow the assembly of CIII. At the same time, the other branches of the ER response would enhance autophagy, restoring its flux.

Viral infections induce ER stress and autophagy as a consequence of the unbalance in protein synthesis due to the hijacking of the cellular protein synthesis apparatus (Sen, Balakrishnan and Jayandharan, 2014) and/or by the action of specific viroporines (Fung, Torres and Liu, 2015). The balance between the different ER stress branches may be influenced by the virus load or aggressiveness. We found that different virus preparations and load can induce the assembly of complex III in mutant cells with variable efficiency. We hypothesize that this variable efficiency depends on the proportion at which autophagy activation is maximized while PERK activation is minimized.

We sustain our model based on four major observations: 1) viral infection triggers the assembly of CIII in mutant cells; 2) PERK activation directly or overall ER stress activation by tunicamycin fails to promote the assembly of CIII in mutant cells; 3) tunicamycin + PERK inhibition triggers the assembly of CIII in mutant cells; 4) PERK activation prevents the survival of suppressor cells in galactose

CONCLUSIONS

- STED imaging demonstrates the co-existence of free and super assembled complexes *in situ.*

- Volume reconstructions by super-resolution STED microscopy provide the first experimental semi-quantitative evaluation of SCs and individual complexes without the use of any detergents, in agreement with the pattern observed by BNGE.

- The results from the different immunostaining experiments support the existence of CI + CIV assembly.

- Respiratory complexes distribution and heterogeneity *in situ* validate the plasticity model.

- ER-stress signaling and the assembly of respiratory complexes are intimately interconnected.

- PERK ER-stress pathway enhances quality control folding of complexes and SCs assembly.

- Regulation of PERK may be a therapeutic strategy to allow the assembly of functional RCs with missense mutations in mtDNA encoded subunits.

CONCLUSIONES

- Las imágenes STED demuestran la coexistencia de complejos libres y súper ensamblados in situ.

- Las reconstrucciones de volúmenes obtenidos por microscopía de superresolución proporcionan el primer enfoque semicuantitativo de la presencia sin el uso de detergentes de supercomplejos y complejos individuales, de acuerdo con lo observado por BNGE.

- Los resultados de las diferentes inmunodetecciones confirman la existencia del ensamblaje del CI + CIV.

- Las distribuciones de complejos respiratorios y la heterogeneidad in situ validan el modelo de plasticidad.

- La señalización ER-stress y el ensamblaje de complejos respiratorios están íntimamente interconectados.

- Las vías PERK ER-stress mejoran el plegado de control de calidad en el ensamblaje RC.

- La regulación de PERK puede ser una estrategia terapéutica para permitir el ensamblaje de CR funcionales con mutaciones sin sentido en subunidades codificadas de mtDNA.

BIBLIOGRAPHY

Abrahams, J. P., Leslie, A. G. W., Lutter, R. and Walker, J. E. (1994) 'Structure at 2.8 A resolution of F1-ATPase from bovine heart mitochondria', *Nature*, 370(6491), pp. 621–628.

Acín-Pérez, R., Bayona-Bafaluy, M. P., Fernández-Silva, P., Moreno-Loshuertos, R., Pérez-Martos, A., Bruno, C., Moraes, C. T. and Enríquez, J. a. (2004) 'Respiratory complex III is required to maintain complex I in mammalian mitochondria', *Molecular Cell*, 13(6), pp. 805–815.

Acin-perez, R. and Enriquez, J. A. (2014) 'Biochimica et Biophysica Acta The function of the respiratory supercomplexes : The plasticity model ☆☆', *BBA - Bioenergetics*. The Authors, 1837(4), pp. 444–450.

Acín-Pérez, R., Fernández-Silva, P., Peleato, M. L., Pérez-Martos, A. and Enriquez, J. A. (2008) 'Respiratory Active Mitochondrial Supercomplexes', *Molecular Cell*, 32(4), pp. 529–539.

Althoff, T., Mills, D. J., Popot, J.-L. and Kühlbrandt, W. (2011) 'Arrangement of electron transport chain components in bovine mitochondrial supercomplex I1III2IV1.', *The EMBO journal*, 30(22), pp. 4652–64.

Andreu, A. L., Checcarelli, N., Iwata, S., Shanske, S. and DiMauro, S. (2000) 'A missense mutation in the mitochondrial cytochrome b gene in a revisited case with histiocytoid cardiomyopathy.', *Pediatric research*. United States, 48(3), pp. 311–314.

Andreu, A. L., Hanna, M. G., Reichmann, H., Bruno, C., Penn, A. S., Tanji, K., Pallotti, F., Iwata, S., Bonilla, E., Lach, B., Morgan-Hughes, J., Shanske, S., Sue, C. M., Pulkes, T., Siddiqui, A., Clark, J. B., Land, J., Iwata, M., Schaefer, J. and DiMauro, S. (1999) 'Exercise Intolerance Due to Mutations in the Cytochrome b Gene of Mitochondrial DNA', *New England Journal of Medicine*. Massachusetts Medical Society, 341(14), pp. 1037–1044.

Aoyama, H., Tomizaki, T., Yamaguchi, H., Nakashima, R., Yaono, R. and Yoshikawa, S. (1995) 'The Whole Structure of the 13-Subunit Oxidized Cytochrome c Oxidase at 2.8 A', *Science*, 272(31), pp. 1136–1144.

Appelhans, T., Richter, C. P., Wilkens, V., Hess, S. T., Piehler, J. and Busch, K. B. (2012) 'Nanoscale organization of mitochondrial microcompartments revealed by combining tracking and localization microscopy', *Nano Letters*, 12(2), pp. 610–616.

Baker, B. M. and Haynes, C. M. (2011) 'Mitochondrial protein quality control during biogenesis and aging', *Trends in Biochemical Sciences*, 36(5), pp. 254–261.

Balsa, E., Marco, R., Perales-Clemente, E., Szklarczyk, R., Calvo, E., Landázuri, M. O. and Enríquez, J. A. (2012) 'NDUFA4 is a subunit of complex IV of the mammalian electron transport chain', *Cell Metabolism*, 16(3), pp. 378–386.

Baracca, A., Chiaradonna, F., Sgarbi, G., Solaini, G., Alberghina, L. and Lenaz, G.

(2010) ‘Mitochondrial Complex I decrease is responsible for bioenergetic dysfunction in K-ras transformed cells’, *Biochimica et Biophysica Acta - Bioenergetics*. Elsevier B.V., 1797(2), pp. 314–323.

Baradaran, R., Berrisford, J. M., Minhas, G. S. and Sazanov, L. a (2013) ‘Crystal structure of the entire respiratory complex I.’, *Nature*, 494(7438), pp. 443–8.

Bayona-Bafaluy, M. P., Movilla, N., Perez-Martos, A., Fernandez-Silva, P. and Enriquez, J. A. (2008) ‘Functional genetic analysis of the mammalian mitochondrial DNA encoded peptides: a mutagenesis approach.’, *Methods in molecular biology (Clifton, N.J.)*. United States, 457, pp. 379–390.

Baysal, B. E., Rubinstein, W. S. and Taschner, P. E. (2001) ‘Phenotypic dichotomy in mitochondrial complex II genetic disorders’, *Journal of Molecular Medicine*, 79(9), pp. 495–503.

Beinlich, F. R. M., Drees, C., Piehler, J., Busch, K. B., Beinlich, F. R. M., Drees, C., Piehler, J. and Busch, K. B. (2015) ‘Shuttling of PINK1 between mitochondrial microcompartments resolved by triple-color superresolution microscopy Shuttling of PINK1 between mitochondrial microcompart- ments resolved by triple-color superresolution microscopy’, *ACS Chemical Biology*, 10(9), pp. 1970–1976.

Belogrudov, G. I., Tomich, J. M. and Hatefi, Y. (1995) ‘ATP Synthase Complex’, pp. 2053–2060.

Benador, I. Y., Veliova, M., Mahdaviani, K., Petcherski, A., Wikstrom, J. D., Assali, E., Acin-Pérez, R., Shum, M., Oliveira, M. F., Cinti, S., Sztalryd, C., Barshop, W., Wohlschlegel, J., Corkey, B. E., Liesa, M. and Shirihai, O. S. (2018) ‘Mitochondria Bound to Lipid Droplets Have Unique Composition, Bioenergetics, and Dynamics That Support Lipid Droplet Expansion’, *Cell Metabolism (in press)*, pp. 869–885.

Betzig, E., Patterson, G. H., Sougrat, R., Lindwasser, O. W., Olenych, S., Bonifacino, J. S., Davidson, M. W., Lippincott-Schwartz, J. and Hess, H. F. (2006) ‘Imaging Intracellular Fluorescent Proteins at Nanometer Resolution’, *Science*, 313(5793), pp. 1642–1645.

Blom, H. and Brismar, H. (2014) ‘STED microscopy: Increased resolution for medical research?’, *Journal of Internal Medicine*, 276(6), pp. 560–578.

Bradford, M. M. (1976) ‘A rapid and sensitive method for the quantitation of microgram quantities of protein utilizing the principle of protein-dye binding’, *Analytical Biochemistry*, 72(1–2), pp. 248–254.

Bruno, C., Sacco, O., Santorelli, F. M., Assereto, S., Tonoli, E., Bado, M., Rossi, G. A. and Minetti, C. (2003) ‘Mitochondrial myopathy and respiratory failure associated with a new mutation in the mitochondrial transfer ribonucleic acid glutamic acid gene.’, *Journal of child neurology*. United States, 18(4), pp. 300–303.

Budde, S. M., van den Heuvel, L. P., Janssen, A. J., Smeets, R. J., Buskens, C. a,

DeMeirleir, L., Van Coster, R., Baethmann, M., Voit, T., Trijbels, J. M. and Smeitink, J. a (2000) 'Combined enzymatic complex I and III deficiency associated with mutations in the nuclear encoded NDUFS4 gene.', *Biochemical and biophysical research communications*, 275(1), pp. 63–68.

Cascarano, J., Chambers, P. A., Schwartz, E., Poorkaj, P. and Gondo, R. E. (1995) 'Organellar clusters formed by mitochondrial-rough endoplasmic reticulum associations: An ordered arrangement of mitochondria in hepatocytes', *Hepatology*, 22(3), pp. 837–846.

Chance, B., Williams, G., Holmes, W. and Higgins, J. (1955) 'Respiratory Enzymes in Oxidative Phosphorylation', *J Biol Chem*, 217, pp. 409–428.

Chance, B., Williams, G., Holmes, W. and Higgins, J. (1955) 'Respiratory Enzymes in Oxidative Phosphorylation', *J Biol Chem*, 217, pp. 409–428.

Chelbi, S. T., Wilson, M. L., Veillard, A. C., Ingles, S. A., Zhang, J., Mondon, F., GasCOIn-Lachambre, G., Doridot, L., Mignot, T. M., Rebourcet, R., Carbonne, B., Concordet, J. P., Barbaux, S. and Vaiman, D. (2012) 'Genetic and epigenetic mechanisms collaborate to control SERPINA3 expression and its association with placental diseases', *Human Molecular Genetics*, 21(9), pp. 1968–1978.

Chen, R., Runswick, M. J., Carroll, J., Fearnley, I. M. and Walker, J. E. (2007) 'Association of two proteolipids of unknown function with ATP synthase from bovine heart mitochondria', *FEBS letters*, 581(17), pp. 3145–8.

Chinnery, P. F. and Hudson, G. (2013) 'Mitochondrial genetics', *British Medical Bulletin*, 106(1), pp. 135–159.

Cnop, M., Foufelle, F. and Velloso, L. A. (2012) 'Endoplasmic reticulum stress, obesity and diabetes', *Trends in Molecular Medicine*. Elsevier Ltd, 18(1), pp. 59–68.

Cogliati, S., Enriquez, J. A. and Scorrano, L. (2016) 'Mitochondrial Cristae: Where Beauty Meets Functionality', *Trends in Biochemical Sciences*, 41(3), pp. 261–273.

D'Aurelio, M., Gajewski, C. D., Lenaz, G. and Manfredi, G. (2006) 'Respiratory chain supercomplexes set the threshold for respiration defects in human mtDNA mutant cybrids.', *Human molecular genetics*, 15(13), pp. 2157–69.

Daems, W. T. and Wisse, E. (1966) 'Shape and attachment of the cristae mitochondriales in mouse hepatic cell mitochondria.', *Journal of ultrastructure research*. United States, 16(1), pp. 123–140.

Diaz, F. (2010) 'Cytochrome c oxidase deficiency: Patients and animal models', *Biochimica et Biophysica Acta (BBA) - Molecular Basis of Disease*. Elsevier B.V., 1802(1), pp. 100–110.

Diaz, F., Fukui, H., Garcia, S. and Moraes, C. T. (2006) 'Cytochrome c oxidase is required for the assembly/stability of respiratory complex I in mouse fibroblasts', *Molecular and cellular biology*, 26(13), pp. 4872–4881.

Dudkina, N. V, Eubel, H., Keegstra, W., Boekema, E. J. and Braun, H.-P. (2005)

‘Structure of a mitochondrial supercomplex formed by respiratory-chain complexes I and III.’, *Proceedings of the National Academy of Sciences of the United States of America*, 102(9), pp. 3225–3229.

Dudkina, N. V, Kudryashev, M., Stahlberg, H. and Boekema, E. J. (2011) ‘Interaction of complexes I, III, and IV within the bovine respirasome by single particle cryoelectron tomography.’, *Proceedings of the National Academy of Sciences of the United States of America*, 108(37), pp. 15196–200.

Dumoulin, R., Sagnol, I., Ferlin, T., Bozon, D., Stepien, G. and Mousson, B. (1996) ‘A novel gly290asp mitochondrial cytochromebmutation linked to a complex III deficiency in progressive exercise intolerance’, *Molecular and Cellular Probes*, 10(5), pp. 389–391.

Dyba, M. and Hell, S. W. (2002) ‘Focal spots of size lambda/23 open up far-field fluorescence microscopy at 33 nm axial resolution.’, *Physical review letters*. United States, 88(16), p. 163901.

E. Abbe (1873) ‘Beiträgezur Theoriedes des mikroskops und der mikroskopischen Wahrnehmung’, *Construction*, Volume 9(Issue 1), p. pp 413-418.

Embley, T. M. and Martin, W. (2006) ‘Eukaryotic evolution, changes and challenges’, *Nature*, 440(7084), pp. 623–630.

Enríquez, J. A. (2016) ‘Supramolecular Organization of Respiratory Complexes’, *Annual review of physiology*, 78(533–61).

Eubel, H., Heinemeyer, J. and Braun, H. (2004) ‘Identification and Characterization of Respirasomes’, *Plant Physiology*, 134(April), pp. 1450–1459.

Eubel, H., Jansch, L. and Braun, H. (2003) ‘New Insights into the Respiratory Chain of Plant Mitochondria. Supercomplexes and a Unique Composition of Complex II’, *Plant Physiology*, 133, pp. 274–286.

Fernandez-Vizarra, E., Bugiani, M., Goffrini, P., Carrara, F., Farina, L., Procopio, E., Donati, A., Uziel, G., Ferrero, I. and Zeviani, M. (2007) ‘Impaired complex III assembly associated with BCS1L gene mutations in isolated mitochondrial encephalopathy’, *Human Molecular Genetics*, 16(10), pp. 1241–1252.

Fernández-Vizarra, E., Ferrín, G., Pérez-Martos, A., Fernández-Silva, P., Zeviani, M. and Enríquez, J. A. (2010) ‘Isolation of mitochondria for biogenetical studies: An update’, *Mitochondrion*. Mitochondria Research Society, 10(3), pp. 253–262.

Fiedorczuk, K., Letts, J. A., Degliesposti, G., Kaszuba, K., Skehel, M. and Sazanov, L. A. (2016) ‘Atomic structure of the entire mammalian mitochondrial complex I’, *Nature*. Nature Publishing Group, 538(7625), pp. 406–410.

Fletcher, P. A., Scriven, D. R. L., Schulson, M. N. and Moore, E. D. W. (2010) ‘Multi-image colocalization and its statistical significance’, *Biophysical Journal*. Biophysical Society, 99(6), pp. 1996–2005.

Frey, T. G. and Mannella, C. A. (2000) 'Mannella - The Internal Structure of Mitochondria', *Trends Biochem Sci*, 0004(July), pp. 1–6.

Fung, T. S., Torres, J. and Liu, D. X. (2015) 'The emerging roles of viroporins in ER stress response and autophagy induction during virus infection', *Viruses*, 7(6), pp. 2834–2857.

Gan, L. et al., (2012) 'Electron tomography of cells', *Quarterly Reviews of Biophysics*. Cambridge University Press, 45(01), pp. 27–56.

Gething, M. J. and Sambrook, J. (1992) 'Protein folding in the cell.', *Nature*. England, 355(6355), pp. 33–45.

Giorgio, V., von Stockum, S., Antoniel, M., Fabbro, A., Fogolari, F., Forte, M., Glick, G. D., Petronilli, V., Zoratti, M., Szabó, I., Lippe, G. and Bernardi, P. (2013) 'Dimers of mitochondrial ATP synthase form the permeability transition pore.', *Proceedings of the National Academy of Sciences of the United States of America*, 110(15), pp. 5887–92.

Gould, T. J., Burke, D., Bewersdorf, J. and Booth, M. J. (2012) 'Adaptive optics enables 3D STED microscopy in aberrating specimens', *Optics Express*, 20(19), p. 20998.

Gu, J., Wu, M., Guo, R., Yan, K., Lei, J., Gao, N. and Yang, M. (2016) 'The architecture of the mammalian respirasome', *Nature*, 537(7622), pp. 1–16.

Guarás, A., Perales-Clemente, E., Calvo, E., Acín-Pérez, R., Loureiro-Lopez, M., Pujol, C., Martínez-Carrascoso, I., Nuñez, E., García-Marqués, F., Rodríguez-Hernández, M. A., Cortés, A., Diaz, F., Pérez-Martos, A., Moraes, C. T., Fernández-Silva, P., Trifunovic, A., Navas, P., Vazquez, J. and Enríquez, J. A. (2016) 'The CoQH2/CoQ Ratio Serves as a Sensor of Respiratory Chain Efficiency', *Cell Reports*, 15(1), pp. 197–209.

Guo, R., Zong, S., Wu, M. and Yang, M. (2017) 'Architecture of Human Mitochondrial Respiratory Megacomplex I2III2IV2', *Cell*. Elsevier Inc., 170(6), p. 1247–1249.e12.

Hackenbrock, C. R., Chazotte, B. and Gupte, S. S. (1986) 'The random collision model and a critical assessment of diffusion and collision in mitochondrial electron transport', *Journal of Bioenergetics and Biomembranes*, 18(5), pp. 331–368.

Harding, H. P., Zhang, Y. and Ron, D. (1999) 'Protein translation and folding are coupled by an endoplasmic-reticulum-resident kinase.', *Nature*, 397(6716), pp. 271–274.

Hayashi, C., Takibuchi, G., Shimizu, A., Mito, T., Ishikawa, K., Nakada, K. and Hayashi, J. I. (2015) 'A somatic T15091C mutation in the Cytb gene of mouse mitochondrial DNA dominantly induces respiration defects', *Biochemical and Biophysical Research Communications*. Elsevier Ltd, 463(4), pp. 1021–1027.

Heide, H., Bleier, L., Steger, M., Ackermann, J., Dröse, S., Schwamb, B., Zörnig, M., Reichert, A. S., Koch, I., Wittig, I. and Brandt, U. (2012) 'Complexome profiling identifies TMEM126B as a component of the mitochondrial complex i assembly complex', *Cell Metabolism*, 16(4), pp. 538–549.

Hell, S. W. (2003) 'Toward fluorescence nanoscopy', *Nature Biotechnology*, 21(11), pp. 1347–1355.

Hell, S. W. and Wichmann, J. (1994) ‘Breaking the diffraction resolution limit by stimulated emission: stimulated-emission-depletion fluorescence microscopy.’, *Optics letters*. United States, 19(11), pp. 780–782.

Hess, S. T., Girirajan, T. P. K. and Mason, M. D. (2006) ‘Ultra-High Resolution Imaging by Fluorescence Photoactivation Localization Microscopy’, *Biophysical Journal*. Elsevier, 91(11), pp. 4258–4272.

Holt, I. J., Harding, A. E. and Morgan-Hughes, J. A. (1988) ‘Deletions of muscle mitochondrial DNA in patients with mitochondrial myopathies’, *Nature*. Nature Publishing Group, 331(6158), pp. 717–719.

Hotta, J. I., Fron, E., Dedecker, P., Janssen, K. P. F., Li, C., Mullen, K., Harke, B., Buckers, J., Hell, S. W. and Hofkens, J. (2010) ‘Spectroscopic rationale for efficient stimulated-emission depletion microscopy fluorophores’, *Journal of the American Chemical Society*, 132(14), pp. 5021–5023.

Hussain, S. G. and Ramaiah, K. V. (2007) ‘Endoplasmic reticulum: Stress, signalling and apoptosis’.

Iwata, S. (1998) ‘Complete Structure of the 11-Subunit Bovine Mitochondrial Cytochrome bc1 Complex’, *Science*, 281(5373), pp. 64–71.

Jakobs, S. and Wurm, C. A. (2014) ‘Super-resolution microscopy of mitochondria’, *Current Opinion in Chemical Biology*. Elsevier Ltd, 20(1), pp. 9–15.

Jans, D. C., Wurm, C. a, Riedel, D., Wenzel, D., Stagge, F., Deckers, M., Rehling, P. and Jakobs, S. (2013) ‘STED super-resolution microscopy reveals an array of MINOS clusters along human mitochondria.’, *Proceedings of the National Academy of Sciences of the United States of America*, 110(22), pp. 8936–41.

Kadowaki, H. and Nishitoh, H. (2013) ‘Signaling pathways from the endoplasmic reticulum and their roles in disease’, *Genes*, 4(3), pp. 306–333.

Keightley, J. A., Anitori, R., Burton, M. D., Quan, F., Buist, N. R. and Kennaway, N. G. (2000) ‘Mitochondrial encephalomyopathy and complex III deficiency associated with a stop-codon mutation in the cytochrome b gene.’, *American journal of human genetics*. United States, 67(6), pp. 1400–1410.

Kelly, D. P. and Scarpulla, R. C. (2004) ‘Transcriptional regulatory circuits controlling mitochondrial biogenesis and function’, *Genes & Development*, (314), pp. 357–368.

Krause, F., Reifschneider, N. H., Vocke, D., Seelert, H., Rexroth, S. and Dencher, N. A. (2004) ‘“Respirasome”-like supercomplexes in green leaf mitochondria of spinach’, *Journal of Biological Chemistry*, 279(46), pp. 48369–48375.

Kroemer, G. and Reed, J. C. (2000) ‘Mitochondrial control of cell death’, *Nature Medicine*. Nature Publishing Group, 6(5), pp. 513–519.

Kühlbrandt, W. (2015) ‘Structure and function of mitochondrial membrane protein complexes’, *BMC Biology*. BMC Biology, 13(1), p. 89.

Kukat, C., Davies, K. M., Wurm, C. A., Spåhr, H., Bonekamp, N. A., Kühl, I., Joos, F., Loguercio, P., Bae, C., Posse, V., Falkenberg, M. and Jakobs, S. (2015) 'Cross-strand binding of TFAM to a single mtDNA molecule forms the mitochondrial nucleoid', *Proceedings of the National Academy of Sciences*, 112(36), pp. 11288–11293.

Lamantea, E., Carrara, F., Mariotti, C., Morandi, L., Tiranti, V. and Zeviani, M. (2002) 'A novel nonsense mutation (Q352X) in the mitochondrial cytochrome b gene associated with a combined deficiency of complexes I and III', *Neuromuscular Disorders*, 12(1), pp. 49–52.

Lapuente-Brun, E., Moreno-Loshuertos, R., Acín-Pérez, R., Latorre-Pellicer, A., Colás, C., Balsa, E., Perales-Clemente, E., Quirós, P. M., Calvo, E., Rodríguez-Hernández, M. a, Navas, P., Cruz, R., Carracedo, Á., López-Otín, C., Pérez-Martos, A., Fernández-Silva, P., Fernández-Vizarra, E. and Enríquez, J. A. (2013) 'Supercomplex assembly determines electron flux in the mitochondrial electron transport chain.', *Science*, 340(6140), pp. 1567–70.

Legros, F., Chatzoglou, E., Frachon, P., Ogier De Baulny, H., Laforêt, P., Jardel, C., Godinot, C. and Lombès, A. (2001) 'Functional characterization of novel mutations in the human cytochrome b gene.', *European journal of human genetics : EJHG*, 9(7), pp. 510–8.

Letts, J. A., Fiedorczuk, K. and Sazanov, L. A. (2016) 'The architecture of respiratory supercomplexes', *Nature*, 537(7622), pp. 644–648.

Lodish, H., Berk, A., Zipursky, S., Matsudaira, P., Baltimore, D. and Darnell, J. (2003) *Molecular Cell Biology*. 5th editio. Edited by W. H. Freeman. New York: W. H. Freeman.

Luft, R., Ikkos, D., Palmieri, G., Ernster, L. and Afzelius, B. (1962) 'A case of severe hypermetabolism of nonthyroid origin with a defect in the maintenance of mitochondrial respiratory control: a correlated clinical, biochemical, and morphological study.', *The Journal of clinical investigation*. United States, 41, pp. 1776–1804.

MacDonald, J. A., Fowle, W. H. and Woods PhD, D. C. (2017) 'New insights on mitochondrial heterogeneity observed in prepared mitochondrial samples following a method for freeze-fracture and scanning electron microscopy', *Micron*. Elsevier, 101(April), pp. 25–31.

Mannella, C. A. (2006) 'Structure and dynamics of the mitochondrial inner membrane cristae', *Biochimica et Biophysica Acta (BBA) - Molecular Cell Research*, 1763(5–6), pp. 542–548.

Marin-Garcia, J., Hu, Y., Ananthakrishnan, R., Pierpont, M. E., Pierpont, G. L. and Goldenthal, M. J. (1996) 'A point mutation in the cytb gene of cardiac mtDNA associated with complex III deficiency in ischemic cardiomyopathy.', *Biochemistry and molecular biology international*. England, 40(3), pp. 487–495.

Marques, I., Dencher, N. A., Videira, A. and Krause, F. (2007) 'Supramolecular organization of the respiratory chain in Neurospora crassa mitochondria', *Eukaryotic Cell*, 6(12), pp. 2391–2405.

Meyer, B., Wittig, I., Trifilieff, E., Karas, M. and Schägger, H. (2007) 'Identification of two proteins associated with mammalian ATP synthase.', *Molecular & cellular proteomics : MCP*, 6(10), pp. 1690–1699.

Morán, M., Marín-Buera, L., Gil-Borlado, M. C., Rivera, H., Blázquez, A., Seneca, S., Vázquez-López, M., Arenas, J., Martín, M. A. and Ugalde, C. (2010) 'Cellular pathophysiological consequences of BCS1L mutations in mitochondrial complex III enzyme deficiency', *Human Mutation*, 31(8), pp. 930–941.

Moreno-Lastres, D., Fontanesi, F., García-Consuegra, I., Martín, M. A., Arenas, J., Barrientos, A. and Ugalde, C. (2012) 'Mitochondrial complex I plays an essential role in human respirasome assembly', *Cell Metabolism*, 15(3), pp. 324–335.

Moreno-Loshuertos, R. and Enríquez, J. A. (2016) 'Respiratory supercomplexes and the functional segmentation of the CoQ pool', *Free Radical Biology and Medicine*. Elsevier, 100, pp. 05-13.

Mori, K. (2000) 'Tripartite Management Minireview of Unfolded Proteins in the Endoplasmic Reticulum Cell 452 Figure 2. Mechanism for ER Stress–Induced Transcriptional Induction in Mammalian Cells', *Cell*, 101, pp. 451–454.

Müller, C. S., Bildl, W., Haupt, A., Ellenrieder, L., Becker, T., Hunte, C., Fakler, B. and Schulte, U. (2016) 'Cryo-slicing Blue Native-Mass Spectrometry (csBN-MS), a Novel Technology for High Resolution Complexome Profiling', *Molecular & Cellular Proteomics*, 15(2), pp. 669–681.

Muster, B., Kohl, W., Wittig, I., Strecker, V., Joos, F., Haase, W., Bereiter-Hahn, J. and Busch, K. (2010) 'Respiratory chain complexes in dynamic mitochondria display a patchy distribution in life cells', *PLoS ONE*, 5(7).

Nübel, E., Wittig, I., Kerscher, S., Brandt, U. and Schägger, H. (2009) 'Two-dimensional native electrophoretic analysis of respiratory supercomplexes from Yarrowia lipolytica.', *Proteomics*, 9(9), pp. 2408–18.

Nunnari, J. and Suomalainen, A. (2012) 'Mitochondria: In sickness and in health', *Cell*. Elsevier Inc., 148(6), pp. 1145–1159.

Okamoto, K., Perlman, P. S. and Butow, R. A. (2001) 'Targeting of green fluorescent protein to mitochondria.', *Methods in cell biology*. United States, 65, pp. 277–283.

Orlova, E. V. and Saibil, H. R. (2011) 'Structural analysis of macromolecular assemblies by electron microscopy', *Chemical Reviews*, 111(12), pp. 7710–7748.

Osellame, L. D., Blacker, T. S. and Duchen, M. R. (2012) 'Cellular and molecular mechanisms of mitochondrial function', *Best Practice & Research Clinical Endocrinology & Metabolism*. Elsevier Ltd, 26(6), pp. 711–723.

Palade, G. E. (1952) 'The fine structure of mitochondria.', *The Anatomical record*. United States, 114(3), pp. 427–451.

Petros, J. A., Baumann, A. K., Ruiz-Pesini, E., Amin, M. B., Sun, C. Q., Hall, J., Lim, S., Issa, M. M., Flanders, W. D., Hosseini, S. H., Marshall, F. F. and Wallace, D. C. (2005) 'mtDNA mutations increase tumorigenicity in prostate cancer.', *Proceedings of the National Academy of Sciences of the United States of America*. National Academy of Sciences, 102(3), pp. 719–24.

Rainbolt, T. K., Atanassova, N., Genereux, J. C. and R. Luke Wiseman (2013) 'Stress-Regulated Translational Attenuation Adapts Mitochondrial Protein Import Through Tim17A Degradation', 18(6), pp. 908–919.

Rashid, H., Yadav, R. K., Kim, H., Chae, H., Rashid, H., Yadav, R. K., Kim, H. and Chae, H. (2015) 'ER stress : Autophagy induction , inhibition and selection ER stress : Autophagy induction , inhibition and selection', *Autophagy*, 8627(December 2016), pp. 1956–1977.

Rust, M. J., Bates, M. and Zhuang, X. (2006) 'Sub-diffraction-limit imaging by stochastic optical reconstruction microscopy (STORM)', *Nature Methods*, 3(10), pp. 793–796.

Rutter, J., Winge, D. R. and Schiffman, J. D. (2011) 'Succinate Dehydrogenase—Assembly, Regulation and Role in Human Disease', 10(4), pp. 393–401.

Saada, A., Edvardson, S., Shaag, A., Chung, W. K., Segel, R., Miller, C., Jalas, C. and Elpeleg, O. (2012) 'Combined OXPHOS complex i and IV defect, due to mutated complex i assembly factor C20ORF7', *Journal of Inherited Metabolic Disease*, 35(1), pp. 125–131.

Saiki, R., Scharf, S., Faloona, F., Mullis, K., Horn, G., Erlich, H., Arnheim, N. and Nikoskelainen, E. (1985) 'Enzymatic amplification of beta-globin genomic sequences and restriction site analysis for diagnosis of sickle cell anemia', *Science*. American Association for the Advancement of Science, 230(4732), pp. 1350–1354.

Sazanov, L. a. (2015) 'A giant molecular proton pump: structure and mechanism of respiratory complex I', *Nature Reviews Molecular Cell Biology*, 16(6), pp. 375–388.

Schägger, H. (2001) 'Respiratory chain supercomplexes.', *IUBMB Life*, 52(3–5), pp. 119–128.

Schägger, H. and Pfeiffer, K. (2000) 'Supercomplexes in the respiratory chains of yeast and mammalian mitochondria.', *The EMBO journal*, 19(8), pp. 1777–1783.

Schindelin, J., Arganda-Carreras, I., Frise, E., Kaynig, V., Longair, M., Pietzsch, T., Preibisch, S., Rueden, C., Saalfeld, S., Schmid, B., Tinevez, J.-Y., White, D. J., Hartenstein, V., Eliceiri, K., Tomancak, P. and Cardona, A. (2012) 'Fiji: an open-source platform for biological-image analysis', *Nature Methods*, 9(7), pp. 676–682.

Schindelin, J., Rueden, C., Miura, K., Hiner, M. and Tinevez, J.-Y. (2016) 'CorrectBleach: upgrade with Exponential fitting method'.

Schon, E. A. and Dencher, N. A. (2009) 'Heavy Breathing: Energy Conversion by Mitochondrial Respiratory Supercomplexes', *Cell Metabolism*. Elsevier Inc., 9(1), pp. 1–3.

Schuelke, M., Krude, H., Finckh, B., Mayatepek, E., Janssen, A., Schmelz, M., Trefz, F., Trijbels, F. and Smeitink, J. (2002) 'Septo-optic dysplasia associated with a new mitochondrial cytochrome b mutation.', *Annals of neurology*. United States, 51(3), pp. 388–392.

Sen, D., Balakrishnan, B. and Jayandharan, G. R. (2014) 'Cellular unfolded protein response against viruses used in gene therapy ', *Frontiers in Microbiology* , p. 250.

Shim, S.-H., Xia, C., Zhong, G., Babcock, H. P., Vaughan, J. C., Huang, B., Wang, X., Xu, C., Bi, G.-Q. and Zhuang, X. (2012) 'Super-resolution fluorescence imaging of organelles in live cells with photoswitchable membrane probes', *Proceedings of the National Academy of Sciences*, 109(35), pp. 13978–13983.

Sjöstrand, F. S. (1956) 'The Ultrastructure of Cells as Revealed by the Electron Microscope', in Bourne, G. H. and Danielli, J. F. B. T.-I. R. of C. (eds). Academic Press, pp. 455–533.

Sousa, J. S., Mills, D. J., Vonck, J. and Kühlbrandt, W. (2016) 'Functional asymmetry and electron flow in the bovine respirasome', *eLife*, 5, pp. 1–17.

Stock, D. (1999) 'Molecular Architecture of the Rotary Motor in ATP Synthase', *Science*, 286(5445), pp. 1700–1705.

Sun, F., Huo, X., Zhai, Y., Wang, A., Xu, J., Su, D., Bartlam, M. and Rao, Z. (2005) 'Crystal structure of mitochondrial respiratory membrane protein Complex II', *Cell*, 121(7), pp. 1043–1057.

Suomalainen, A. and Battersby, B. J. (2017) 'Mitochondrial diseases: the contribution of organelle stress responses to pathology', *Nature Reviews Molecular Cell Biology*. Nature Publishing Group.

Tello, D., Balsa, E., Acosta-Iborra, B., Fuertes-Yebra, E., Elorza, A., Ordóñez, Á., Corral-Escariz, M., Soro, I., López-Bernardo, E., Perales-Clemente, E., Martínez-Ruiz, A., Enríquez, J. A., Aragonés, J., Cadenas, S. and Landázuri, M. O. (2011) 'Induction of the mitochondrial NDUFA4L2 protein by HIF-1α decreases oxygen consumption by inhibiting complex i activity', *Cell Metabolism*, 14(6), pp. 768–779.

Timón-Gómez, A., Nývltová, E., Abriata, L. A., Vila, A. J., Hosler, J. and Barrientos, A. (2017) 'Mitochondrial cytochrome c oxidase biogenesis: Recent developments', *Seminars in Cell & Developmental Biology*.

Twig, G., Elorza, A., Molina, A. J. A., Mohamed, H., Wikstrom, J. D., Walzer, G., Stiles, L., Haigh, S. E., Katz, S., Las, G., Alroy, J., Wu, M., Py, B. F., Yuan, J., Deeney, J. T., Corkey, B. E. and Shirihai, O. S. (2008) 'Fission and selective fusion govern mitochondrial segregation and elimination by autophagy', *EMBO Journal*, 27(2), pp. 433–446.

Ugalde, C., Janssen, R. J. R. J., van den Heuvel, L. P., Smeitink, J. A. M. and Nijtmans, L. G. J. (2004) 'Differences in assembly or stability of complex I and other mitochondrial OXPHOS complexes in inherited complex I deficiency', *Human Molecular Genetics*, 13(6), pp. 659–667.

Valnot, I., Kassis, J., Chretien, D., de Lonlay, P., Parfait, B., Munnich, A., Kachaner, J., Rustin, P. and Rotig, A. (1999) 'A mitochondrial cytochrome b mutation but no mutations of nuclearly encoded subunits in ubiquinol cytochrome c reductase (complex III) deficiency.', *Human genetics*. Germany, 104(6), pp. 460–466.

Vonck, J. and Schäfer, E. (2009) 'Supramolecular organization of protein complexes in the mitochondrial inner membrane.', *Biochimica et biophysica acta*. Elsevier B.V., 1793(1), pp. 117–124.

Walker, J. E. (2013) 'The ATP synthase: the understood, the uncertain and the unknown.', *Biochemical Society transactions*. Portland Press Limited, 41(1), pp. 1–16.

Walker, J. E. and Collinson, I. R. (1994) 'The role of the stalk in the coupling mechanism of F1F0-ATPases', *FEBS Letters*, 346(1), pp. 39–43.

Wallace, D. C. (2005) 'A mitochondrial paradigm of metabolic and degenerative diseases, aging, and cancer: a dawn for evolutionary medicine.', *Annual review of genetics*, 39, pp. 359–407.

Wallace, D. C., Fan, W. and Procaccio, V. (2010) 'Mitochondrial Energetics and Therapeutics', *Annual Review of Pathology: Mechanisms of Disease*, 5(1), pp. 297–348.

Westphal, V. and Hell, S. W. (2005) 'Nanoscale resolution in the focal plane of an optical microscope.', *Physical review letters*. United States, 94(14), p. 143903.

Wibrand, F., Ravn, K., Schwartz, M., Rosenberg, T., Horn, N. and Vissing, J. (2001) 'Multisystem disorder associated with a missense mutation in the mitochondrial cytochrome b gene.', *Annals of neurology*. United States, 50(4), pp. 540–543.

Wilkens, V., Kohl, W. and Busch, K. (2012) 'Restricted diffusion of OXPHOS complexes in dynamic mitochondria delays their exchange between cristae and engenders a transitory mosaic distribution', *Journal of Cell Science*.

Wu, M., Gu, J., Guo, R., Huang, Y. and Yang, M. (2016) 'Structure of Mammalian Respiratory Supercomplex I1III2IV1', *Cell*. Elsevier, 167(6), p. 1598–1609.e10.

Xu, C., Bailly-Maitre, B. and Reed, J. C. (2005) 'Endoplasmic reticulum stress: cell life and death decisions.', *The Journal of clinical investigation*. United States, 115(10), pp. 2656–2664.

Yang, G. D., Yang, X. M., Lu, H., Ren, Y., Ma, M. Z., Zhu, L. Y., Wang, J. H., Song, W. W., Zhang, W. M., Zhang, R. and Zhang, Z. G. (2014) 'SERPINA3 promotes endometrial cancer cells growth by regulating G2/M cell cycle checkpoint and apoptosis', *International Journal of Clinical and Experimental Pathology*, 7(4), pp. 1348–1358.

Yang, W.-C., Li, H., Wang, F., Zhu, X.-L. and Yang, G.-F. (2012) 'Rieske Iron–Sulfur Protein of the Cytochrome bc1 Complex: A Potential Target for Fungicide Discovery', *ChemBioChem*. WILEY-VCH Verlag, 13(11), pp. 1542–1551.

Zhao, C., Yin, S., Dong, Y., Guo, X., Fan, L., Ye, M. and Hu, H. (2013) 'Autophagy-dependent EIF2AK3 activation compromises ursolic acid-induced apoptosis through upregulation of MCL1 in MCF-7 human breast cancer cells', *Autophagy*, 9(2), pp. 196–207.

Zhou, Z. H. (2011) 'Chapter 1 - Atomic resolution cryo electron microscopy of macromolecular complexes', in Ludtke, S. J. and Venkataram Prasad, B. V. B. T.-A. in P. C. and S. B. (eds) *Recent Advances in Electron Cryomicroscopy, Part B*. Academic Press, pp. 1–35.

Zick, M., Rabl, R. and Reichert, A. S. (2009) 'Cristae formation-linking ultrastructure and function of mitochondria', *Biochimica et Biophysica Acta - Molecular Cell Research*. Elsevier B.V., 1793(1), pp. 5–19.